Solidification Of Eutectic And Off-eutectic Aluminum-zinc Alloys.

Order Number 9513108

Solidification of eutectic and off-eutectic Al-Zn alloys

Bluni, Scott Thomas, Ph.D.

Lehigh University, 1994

U·M·I
300 N. Zeeb Rd.
Ann Arbor, MI 48106

Solidification of Eutectic and Off-Eutectic Al-Zn Alloys

by

Scott Thomas Bluni

A Dissertation Presented to
the Graduate Committee of Lehigh University
in Candidacy for the Degree of

Doctor of Philosophy

in

Materials Science & Engineering

Lehigh University

1994

Certificate of Approval

Approved and recommended for acceptance as a dissertation in partial fulfillment of the requirements for the degree of Doctor of Philosophy.

8/26/94
Date

Dissertation Director
A.R. Marder

8/26/94
Accepted Date

Special Committee directing the work of Mr. Scott T. Bluni:

A.R. Marder (Chairman)

J.I. Goldstein

M.R. Notis

K. Barmak

F.E. Goodwin

ACKNOWLEDGEMENTS

There are many mentors, colleages, and friends who contributed to the successful completion of this dissertation. Dr. Arnie Marder was a constant source of ideas and insight, and I am indebted to him for his direction as project advisor. Drs. Goldstein, Notis, and Barmak were equally as helpful in making thoughtful contributions into experimental techniques, analysis of results, and the preparation of this manuscript. My final committee member, Dr. Frank Goodwin, kept me in check with "real-world" considerations so that this research would provide useful information for corporate sponsors. The assistance of Arlan Benscoter, both in the lab and the gym, was of vital importance to this work. Others who provided technical assistance include Jim Kerner, Kathy Repa, Dave Ackland, and Andrea Pressler; each of whom are truly top-notch and whose contributions were essential. Brief but helpful communications with Professor John Perepezko of The University of Wisconsin-Madison are also gratefully acknowledged. There are a number of graduate students I would like to thank for their inciteful discussions and friendship during my studies at Lehigh: Brian Smith, Saikumar Vivekenand, Cathy Jordan, Bruce Lindsley, John DuPont, Boris Levin, Kevin Stein, Rick Baron, Sean Hayes, and Don Susan. This research would not have been possible without the financial support of the International Lead Zinc Research Organization (ILZRO) and its members, and their funding is gratefully acknowledged. Special thanks is given to Mr. Alan Jenkins of British Steel, Dr. Jean Wégria of Union Miniere, Mr. Michel Dubois of Cockerill Sambre, and Mr. Josef Faderl of Voest-

Alpine for their hospitality while visiting sponsoring companies in Europe and offering additional direction to this research. Finally, I would like to thank my wife, Maria, for her patience, emotional support, and love during our years in Bethlehem.

TABLE OF CONTENTS

LIST OF TABLES

LIST OF FIGURES

LIST OF SYMBOLS

Symbol	Definition
A	Surface area
C_E	Eutectic solute concentration
$C_{Z=0}$	Solute concentration at the solid/liquid interface
C_∞	Alloy solute concentration
D	Diffusion coefficient
G	Temperature gradient in the melt
G_c	Solute gradient in the melt
ΔG	Change in Gibbs free energy
ΔG_v	Difference in Gibbs free energy between solid and liquid phases
I	Nucleation rate
k	Boltzmann's constant
K_c	Solute undercooling constant
K_r	Curvature undercooling constant

LIST OF SYMBOLS (cont.)

Symbol	Definition
K(x)	Local interface curvature
m	Liquidus slope
q	Activation energy
r	Radius of a eutectic rod
S(θ)	Shape factor
S	½-width of a eutectic lamellae
t	Time
T	Temperature
ΔT	Total interface undercooling during solidification
ΔT_c	Solute undercooling
ΔT_r	Curvature undercooling
ΔT_k	Kinetic undercooling
V,v	Growth rate

LIST OF SYMBOLS (cont.)

Symbol	Definition
V_s	Volume of solid phase
x	Direction perpendicular to the solidification direction
z	Direction of solidification
α	Jackson's alpha factor, numerically equal to $\Delta S_f/R$
Γ	Gibbs-Thompson coefficient
γ	Interfacial energy
θ	Wetting angle
λ	Eutectic interphase spacing

To Scotty and Mark

ABSTRACT

The use of zinc-based hot-dip coatings for corrosion resistance on steel components is widespread throughout the world. Of all the types of zinc-based hot-dip coatings currently produced on a commercial basis, Galfan® (Zn-5wt% Al) is considered to be the most formable due to the limited formation of an intermetallic compound layer at the substrate/coating interface and the inherent ductile nature of its eutectic structure. Although there are numerous uses for Galfan and the demand for this coating continues to increase, it may not be suitable for some applications which have stringent surface requirements because the coating often contains small surface defects. The problematic surface condition of Galfan coatings has led to interest in the present research program. As an overall objective, this study was designed to address the solidification characteristics of eutectic and off-eutectic Al-Zn alloys. In so doing, the relationships between coating processing conditions and microstructure will be more fully understood, thereby providing a fundamental basis for further coating research and development. The solidification of eutectic and off-eutectic alloys is therefore investigated in terms of nucleation and growth characteristics.

Through the use of differential scanning calorimetry techniques, non-reciprocal nucleation characteristics were found for the Al-Zn system. For alloys with zinc concentrations <95wt% where aluminum is the proeutectic phase, an average undercooling of 0.25°C below the eutectic temperature is required for zinc nucleation and subsequent eutectic formation at a cooling rate of 1 K/min. In comparison, an average undercooling of 4.0°C is necessary for aluminum nucleation on proeutectic zinc in alloys containing ≥ 95wt% zinc at the same cooling rate. Aluminum is therefore said to be a better nucleant of zinc than vice-versa. This non-reciprocal nucleation results in the formation of zinc halos around proeutectic β-Al dendrites and a difference in eutectic structure when comparing hypo- and hypereutectic alloys. For example, the relatively large undercooling required for eutectic nucleation in Zn-rich alloys results in a significant decrease in the interlamellar spacing and a difference in the volume fraction of phases in the eutectic structure when compared to Al-rich alloys. Furthermore, the difference in the volume fraction of phases in the eutectic structure results in a difference in eutectic morphology: the eutectic structure for Zn-rich alloys is strictly lamellar, whereas the eutectic structure for Al-rich alloys consists of rods or rods and lamellae. The changes in interlamellar spacing, volume fraction of phases, and morphology of the eutectic structure brought about by the experimentally determined non-reciprocal nucleation characteristics are in good agreement with theory.

Eutectic and off-eutectic Al-Zn alloys were directionally solidified to determine the role of

solidification parameters on resultant microstructure. In agreement with theory, the interlamellar spacing for unidirectionally solidified Al-Zn alloys was found to be proportional to $V^{-1/2}$. Unlike alloys having a cast structure, the measured λ values for directionally solidified alloys were found to be independent of alloy composition. Also independent of alloy composition was eutectic morphology, which was found to be typically lamellar for hypo- and hypereutectic alloys grown at rates from about 15-105μm/second. Rod eutectic structures were found in these samples only when (1) the eutectic nucleated on a primary dendrite ahead of the solid/liquid interface during growth, and/or (2) the eutectic solidification front encountered a preexisting primary dendrite, causing a breakdown in the planar solid/liquid interface.

The eutectic coupled zone of growth for the Al-Zn eutectic was found to be skewed to the Al-rich side of the eutectic. It was found that the constitutional supercooling criterion did not accurately predict the eutectic-dendritic transition for this system. Instead, it is hypothesized that the competitive growth criterion controls the formation of the stable microstructure. It is therefore suggested that the eutectic structure outgrows β-Al dendrite formation at sufficient undercoolings below the eutectic temperature when in the presence of low temperature gradients in the melt. One possible explanation for this retarded β-Al growth is a significant kinetic undercooling associated with β-Al interfacial motion. However, thermodynamic data for β-Al obtained via differential scanning calorimetry yields an entropy of fusion of 10.9 J/mol•K and therefore an α-factor of 1.31, which is in agreement with published data for pure aluminum. According to accepted theory, these data would indicate β-Al to grow with a negligible kinetic undercooling.

Banding was found for directionally solidified alloys when grown at rates $\leq 50\mu$m/second. A close examination of the bands indicates these regions to be precipitation zones for either of the two eutectic phases. Banding is thought to occur when, during eutectic growth, one of the eutectic phases accumulates at the solid/liquid interface to a concentration which cannot be absorbed by the growing eutectic or sustained as a boundary layer by the advancing interface. This "solute adjustment" can manifest itself as a change in the eutectic interlamellar spacing, a change in the volume fraction of the eutectic phases, and/or the phase precipitation ahead of the solid/liquid interface.

In comparing the solidification structures produced with DSC ("cast" structure) and directional solidification techniques, the undercooling associated with the solidification process was found to be the controlling factor for microstructural development. Regardless of the solidification technique, eutectic microstructural characteristics such as interlamellar spacing, the volume fraction of phases, and the eutectic morphology were found to be equivalent when produced at similar undercoolings.

INTRODUCTION

Aluminum-zinc alloys have long been used for a number of engineering applications. As early as the turn of this century, these alloys were recognized to be of significant industrial importance as casting alloys given their low density, high fluidity, and low surface tension. In more recent times, perhaps the most significant use these alloys has been the application of Zn-rich alloys as corrosion-resistant coatings, which are now considered commonplace for a number of steel components. The requirements for zinc coatings have become so great that by 1991, 1.8 million tons of zinc ore was used for galvanizing steel, representing almost 50% of total worldwide use of zinc. Presently in North America alone, there is approximately 20 million tons of coated-sheet capacity. The rapidly increasing demand for these coatings has resulted in a situation where the steel industry has been quick to respond to consumer demands and, consequently, a number of zinc coating products have been developed without a thorough understanding of these coatings. For example, the relationships between processing parameters, microstructural characteristics, and coating properties may not be fully understood. The result is a product which provides some or all of the required characteristics for which it is intended, but it may not be optimal in terms of cost effectiveness and performance. Scores of research projects are therefore currently underway to investigate fundamental questions regarding hot-dip zinc coatings.

Of all the types of Zn-based hot-dip coatings currently produced on a

commercial basis, Galfan® (Zn-5wt% Al) is considered to be the most formable due to the limited formation of an intermetallic compound layer at the substrate/coating interface and the inherent ductile nature of its eutectic structure. Production of this coating has grown from about 10,000 tons in 1983 to almost 600,000 tons in 1993. Although there are numerous uses for Galfan and the demand for this coating continues to increase, it may not be suitable for some applications which have stringent surface requirements because the coating often contains small surface defects. The factors which contribute to the smoothness of the coating have been unclear, but the problem has been associated with eutectic grain boundaries.

The problematic surface condition of Galfan coatings has led to interest in the present research program. As an overall objective, this study was designed to address the solidification characteristics of eutectic and off-eutectic Al-Zn alloys. In so doing, the relationships between coating processing conditions and microstructure will be more fully understood, thereby providing a fundamental basis for further coating research and development. The solidification of eutectic and off-eutectic alloys is therefore investigated in terms of nucleation and growth characteristics. The effects of composition and cooling rate on the nucleation of proeutectic and eutectic phases, and the subsequent effects on eutectic microstructural development, are examined with the use of differential scanning calorimetry techniques. Likewise, the effects of composition and growth rate on the microstructures of these phases are studied through unidirectional solidification experiments. The microstructures produced by solidification experiments are not intended to simulate those of commercial coating

product, but it is anticipated that the results obtained from this research may be applied to the engineering of Galfan hot-dip coatings.

BACKGROUND

In the following review of the literature and theory which are pertinent to this study, solidification in terms of nucleation and growth, the Al-Zn system and eutectic, and Galfan coatings are discussed, respectively.

Nucleation Theory

The solidification process can be separated into nucleation and growth events. As a liquid cools, a temperature (the solidification point) is reached at which the free energy of the solid phase is equal to that of the liquid. Any further cooling results in a continual decrease in the free energy of the solid phase, and consequently, in a driving force for solidification. A solid phase is said to have nucleated from the melt when a critical number of atoms have bonded in a crystalline array such that a stable embryo has formed and can continue to grow.

Homogeneous Nucleation

In homogeneous nucleation, the solid embryo forms within the melt in the absence of any nucleation catalysts. As explained above, the formation of the solid phase will result in a negative contribution to the system free energy. However, the creation of a solid/liquid interface upon solidification has a positive influence on this energy, resulting in the following expression to describe the change in free energy resulting from the nucleation event:

$$\Delta G = -V_s \Delta G_v + A_{sl} \gamma_{sl} \quad (1)$$

where V_s is the volume of the newly formed solid, ΔG_v is the difference in free energy between the liquid and solid phases, A_{sl} is the area of the solid/liquid interface, and γ_{sl} is the solid/liquid interfacial energy. The second term in equation 1 is often large enough to cause a considerable undercooling (driving force) before nucleation occurs (Turnbull and Cech, 1950) (Thompson and Spaepen, 1983) (Perepezko, 1984). Once initial nucleation has occurred, subsequent nucleation is rapid according to the equation (Turnbull and Fisher, 1949) (Turnbull 1, 1950):

$$I_{hom} = A \exp\left[\frac{-K\gamma^3}{(\Delta G_v)^2 kT}\right] \quad (2)$$

nuclei/mol•sec•cm^3. In this equation, A is a system constant and K is a factor determined by the shape of the nucleus. Although homogeneous nucleation is thought to occur for small droplets dispersed in solution (Thompson and Spaepen, 1983) (Perepezko, 1984) (Chu et al., 1984), it is not achieved for most liquids as there is inevitably some nucleation catalyst or site available in the system (Turnbull 2, 1950) (Holloman and Turnbull, 1951) (Sundquist and Mondolfo, 1961).

Heterogeneous Nucleation

In heterogeneous nucleation, the energy barrier for the start of nucleation is decreased due to the presence of any substrates or impurities in the system which provide initiation sites. For a spherical embryo which solidifies as a "cap" on an already existing solid surface (Figure 1), the free energy required for nucleation is

given as (Turnbull 2, 1950):

$$\Delta G = -V_s \Delta G_v + A_{sl}\gamma_{sl} + A_{sm}\gamma_{sm} - A_{sm}\gamma_{lm} \tag{3}$$

or

$$\Delta G = [-V_s \Delta G_v + A_{sl}\gamma_{sl}][\frac{1}{4}(2+\cos\theta)(1-\cos\theta)^2]. \tag{4}$$

In equation 3, "sm" and "lm" refer to the solid/mold and liquid/mold interfaces, respectively. The second term in equation 4 is commonly written as $S(\theta)$ and denoted as the "shape factor", which has a numerical value ≤ 1 as shown in Figure 2. The free energy required for heterogeneous nucleation is therefore always less than that for homogeneous nucleation by a factor of $S(\theta)$. Likewise, the nucleation rate for heterogeneous nucleation differs by that for homogeneous nucleation (equation 2) due to the influence of the shape factor as follows (Turnbull 1, 1950):

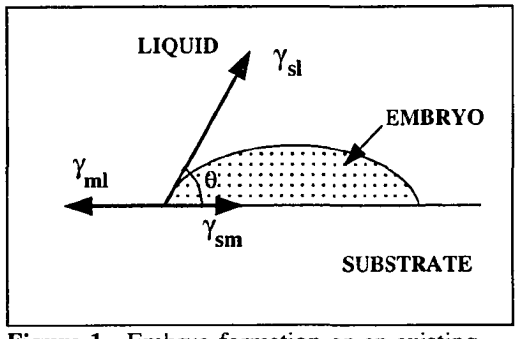

Figure 1. Embryo formation on an existing substrate and associated interfacial energies.

$$I_{het} = A' \exp[\frac{-K\gamma^3[S(\theta)]}{(\Delta G_v)^2 kT}], \tag{5}$$

which can also be written as shown in equation 6 (Turnbull 2, 1950). Here, q is the

$$I = K \exp[\frac{-(\Delta G + q)}{kT}] \tag{6}$$

activation energy necessary for atomic diffusion across the solid/liquid interface and ΔG is given by equations 1 and 4 for homogeneous and heterogeneous nucleation, respectively. Since $\Delta G_{het} << \Delta G_{hom}$, the steady state nucleation rate for heterogeneous nucleation will be much greater at a given temperature than the rate of homogeneous nucleation.

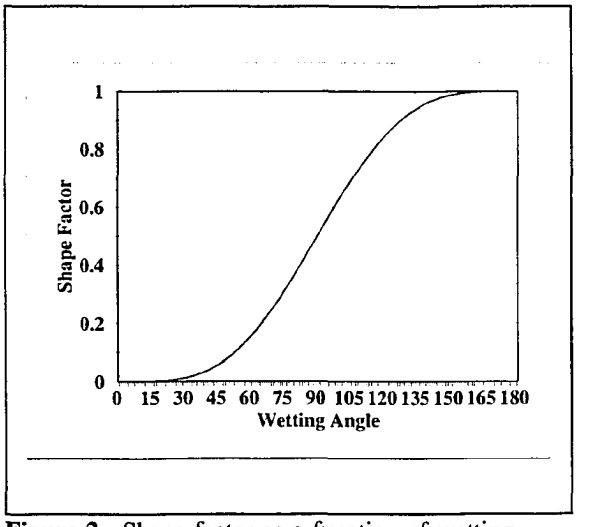

Figure 2. Shape factor as a function of wetting angle.

Eutectic Nucleation

For eutectic alloys, two nucleation events must occur before steady-state growth can ensue. The first is the nucleation of one primary phase, which occurs at some undercooling below the liquidus or eutectic temperature depending on alloy composition. This phase can act to either promote or hinder the nucleation of the other eutectic phase, depending on its "nucleating power". The ability of one solid to heterogeneously nucleate another solid has been the subject of a number of investigations, particularly in eutectic systems. Most studies have indicated that eutectic alloys exhibit "non-reciprocal" nucleating characteristics, meaning that one primary phase will acts as an effective hetereogeneous nucleation site for the other phase, but not vice-versa (Hollomon and Turnbull, 1951) (Sundquist and Mondolfo, 1961) (Powell and Colligan, 1971) (Lemaignan et al., 1980) (Lemaignan, 1981). For example, Sundquist and Mondolfo

found that for the Pb-Sn system, primary Sn will nucleate Pb at undercoolings between 0 and 0.5°C, while primary Pb has no apparent nucleating effect on Sn resulting in an undercooling $\Delta T \geq 55°C$ for Sn nucleation. For some eutectic alloys, a primary phase may be so poor a nucleant that the surrounding melt becomes severely undercooled and solute enriched, resulting in dendritic growth of the undercooled phase prior to eutectic growth (Lemaignan, 1980).

The basis for the differences in nucleating abilities for each primary phase is not clear, but it has previously been related to the melting point of the primary phase and interfacial energy arguments (Sundquist and Mondolfo, 1961) (Southin and Chadwick, 1978). In consideration of Figure 1, it is seen that the solid/liquid interfacial energy of a nucleation catalyst (σ_{ml}) can be considered to be part of the driving force for solidification, while the solid/liquid interfacial energy of the nucleated solid (σ_{sl}) can be considered to be a barrier for nucleation. In other words, an increase in σ_{ml} would tend to decrease the wetting angle (θ) of the nucleated embryo, while an increase in σ_{sl} would tend to increase θ. It follows that metals which have high solid/liquid interfacial energies are difficult to nucleate and will tend to be good nucleating agents, and metals with low solid/liquid interfacial energies will be easy to nucleate and will act as poor nucleating agents. Furthermore, since elements having high melting temperatures typically have higher σ_{sl}'s than elements with lower melting temperatures and equal crystal structures, those elements with higher melting points should be better nucleants than those with lower melting temperatures.

Crystal structure is an important factor in heterogeneous nucleation. Due to lattice mismatch considerations, an interface between two metals of the same crystal structure will usually, but not necessarily, have a lower interfacial energy than that between materials of different crystal structures. Although this has been found to generally hold true (Southin and Chadwick, 1978), a clear understanding of the influence of crystal structure on heterogeneous nucleation has not yet been determined.

Eutectic Growth

In the sections to follow, eutectic growth is discussed in terms of the lamellar-rod transition, interlamellar spacing and interface undercooling, diffusion ahead of the solid/liquid interface, and lamellar curvature.

The Lamellar-Rod Transition

Regular eutectics can grow with either a lamellar or rod morphology, or with both. The transition between lamellar and rod growth has been associated with the volume fraction of the phases involved, the presence of impurities, changes in growth direction, and the curvature of the solid/liquid interface during solidification. As will be shown, many of these factors cannot be considered independantly.

Tiller (1958) noted from a number of early experiments that rods are typical of some eutectics solidified at all growth rates, while for others, lamellae break down into

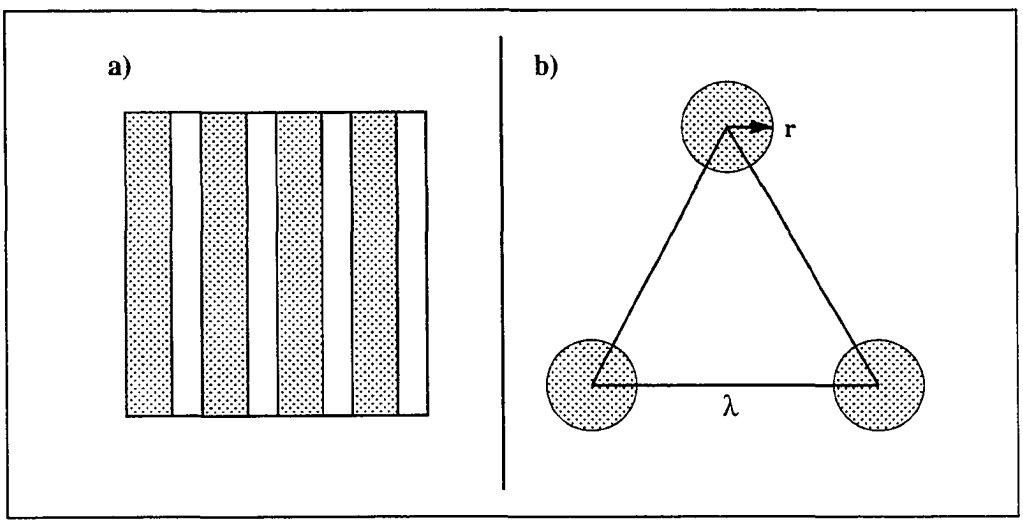

Figure 3. Cross-sections of a) rod and b) lamellar eutectic morphologies.

rods at certain velocities. It is also qualitatively argued that a rod morphology should be favored when the volume fraction of one of the eutectic phases is large. Tiller speculated that there may be some relationhip between growth rate and the volume fraction of phases, thus accounting for the change in some eutectic morphologies with growth rate. Theoretically, however, this is not possible, and there are other explanations for his observations as will be discussed. As noted by Cooksey et al. (1964), the length of the α/β surface per unit cross section in a lamellar morphology is independent of the relative thicknesses of the lamellae and equals $2/\lambda$. For rod growth, however, the α/β surface area is dependent on the relative volume fractions of the two phases. Based on Figure 3, the number of cross-sectional "triangles" resulting from rod formation is $4/\sqrt{3}\lambda^2$, with each triangle containing an α/β interfacial length of πr. The α/β interfacial length is therefore $4\pi r/\sqrt{3}\lambda^2$, and substituting for r, it is

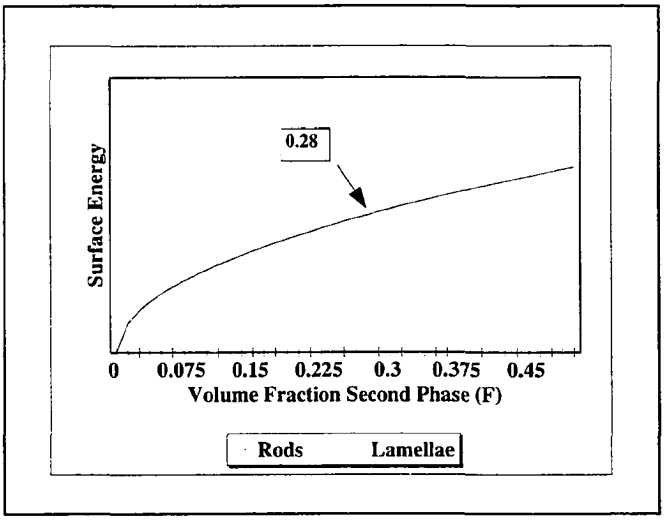

Figure 4. Surface energy produced by rod and lamellar eutectic growth, as a function of volume percent second phase.

calculated to be $3.816F^{0.5}/\lambda$, where F is the volume fraction of the α phase. Based on this analysis, the surface energy associated with rod and lamellar growth is represented in Figure 4, which implies that rod formation is expected at low F values (<0.28), whereas for higher values of F, a lamellar morphology is predicted. It has been shown through similar interfacial energy considerations (Hunt and Chilton, 1963) (Jackson and Hunt, 1966) that a critical volume fraction of 0.3 is expected during isotropic growth. It is also noted (Jackson and Hunt, 1966), however, that for systems which grow anisotropically, it is possible to grow lamellae even at low phase volume fractions.

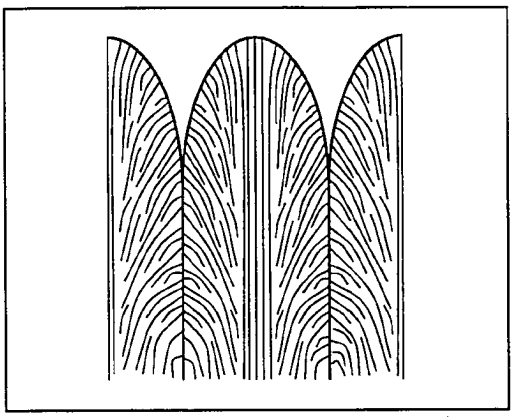

Figure 5. Rod formation due to a curved solid/liquid interface during cellular growth.

In addition to volume fraction considerations, the influence of the solid/liquid interface shape on the lamellar-rod transition has been acknowledged. An experimental analysis (Hunt and Chilton, 1963) has shown that rods will result in an otherwise "lamellar" eutectic when the interface becomes curved or disrupted for any reason, thus solidifying in a direction other than the preferred lamellar growth direction. By this mechanism, it is argued (Hunt and Chilton, 1963) (Hunt, 1966) that impurities indirectly contribute to rod formation. The presence of impurites results in the breakdown of planar front growth, thus resulting in a curved solid/liquid interface. It is this curved interface that

induces rod formation, since the phases will grow normal to the interface as shown in Figure 5. The breakdown will also occur if the eutectic grows into a mechanical obstacle or dendrite. This may explain Tiller's observation that some eutectics will break down into rods at a certain growth rate, since a high velocity implies a high undercooling during solidification, which may result in the formation of eutectic cells (the reader is directed to the section on Coupled Zone Theory).

Eutectic Growth: Interlamellar Spacing and Interface Undercooling

There has been a considerable amount of both theoretical and experimental work on the growth of eutectics. Oddly enough, the paper which provided a fundamental basis for eutectic theory was written to describe the solid-state transformations from austenite in the Fe-Fe_3C system, with particular attention to the eutectoid decomposition to pearlite (Zener, 1946). Using theromodynamic rationale, Zener found that pearlite will grow with an interlamellar spacing which is inversely proportional to the amount of undercooling below the eutectoid transformation temperature. Combining this analysis with the effects of undercooling on diffusion and growth rate, it is deduced that for pearlite growth,

$$\lambda^2 V = constant. \tag{7}$$

Tiller (1958) applied Zener's analysis to eutectics, verifying Equation 7 under the assumption that growth occurs at a minimum undercooling at a given velocity.

The relationship between growth rate and interlamellar spacing can be deduced from undercooling considerations. During solidification, the solid/liquid interface is

assumed to be isothermal along its length and at some temperature below the eutectic temperature, ΔT (Tiller, 1958) (Hunt and Chilton, 1963) (Chadwick, 1963) (Jackson and Hunt, 1966). The factors which contribute to ΔT become clear when eutectic growth can be considered to be the result of two competing effects, namely:

1. Diffusion in the melt, where growing phases are sources or sinks with respect to the diffusing elements; and
2. Interface energy, which would prefer complete separation (no curvature) of the two solid phases in order to minimize the free energy of the system.

These competing effects result in two separate sources for the undercooling of a solid interface below the eutectic temperature during growth: i) ΔT_c, the the solute undercooling, which arises from the local concentrations at the solid/liquid interface and subsequent diffusional limitations; and ii) ΔT_r, the curvature undercooling, which arises from the increase energy associated with an increased curvature of the solid/liquid interface as the interlamellar spacing decreases. One additional contribution is ΔT_k, the kinetic undercooling, which is due to the chemical potential difference which provides the driving force for solidification. Since ΔT_k is negligible for growth in systems where the entropy of fusion is low, such as in metallic systems (Jackson and Hunt, 1966), the total undercooling during eutectic growth can be expressed as follows:

$$\Delta T = \Delta T_c + \Delta T_r \tag{8}$$

where C_E is the eutectic solute concentration, $C_{z=0}$ is the solute concentration at the

$$=[m(C_E - C_{z=0})] + [\Gamma\ K(x)]\ ) \qquad (9$$

$$= K_c \lambda V + \frac{K_r}{\lambda}, \qquad (10)$$

interface, m is the local liquidus slope, Γ is the Gibbs-Thompson coefficient, K(x) is the local interface curvature, and K_c and K_r are solute and curvature constants respectively. The effects of each undercooling contribution for a given velocity are shown graphically in Figures 6 and 7 as functions of interlamellar spacing and of position along the solid/liquid interface, respectively. Assuming that growth occurs at the extrenum condition, or at the minimum undercooling for a given velocity,

$$\frac{d(\Delta T)}{d\lambda} = 0 = K_c V - \frac{K_r}{\lambda^2}, \qquad (11)$$

such that

$$K_c V = \frac{K_r}{\lambda^2} \qquad (12)$$

and therefore,

$$\lambda^2 V = \frac{K_r}{K_c}. \qquad (13)$$

Several experimental investigations (Chadwick, 1963) (Hunt and Chilton, 1963) (Cooksey et al., 1964) (Moore and Elliott, 1967) (Jaffrey and Chadwick, 1969) (Clark and Elliott,

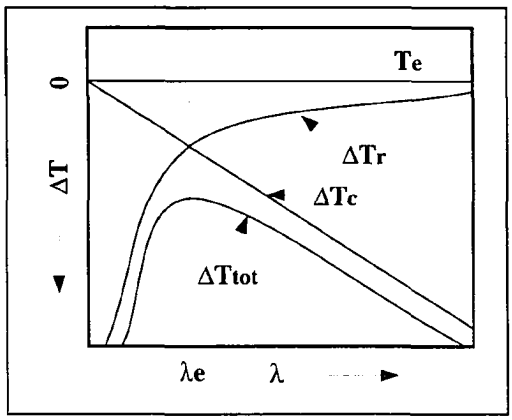

Figure 6. Contributions to the total undercooling during eutectic growth.

1976) have shown that $\lambda = V^{-n} \cdot constant$ for a number of regular eutectics over a wide range of growth rates, although n was found to vary from 0.35 to 0.50. This variance between theory and experiment can be attributed to the assumption originally made by Tiller (1958) that growth occurs with a minimum undercooling at the interface, since this assumption has no fundamental justification. As pointed out by Hunt and Jackson (1966), and later by Seetharaman and Trivedi (1988), a range of lamellar spacings is theoretically possible at a given growth rate such that $\lambda_m < \lambda < \lambda_M$ as shown in Figure 8. It has been shown (Seetharaman and Trivedi, 1988) that if the stable range shown in Figure 8 is entered from $\lambda < \lambda_m$, the steady-state interlamellar spacing value will be slightly larger than that predicted by the minimum undercooling condition, while if the stable range is entered from $\lambda > \lambda_M$, the steady-state interlamellar spacing value will be somewhat less than λ_M and can slowly drift towards some

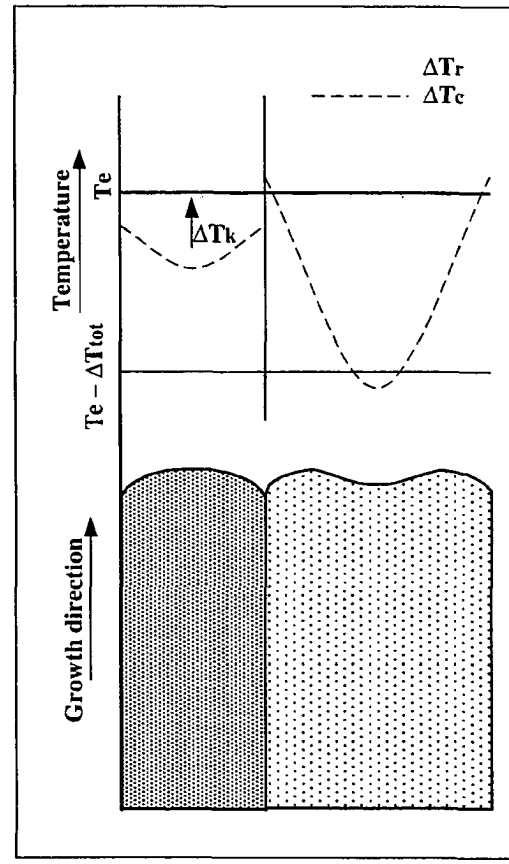

Figure 7. Undercooling contributions along the solid/liquid interface during lamellar eutectic growth.

smaller value. A narrow range of stable interlamellar spacings, resulting from differing solidification conditions, is therefore established.

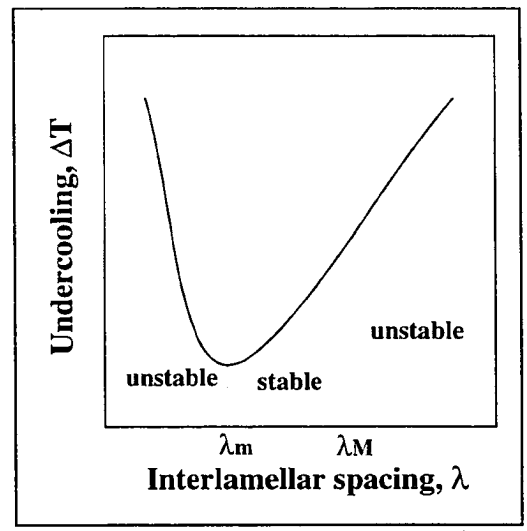

Figure 8. Undercooling as a function of λ for a given velocity. Stable and unstable growth regions are shown.

In the sections to follow, the factors which contribute to ΔT during eutectic growth, namely diffusion ahead of the solid/liquid interface and the interface curvature, are described in some detail.

Eutectic Growth: Diffusion

In their well-known paper, Jackson and Hunt (1966) solved diffusion equations for both lamellar and rod eutectic growth. In their analysis, it is assumed that the lamellar interfaces are flat and the diffusion distance ahead of the interface is much larger than the interlamellar spacing. Under these assumptions, the diffusion equation ahead of the solid/liquid interface during steady-state growth in the z direction is given as:

$$\nabla^2 C + \frac{V}{D}\frac{\partial C}{\partial z} = 0 . \tag{14}$$

This derivation of this equation is not given by Jackson and Hunt, but it can be obtained from Fick's Second Law:

$$\frac{\partial^2 C}{(\partial x')^2} = \frac{1}{D}\frac{\partial C}{\partial t}. \tag{15}$$

Since, according to the Chain Rule,

$$\frac{dC}{dt} = \frac{\partial C}{\partial x'}\frac{dx'}{dt} + \frac{\partial C}{\partial t} \tag{16}$$

and

$$\frac{dx'}{dt} = -R, \tag{17}$$

$$D\frac{\partial^2 C}{(\partial x')^2} = \frac{dC}{dt} = -R\frac{\partial C}{\partial x'} + \frac{\partial C}{\partial t}. \tag{18}$$

Introducing a y coordinate and rearranging gives

$$\frac{\partial^2 C}{(\partial x')^2} + \frac{\partial^2 C}{\partial y^2} + \frac{R}{D}\frac{\partial C}{\partial x'} = \frac{1}{D}\frac{\partial C}{\partial t}. \tag{19}$$

The right hand side of equation 19 is equal to zero when steady state growth is assumed, and therefore this equation is equivalent to equation 14. The solution to equation 14 reduces to

$$C = C_e + C_\infty + B_0 e^{-\frac{V}{D}z} + \sum_{n=1}^{\infty} B_n \cos\frac{n\pi x}{S_\alpha + S_\beta} e^{-\frac{n\pi z}{S_\alpha + S_\beta}} \tag{20}$$

for lamellar growth, where

$$B_0=\frac{C_0^{\alpha}S_{\alpha}-C_0^{\beta}S_{\beta}}{S_{\alpha}+S_{\beta}}\ ;\ B_n=\frac{2}{(n\pi)^2}(S_{\alpha}+S_{\beta})\frac{V}{D}C_0\ \sin\frac{n\pi S_{\alpha}}{S_{\alpha}+S_{\beta}}\ , \tag{21}$$

and

$$C=C_e+C_{\infty}+A_0e^{-\frac{V}{D}z}+\sum_{n=1}^{\infty}A_nJ_0\left(\frac{\gamma_n r}{r_{\alpha}+r_{\beta}}\right)e^{-\frac{\gamma_n z}{r_{\alpha}+r_{\beta}}} \tag{22}$$

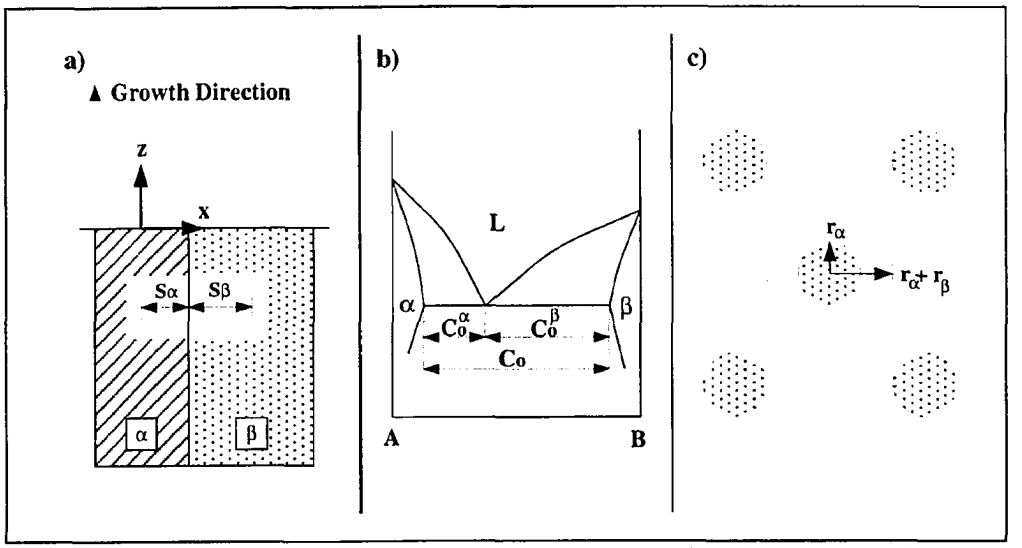

Figure 9. Illustration of terms used in the Jackson and Hunt analysis for a) a planar lamellar interface, b) theoretical eutectic phase diagram, and c) a rod structure.

for rod growth, where

$$A_0=\left(\frac{r_{\alpha}}{r_{\alpha}=r_{\beta}}\right)^2C_0-C_0^{\beta}\ ;\ A_n=\frac{2Vr_{\alpha}}{D}C_0J_1\frac{\left(\frac{\gamma_n r_{\alpha}}{r_{\alpha}+r_{\beta}}\right)}{(\gamma_n^2J_0)^2}\ . \tag{23}$$

Several of the terms used in these equations are defined in Figure 9, and γ_n is approximately equal to $n\pi$. Jackson and Hunt's analysis, and the assumptions therein,

have been shown to be experimentally sound (Mollard and Flemings, 1967b), at least for the case of regular lamellar eutectic growth.

Eutectic Growth: Interface Curvature

Expressions have been derived (Jackson and Hunt, 1966) for the average curvature of both lamellar and rod eutectics. Curvature is dependant on phase boundary geometry and on interlamellar spacing. For the case of lamellae, the curvature is given simply as

$$K = \frac{1}{r(x)} = \frac{1}{S}\int_0^S \frac{dx}{r(x)} = \frac{1}{S}\sin\theta\ , \qquad (24)$$

where S and θ are shown in Figure 10. For the rod morphology where α rods exist in a β matrix, curvatures are given as

$$K_\alpha = \frac{2}{r_\alpha}\sin\theta_\alpha\ ;\ K_\beta = \frac{2r_\alpha}{(r_\alpha + r_\beta)^2 - r_\alpha^2}\sin\theta_\beta \qquad (25)$$

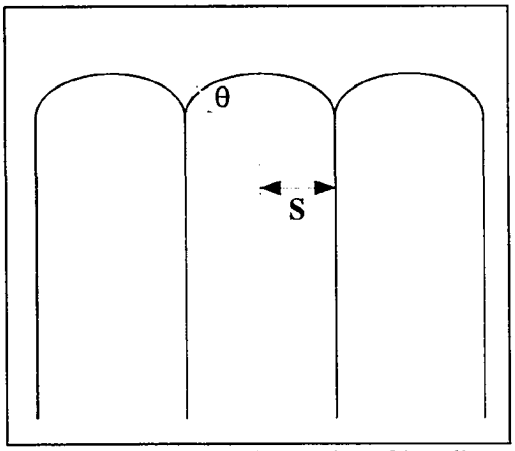

Figure 10. Schematic illustration of lamellar interface showing definition of S and θ. (After Jackson and Hunt, 1966)

The curvature expressions shown above can be combined with the expressions for the average composition at the interface, equations 20 or 22, to obtain the total interface undercooling during lamellar or rod eutectic growth, respectively.

The Eutectic-Dendritic Transition

Competitive Growth Criterion

Hunt and Jackson (1967) were the first to speculate on the theoretical basis for the eutectic-dendrite transition in metallic alloys. Based on prior investigations involving organic systems (Tammann and Botschwar, 1934) (Botschwar, 1934) (Kofler, 1950), they argued that the structure which grows with the highest velocity at a given undercooling (or with the lowest undercooling at a given growth rate) will be preferred and will constitute the solidified morphology. For example, for the isothermal solidification of a binary A-B alloy on the A-rich side of the eutectic, only α dendrites will grow at temperatures greater than the eutectic temperature, T_E (see Figure 11). For temperatures between T_I and T_E, however, both α dendrites and eutectic will exist, with the dendrites growing ahead of the eutectic due to their higher growth velocity. Finally, at temperatures less than T_I, eutectic will outgrow dendrites and will therefore be the only structure to form. Furthermore, it is pointed out in a qualitative manner that the temperature gradient in the liquid, G, does play a role in dendritic and mixed dendritic-eutectic growth. It is speculated that as G increases, the distance that dendrites can grow out ahead of the interface continues to decrease.

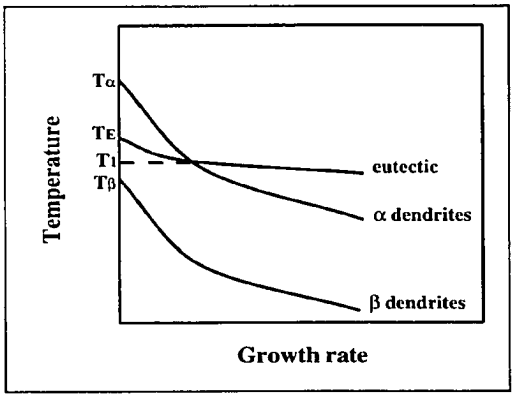

Figure 11. Schematic drawing of the variation in growth rate of the eutectic and of primary dendrites for an alloy rich in component A.

Hunt and Jackson offer no experimental verification of their analysis.

Constitutional Supercooling Criterion

In contrast to Hunt and Jackson, Mollard and Flemings (1967) attempted to show that the dendrite-eutectic transition depends on the constitutional supercooling criterion (CSC). As discussed in the section "Eutectic Growth: Diffusion", the steady-state solute distribution ahead of an advancing solid/liquid interface is given by

$$\nabla^2 C + \frac{R}{D}\frac{\partial C}{\partial x'} = 0 \ , \tag{14}$$

which is schematically represented in Figure 12a. This distribution controls the equilibrium liquidus temperature in the z direction, which is related to the composition by

$$T_l(C_o) - T_l(z) = m(C_o - C(z)) \ . \tag{27}$$

As the solute concentration in the liquid, C(z), decreases ahead of the interface, the liquidus temperature, $T_l(z)$ will increase as indicated by the phase diagram, Figure 12b. Depending on the temperature gradient in the melt, the composition-induced variation in liquidus temperature may result in a region ahead of the solid/liquid interface where the temperature, T_q is actually less than the liquidus temperature, Figure 12c. This region is said to be constitutionally supercooled, thus promoting the growth of interface perturbations into cells or dendrites. The CSC is therefore given as

$$G \prec mG_c \,, \tag{28}$$

where G_c is the solute gradient in the melt which can also be expressed as

$$G_c = (\frac{V}{D})\Delta C_o \,. \tag{29}$$

Accordingly, a planar eutectic interface was expected to be stable when

$$\frac{G}{V} \geq -\frac{m(\Delta C_o)}{D}, \tag{30}$$

or when growth occurs in the presence of a high temperature gradient in the liquid and/or at low growth rates.

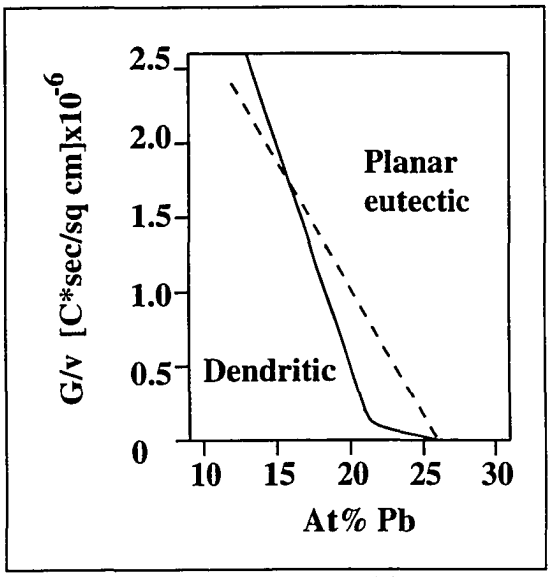

Figure 13. The eutectic-dendritic transition as predicted by the CSC (dashed line) and as determined for the Sn-Pb system (solid line). (After Mollard and Flemings, 1967.)

In a series of directional solidification experiments involving off-eutectic Sn- rich Sn-Pb alloys solidified at growth rates up to 30 E-4 cm/sec and temperature gradients up to 480°C/cm, qualitative agreement was obtained between the CSC predictions and experimental findings (Figure 13). At solute concentrations ≤10at% from the eutectic (26 at% Pb), however, planar eutectic growth was found to persist where significant supercooling was

predicted. The discrepancies between theoretical predictions and experimental results were largely attributed to the fact that the CSC predicts the onset of planar front instability, and not necessarily dendritic growth. However, it can also be argued that

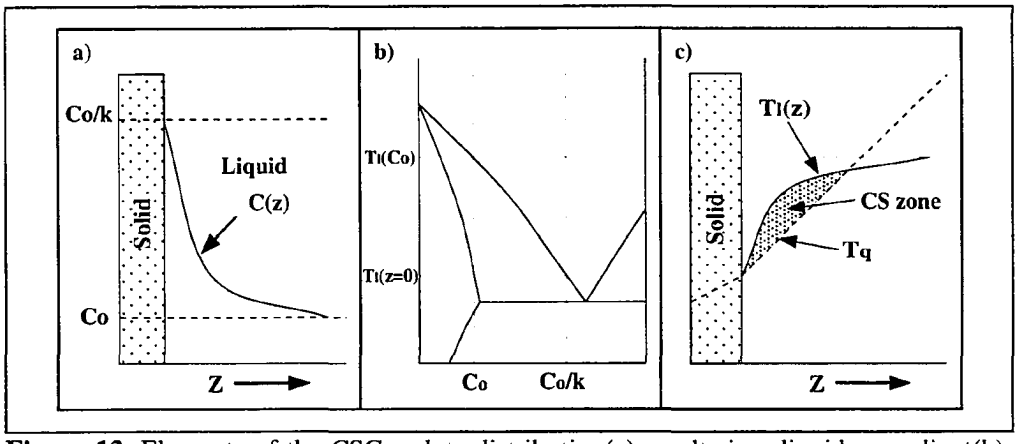

Figure 12. Elements of the CSC: solute distribution(a) results in a liquidus gradient(b) resulting in a supercooled region(c).

the CSC cannot predict the transition to dendrites in an alloy of eutectic composition, since such an alloy will always be constitutionally supercooled. Since the solute buildup ahead of a eutectic interface will result in a decreasing liquidus temperature with distance (as opposed to an increasing liquidus temperature for off-eutectic alloys), such an interface will always grow in the presence of constitutional supercooling. It therefore seems that the competitive growth criterion will be more likely to predict the eutectic-dendrite transition for eutectic alloys, and this is consistent with the work of Jackson (1968).

Jackson (1968) experimentally verified the competitive growth theory proposed by Hunt and Jackson (1967) with the quantitative inclusion of temperature gradient.

In this study, experimentally-determined expressions for the growth rates of Sn-Pb eutectic and Sn dendrites as functions of undercooling are used in order to derive growth rate expressions which take temperature gradient into account. If the calculated dendrite growth rate was greater than the eutectic growth rate, dendrites were predicted to grow ahead of the interface. This analytical treatment was applied to the experimental data determined by Mollard and Flemings, resulting in a much improved correlation between theoretical predictions and experimental findings. Jackson argued that since Mollard and Flemings used high temperature gradients in their experiments, high growth velocities are therefore needed to obtain dendrites according to the CSC, which predicts dendritic growth at low values of G/v (equation 30). High growth rates, in turn, imply that large undercooings ($\Delta T \propto v$) are needed for dendritic growth. Since a negligable undercooling is assumed for cellular or dendritic growth in the CSC derivation, the CSC cannot predict dendrite-eutectic transitions in the presence of a temperature gradient.

The ability of a eutectic or off-eutectic alloy to produce a eutectic or dendritic structure is often discussed in terms of the coupled zone of growth for a particular alloy system. As will be shown in the following section of this review, the structural morphology of a eutectic or off-eutectic alloy is dependent on a number of solidification conditions during the nucleation and growth events.

Coupled Zone Theory

The coupled zone of growth refers to the set of solidification conditions which

will produce a eutectic structure which is free from proeutectic dendrites. Knowledge of this zone can be useful in determining which alloy compositions, solidification rates, and temperature gradients in the melt, can produce desired microstructures. The equilibrium phase diagram alone is not a sufficient reference when predicting solidification morphology, since for certain solidification conditions, wholly eutectic structures can be produced in a wide range of off-eutectic alloys, and for some alloy systems, primary dendrites can be produced at the eutectic composition. This is shown in Figure 14, which contains a schematic illustration of a symmetric coupled zone for a typical normal eutectic. Within the shaded area, the eutectic morphology is most stable and will outgrow dendrites of either primary phase.

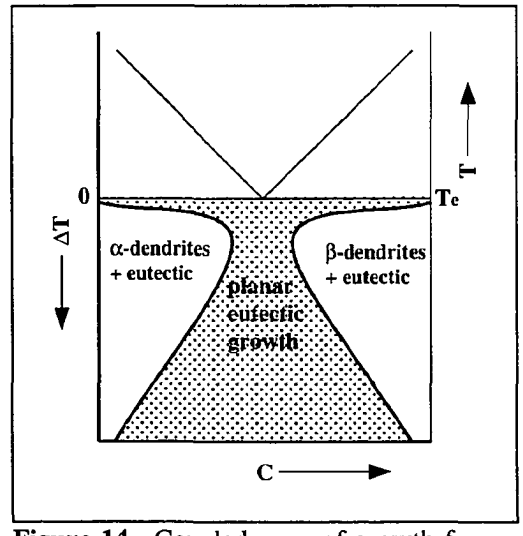

Figure 14. Coupled zone of growth for a normal eutectic system.

In conventional coupled zone theory, the structure which grows with the highest velocity at a given undercooling, or with the lowest undercooling at a given velocity, will be preferred by the system and will constitute the resultant microstructure (Kurz and Fisher, 1979) (Kurz and Fisher, 1989). As discussed in the section on eutectic growth, eutectics will grow with an undercooling given by

$$\Delta T = K_c \lambda V + \frac{K_r}{\lambda} , \tag{10}$$

and will approximately follow the relation

$$\lambda^2 V = \frac{K_r}{K_c} . \tag{13}$$

Substituting λ from equation 10 into equation 13,

$$\Delta T = K_c\left(\sqrt{\frac{K_r}{V K_c}}\right)V + \frac{K_r}{\sqrt{\frac{K_r}{V K_c}}} , \tag{31}$$

and therefore,

$$\Delta T = 2\sqrt{K_c K_r}\sqrt{V}, \tag{32}$$

or

$$\Delta T = \sqrt{V} \bullet constant. \tag{33}$$

Similarly, for dendritic growth, the undercooling is given by (Burden and Hunt, 1974)

$$\Delta T = \frac{GD}{V} - \left(\frac{mVr}{D}\right)(1-k)C_O - \frac{krGD}{V} + \frac{2\Gamma}{r} , \tag{34}$$

which can be simplified to (Kurz and Fisher, 1979)

$$\Delta T = \frac{GD}{V} + \sqrt{V} \bullet constant . \tag{35}$$

By comparing equations 33 and 35, it can be seen that with known solidification conditions, one can predict morphological transitions based on undercooling considerations. Figure 15 illustrates this principle for an alloy of composition C_0 for a eutectic alloy system which is characterized by a symmetrical coupled zone. It is

shown in this figure that for most growth rates, β dendrites grow with the lowest undercooling and are therefore more stable than eutectic or α dendrites. In this case, β dendrites will grow ahead of the eutectic interface since they grow with a lower undercooling. However, since the undercooling associated with β dendrites can be expressed in the form shown in equation 35, the eutectic structure is more stable at very low and high growth rates and will therefore be the preferred morphology even though C_o is not of eutectic composition.

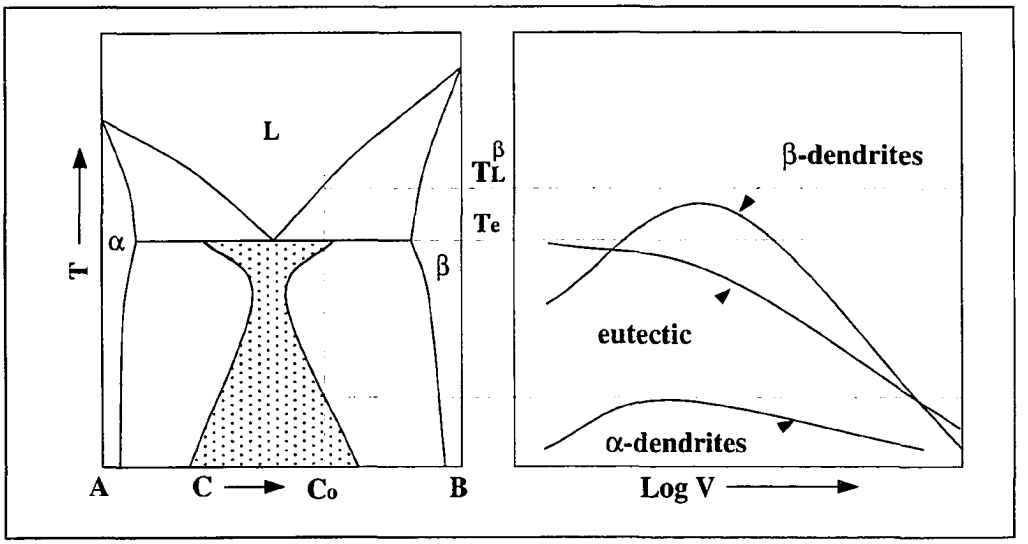

Figure 15. Coupled zone and corresponding temperature-velocity diagram for a normal eutectic system.

In systems where one of the eutectic phases either grows anisotropically or requires a high undercooling for nucleation, a skewed coupled zone may exist. In this case, dendrites of one primary phase may be the most stable form of growth at the eutectic composition or even on the other side of the eutectic composition, where dendrites of the other primary phase would normally be expected to form. This is

schematically illustrated in Figure 16, along with a temperature-velocity plot which can be compared to that for a symmetrical coupled zone as shown in Figure 15.

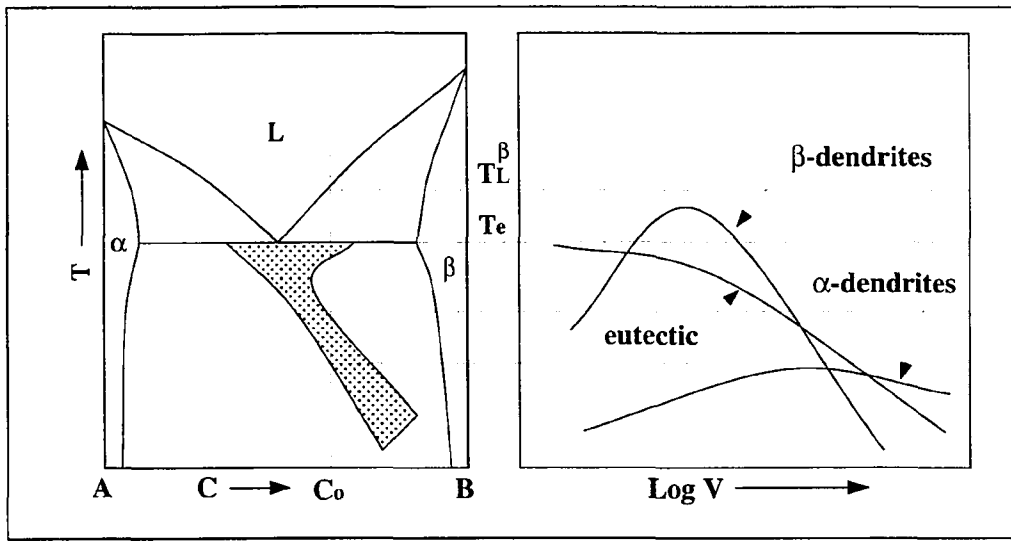

Figure 16. Skewed coupled zone and corresponding temperature-velocity diagram for a eutectic system where one phase grows anisotropically or may require a large undercooling for nucleation.

The Al-Zn Equilibrium Phase Diagram

The Al-Zn phase diagram has been a source of investigation and debate for about a century. Because alloys of this system possess great fluidity and low melting points, they have long been used as casting alloys. Consequently, quantitative information regarding the liquidus line of this system was achieved as early as 1897, at which time Heycock and Neville determined the freezing temperatures for various Al-Zn alloys and identified a eutectic point at 380.5°C and 89 at% Zn. Based on thermal analysis and microscopic examination, Shepherd (1905) verified the eutectic point found by Heycock and Neville, and produced the first complete, although crude, Al-Zn phase diagram. Although the Al solidus line was not determined, the diagram wholly consisted of a eutectic transformation with the eutectic line ranging from approximately 45 to 95 at% Zn. In 1911, Rosenhain and Archbutt (1911) noted that the Al-rich phase decomposes, perhaps in a eutectoid reaction, at 256°C and 60at% Zn. More importantly, however, they suggested a peritectic reaction to occur at 443°C and 60at% Zn, thus intiating a debate that continues to present times. Further investigations (Hanson and Gayler, 1922) (Fuller and Wilcox, 1935) confirmed the presence of the eutectoid decomposition, but many (Fuller and Wilcox, 1935) (Fink and Willey, 1936) (Gayler and Sutherland, 1938) (Ellwood, 1940) disagreed on the basis of various experimental findings obtained through thermal analyses, dilatometry, electrical resistivity measurements, and microscopy, that a peritectic reaction occurs in this system. Futhermore, the Al-rich solid solution was shown to be crystallographically identical to the phase which was previously proposed to be the

result of the peritectic reaction, and the lattice parameter of the solid solution within this extended composition range was found to change only by virtue of changes in composition. These investigators also discovered a miscibility gap within the Al solid solution, yielding the phase diagram which closely resembles the one commonly

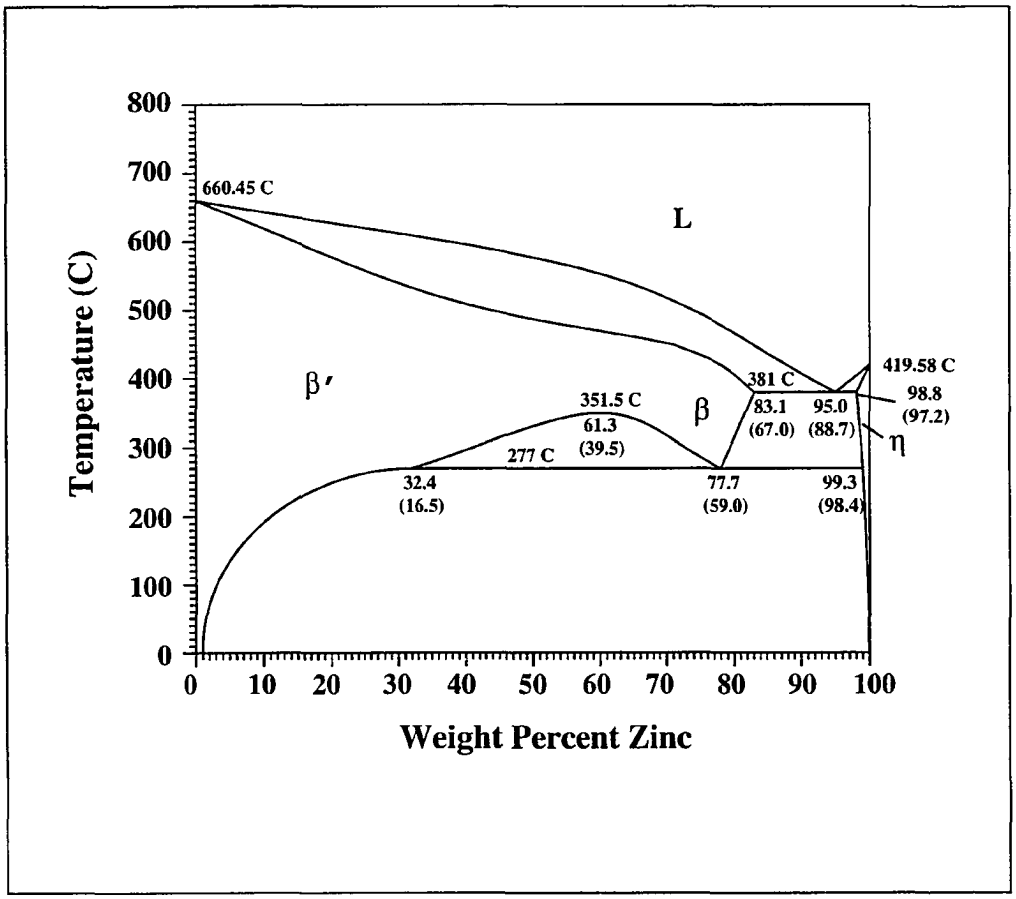

Figure 17. The Al-Zn equilibrium phase diagram. Atomic percent compositions given in parentheses.

accepted today (Figure 17). Unfortunately, more recent studies (Goldak and Parr, 1963) (Nayak, 1973) give credence to the prospect of the peritectic reaction and an adjacent, narrow two-phase region which intersects the Al solidus and the miscibility

gap. Although the experimental techniques used by these investigators, which include high-temperature x-ray diffractometry and quantitative thermal analyses, seem plausible, the proposed peritectic reaction and subsequent two-phase field are not theoretically sound because i) the presence of a two-phase field is not consistent with, and cannot be joined to, the well-established miscibility gap; and ii) the two-phase field separates two crystallographically identical phases of nearly equal composition

Table I. Phase transformations in the Al-Zn system. (After Murray, 1983)

Phase Transformation	Composition, wt% (at% Zn)	Temperature (°C)	Transformation Type
$L \rightleftharpoons \beta+\eta$	95.0 (88.7)	381	Eutectic
$\beta \rightleftharpoons \beta'+\eta$	77.7 (59.0)	277	Eutectoid (Monotectoid)
$(Al) \rightleftharpoons \beta'+\beta$	61.3 (39.5)	351.5	Critical
$L \rightleftharpoons (Al)$	0 (0)	660.45	Congruent
$L \rightleftharpoons \eta$	100 (100)	419.58	Congruent

(within 1 at%), and this is not thermodynamically feasible. The phase diagram shown in Figure 17 is therefore the most widely accepted for this system, although questions still remain about the presence of a peritectic reaction.

The solid phases present in the Al-Zn system include β', β, and η. β' and β represent the Al- and Zn- rich portions, respectively, of the Al fcc solid solution. The solubility of Zn in the Al solid solution increases with temperature to 16.5 at% at the

eutectoid temperature (277°C), and 67 at% at the eutectic temperature (381°C). η is the cph Zn phase, which has a maximum Al solubility of 2.8 at%, which occurs at the eutectic. This solubility decreases to 1.6 at% at the eutectoid temperature and 0.07 at% at room temperature. The transformations involving these phases are summarized in Table I.

The Al-Zn Eutectic

As noted from the phase diagram (Figure 17) (Table I), the eutectic transformation in the Al-Zn system occurs at 381°C and 95.0 wt% (88.7 at%) Zn. This eutectic is classified as a normal eutectic (Hunt and Jackson, 1966) since both eutectic phases have low entropies of fusion and therefore grow isotropically with atomically rough interfaces (no facets). The eutectic morphology is usually that of lamellae, but since the volume percent second phase is approximately 30%, the structure readily breaks down into rods when the solid/liquid interface becomes curved for any reason, i.e. changes in growth direction, cell formation due to impurities, etc.. (Hunt and Chilton, 1963).

Non-reciprocal nucleation characteristics have been observed for the Al-Zn eutectic. Spittle (1977) speculates that since Al-rich β dendrites in off-eutectic alloys are typically surrounded by Zn-rich η halos, Al must be a better nucleant of Zn than vice versa. The expected nucleating abilities of the primary phases based on the interfacial energy considerations as discussed by Sundquist and Mondolfo (see the section "Eutectic Nucleation") support the notion that Al is a better nucleant than Zn, since the surface energy of Al is greater than that of Zn. To the contrary, however, it can be argued by rationale put forth by Chadwick (1963) that the presence of η halos around β dendrites indicates that Al is a poorer nucleant of Zn than vice-versa. If the β dendrite does not serve as a heterogeneous nucleation site for η, the liquid surrounding the dendrite will become enriched in Zn as the dendrite grows. This enriched zone will be highly undercooled, resulting in the nucleation of η within this

zone. Based on these conflicting theories, the significance of the η dendrites on the nucleating abilities of the primary phases therefore warrants further investigation.

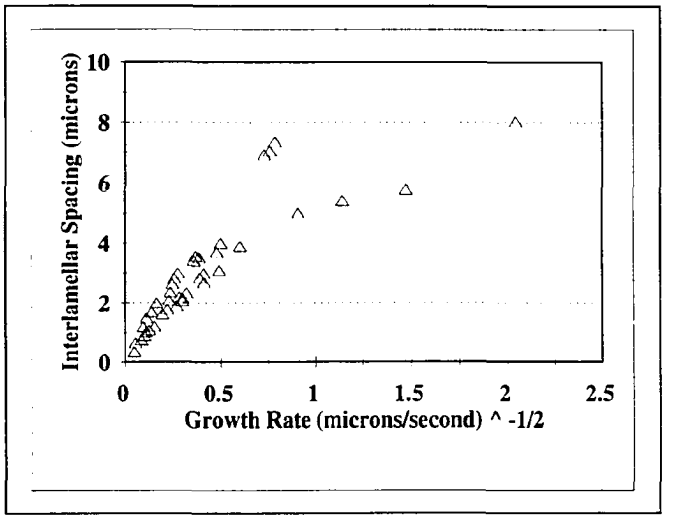

Figure 18. Interlamellar spacing of the Al-Zn eutectic as a function of $V^{-1/2}$.

In an extension of the nucleation characteristics suggested by Spittle, it is argued that the coupled zone for this system is asymmetric and skewed towards the Al-rich side of the Al-Zn phase diagram. Although the link between nucleation characteristics and the placement of the coupled zone is not clear since coupled zone theory is based on growth considerations (Kurz and Fisher, 1979), further evidence of such a zone is presented by Porot et al. (1987), who found that for rapid cooling rates, Zn-rich η dendrites can be formed even on the Al-rich side of the eutectic.

Several directional solidfication studies have been conducted with Al-Zn eutectic alloys (Chadwick, 1963b) (Cooksey et al., 1964) (Moore and Elliott, 1969) (Livingston et al., 1970) (Tuček et al., 1986). The resulting interlamellar spacing data compiled from these investigations are shown in Figure 18, which plots interlamellar spacing as a function of $V^{-1/2}$. As suggested by eutectic growth theory which predicts

$\lambda \propto V^{-1/2}$, a linear relationship is expected in this plot. However, it seems that the data is better represented by the relationship $\lambda \propto V^{-1/3}$, as shown in Figure 19. As discussed in the section on "Eutectic Growth: Interlamellar Spacing and Interface Undercooling", the predicted theoretical relationship between interlamellar spacing and growth rate assumes that growth occurs as the extrenum condition, and this assumption may not be valid for a given alloy system and set of solidification conditions. It can therefore be said that the Al-Zn eutectic does not grow exclusively at the extrenum condition, at least for the solidification conditions used in the cited studies.

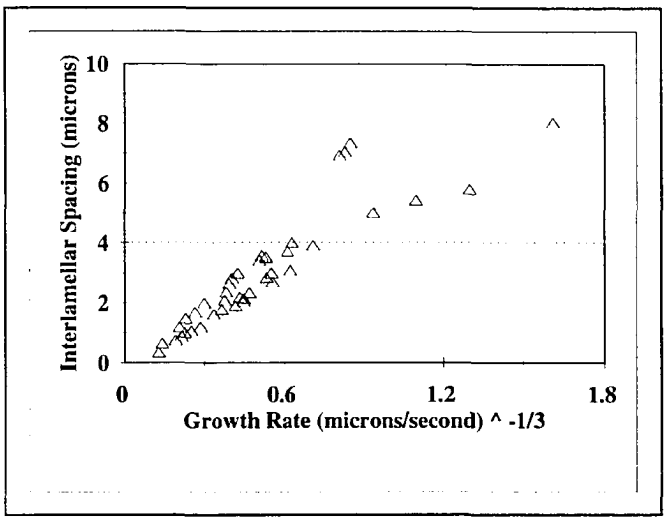

Figure 19. Interlamellar spacing of the Al-Zn eutectic as a function of $V^{-1/3}$.

Hot-Dip GALFAN Coatings

Coating Properties

As a hot dipped Zn-based coating containing approximately 5wt% Al and up to 0.10% mischmetal (see Table II), Galfan offers excellent corrosion resistance, formability, paintability, and cathodic edge protection (Radtke and Herrschaft, 1983) (Mäkimattila, 1986) (Roman, 1989) (Mathieu et al., 1991). Formability, which is superior to that of conventional galvanized steel sheet and wire, can be attributed to the absence or limited formation of a brittle intermetallic layer at the coating/substrate

Table II. GALFAN alloy ingot chemical requirements, in weight percent, according to ASTM B750-85.

Al	Ce+La	Fe	Si	Pb	Cd	Sn	Other	Zn
4.7-6.2	0.03-0.10	0.075 max	0.015 max	0.005 max	0.005 max	0.002 max	0.04 max	bal

interface, and the ductile nature of the eutectic structure typical to the coating (Radtke and Herrschaft, 1983) (Mäkimattila, 1986) (Roman, 1989) (Mathieu et al., 1991) (Lamberigts et al., 1991). The mischmetal additions (Ce and La) increase the fluidity and wettability of the Galfan bath, and enhance the intergranular corrosion resistance of the coating. Although there are numerous uses for Galfan and the demand for this coating continues to increase, (Roman and Lynch, 1989) Galfan may not be suitable for some applications which have stringent surface requirements because the coating often contains small surface depressions. The factors which contribute to the smoothness of the coating remain unclear, but the problem has been associated with grain boundaries and has been found to be affected by solidification conditions

(Lamberigts et al., 1990).

Denting in GALFAN Coatings

GALFAN coatings are often characterized by dents which can be as deep as 20 microns. The resulting rough surface appearance often renders the coating improper for many applications. This problem has been thought to be associated with the Zn-Al eutectic lamellar morphology, with dents occurring at the junction of differently oriented eutectic cells. In addition, preliminary experiments at Lehigh (Marder, 1992) indicate that the denting problem is related to solidification shrinkage and cracking, with possible contributions from impurity segregation. Denting has been observed at aluminum concentrations of 4.0-7.0 wt% and quantified with the use of mechanical scanning microscopy and Fourier-modified measurement techniques. Roughness has been found, however, to be most severe at the eutectic composition (Hirose, 1985). Past efforts to remedy the denting problem have included (1) reductions in aluminum concentration, and (2) increased coating solidification rates. By the former method, large zinc-rich particles form across the coating thickness and the eutectic morphology formation is therefore limited (Lamberigts et al., 1991). Although the depth of denting can be slightly decreased by this method, the resulting coating may possess inadequate corrosion resistance in humid environments and suffer a considerable reduction in ductility when compared to eutectic GALFAN. By the second method, i.e. increased solidification rates, the zinc-rich globules typical to GALFAN coatings are smaller and more numerous, and act to inhibit interlamellar dent formation. In addition, the

interlamellar spacing of the eutectic morphology and the subsequent susceptibility to denting is decreased at higher cooling rates. Moderate reductions in dent depths have been attained by this technique but the number of dents were increased by as much as 10-fold.

In addition to altering solidification conditions, the use of IF steel as GALFAN substrate material has been suggested to reduce the depth of interlamellar denting (Lamberigts et al., 1991) (Mathieu et al., 1991). The resulting dents are much more shallow than those achieved by the two techniques discussed above. Dent depths are reduced by up to 50% when compared to those found when traditional ELC steel is used as substrate. The cause of dent depth reduction is not clear, but is thought to be associated with coating/substrate interactions. Although these findings seem promising, a more recent investigation (Lamberigts and Leroy, 1992) has shown that there is no apparent effect of the steel composition on surface denting when comparing IF and ELC steel substrates. Instead, surface roughness was found to be weakly related to GALFAN dip temperature.

Solidification Process and Surface Defects

The GALFAN solidification process can be envisioned by inspection of the coating surface. When etched to reveal the dendritic structure of the proeutectic zinc, it is seen that some of these dendrites serve as nucleation sites for the eutectic nodules (Figure 20). The remaining dendrites exist within eutectic nodules, and are encompassed by eutectic cells which grow around them.

When the coating surface is observed with brightfield illumination, dents seem to be arranged at grain boundaries as indicated in Figure 21. Such dents were found by laser scanning microscopy techniques to be typically 10-15μm deep relative to the highest adjacent points on the coating surface. It should be noted, however, that the depth of such dents will be obviously dependent on the thickness of the coating, since a dent cannot be deeper than the thickness of the coating itself. It can be concluded by inspection of Figures 20 and 21 that denting occurs only at eutectic nodule boundaries and triple points. One such area is shown in Figure 22, which shows a depression at the triple point, and what appear to be cracks extending along the boundaries of the adjoining nodules. A higher magnification triple point image (Figure 23) further supports these observations.

Figure 20. Etched surface Galfan structure. Indicated proeutectic zinc dendrite has served as a eutectic nucleation site.

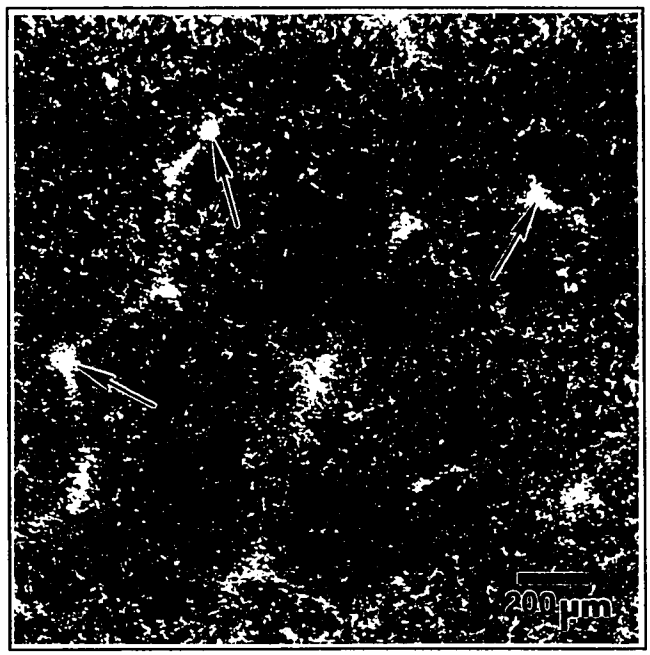

Figure 21. Galfan surface appearance as observed with stereomicroscopy and brightfield illumination. Dents are indicated.

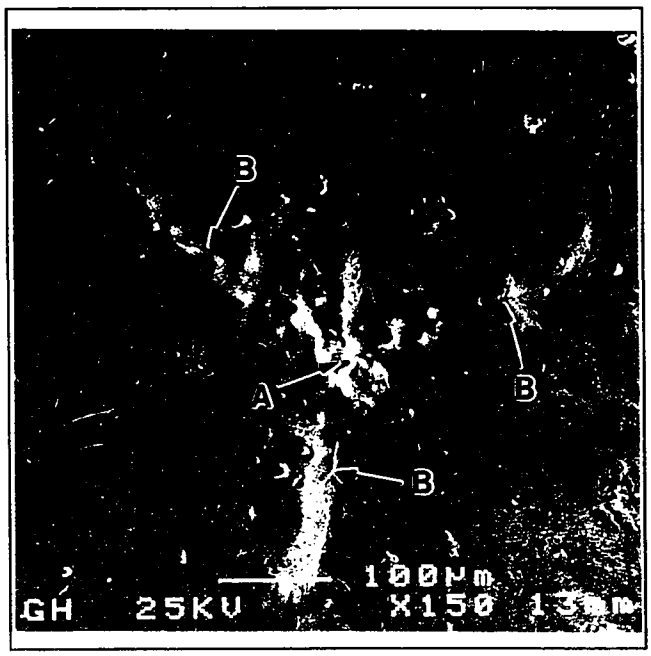

Figure 22. Surface depression (A) at triple point and associated cracks (B) along grain boundaries on Galfan surface.

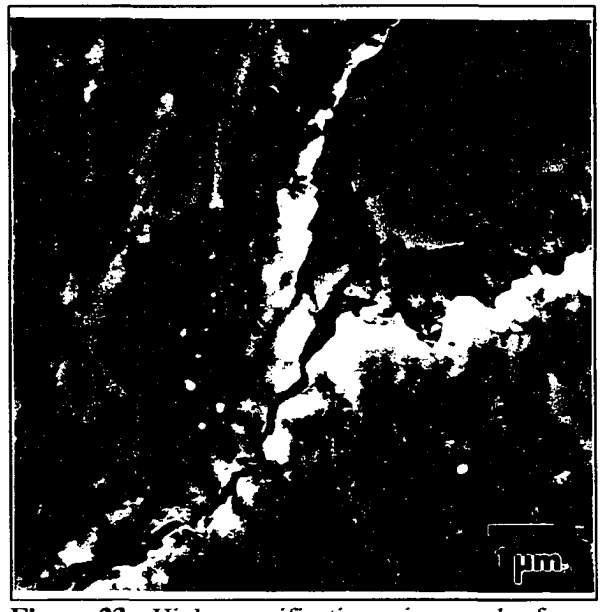

Figure 23. High magnification micrograph of a dented triple point and grain boundary cracks on Galfan surface.

Zn-5%Al-Mischmetal Alloy Solidification

There have been some interesting correlations between the surface defects found in Galfan coatings and those produced from the solidification of Galfan alloy (Zn-5%Al-mischmetal) in the absence of a reactive substrate (Bluni and Marder, 1993). The first is that cracking at eutectic nodule junctions and the denting at triple points as sometimes found in commercial Galfan were successfully simulated. These phenomena can be seen in Figures 24 and 25, respectively. Because of these findings, it can be concluded that surface depressions may be influenced by, but are not a direct result of, substrate interactions. Therefore, the fundamental cause(s) of denting must

be associated with the solidification of the alloy, regardless of whether it is applied as a steel sheet coating. The second finding is that impurity particles were often observed adjacent to nodule boundaries, as can be seen in Figure 26. These impurities were identified as lead by EDS techniques; no other impurities could be detected in these regions. The presence of these particles at nodule boundaries can be explained by the limited solubility of Pb in Zn and the monotectic transformation in the Zn-Pb system (Figure 27). Hence during the solidification process, Pb will be continuously rejected into the melt resulting in the segregation of impurity-rich, low melting point material to grain boundaries.

Since Pb segregation was found for the Zn-5%Al-mischmetal alloy, the EPMA was used to determine the Pb concentration across a surface region of commercial Galfan. The results are shown in Figure 28, which presents a micrograph of the coating surface used for analysis and a plot of the resultant Pb concentration data. The line superimposed on the micrograph represents the path over which concentration data was obtained, in 1μm intervals. By comparing the coating microstructure with the plot, which is drawn to scale, it can be seen that the Pb concentration at the triple point (indicated as "A") is approximately 0.3wt%, or 60 times the maximum allowable concentration as designated by ASTM B750 (see Table II). Other Pb concentration spikes are noted at primary Zn dendrite boundaries (indicated as "B"), also due to the limited solubility of Pb in Zn.

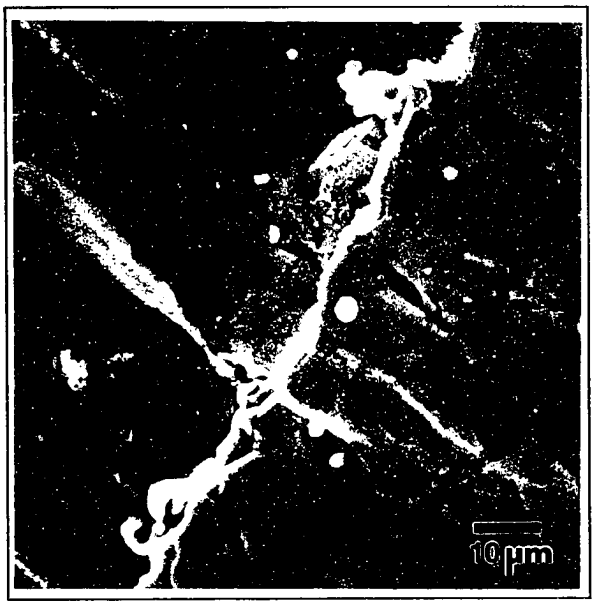

Figure 24. Cracking at a eutectic nodule boundary in Zn-5%Al-mischmetal alloy.

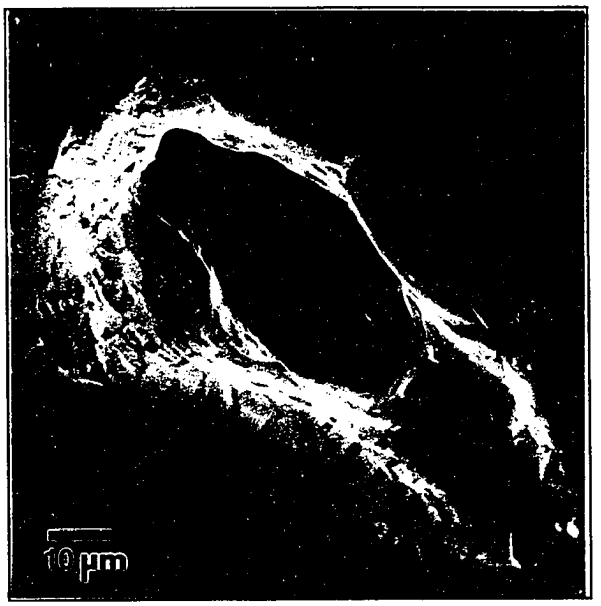

Figure 25. Surface depression at a triple point on Zn-5%Al-mischmetal alloy.

Figure 26. Lead segregation to eutectic nodule boundaries in Zn-5%Al-mischmetal alloy.

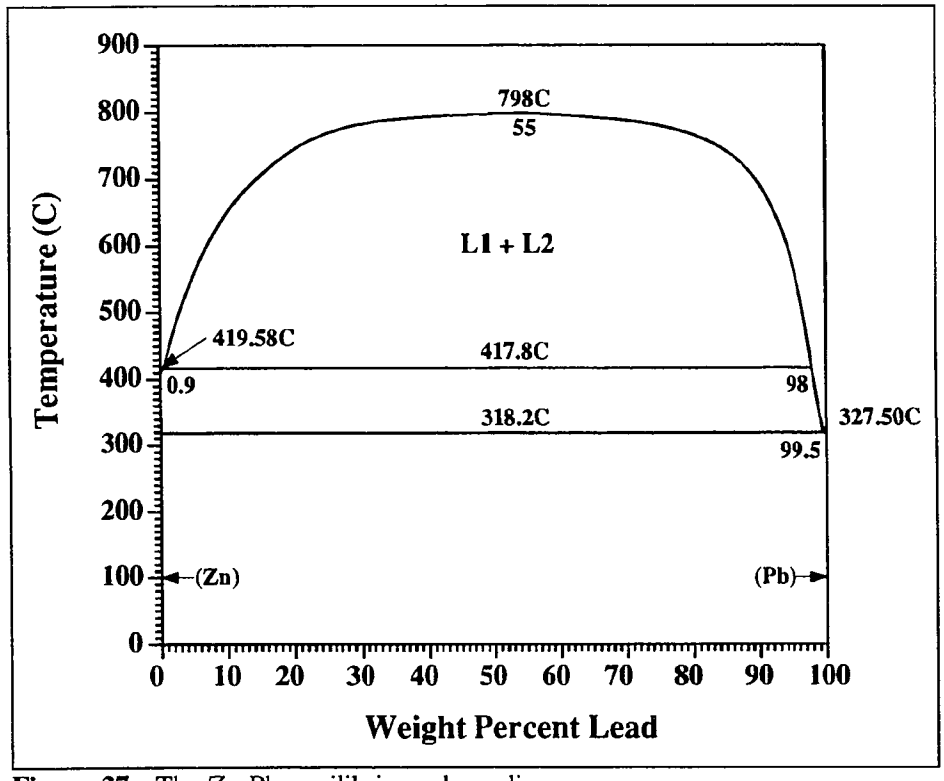

Figure 27. The Zn-Pb equilibrium phase diagram.

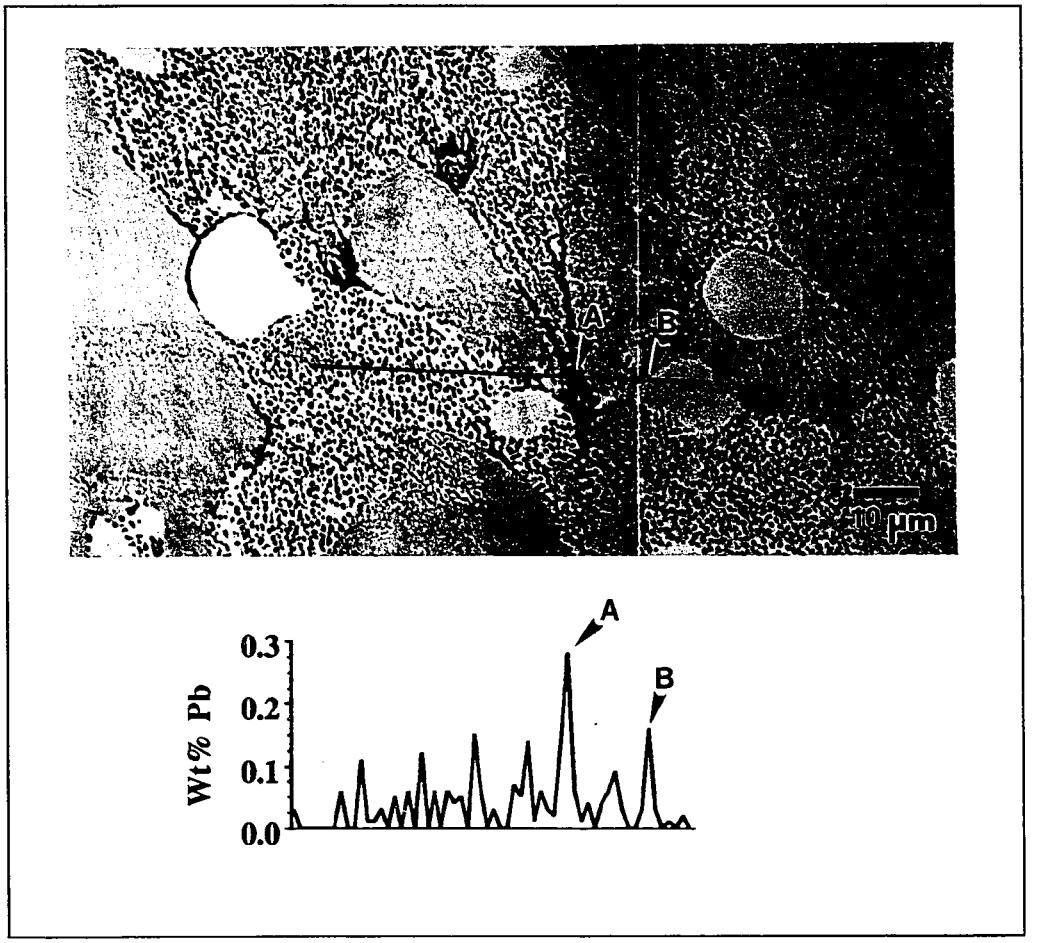

Figure 28. Polished Galfan surface (top) and Pb concentration profile (bottom). The line on the micrograph represents the path of EPMA analysis. (A=triple point; B= primary Zn dendrite)

Mechanism for dent/crack formation in commercial Galfan coatings

Using the information obtained from the commercial Galfan characterization and the Zn-5%Al-mischmetal solidification study, a mechanism for denting/cracking is proposed as schematically illustrated in Figure 29. During the solidification process, the liquid metal is quickly consumed due to the relatively large volume changes

associated with the solidification of Zn and Al (4.7% and 6.5%, respectively). As a result, there will be a shortage of liquid between two (or three) adjacent growing eutectic nodules and upon impingement, the interface will be subsequently curved creating a surface depression. The dents often observed in Galfan are attributed to this phenomenon. In addition, because impurities such as Pb are continuously rejected into the melt during the solidification process, the resulting grain boundary areas should therefore be impurity-rich and weak in comparison to the bulk coating. When stresses are induced from shrinkage due to any further solidification and/or cooling, cracking will occur within these weakened grain boundaries. The occurrence of shrinkage cavities, cracks, and impurity segregation at grain boundaries in commercial Galfan can be seen in Figures 21, 23, and 28, respectively.

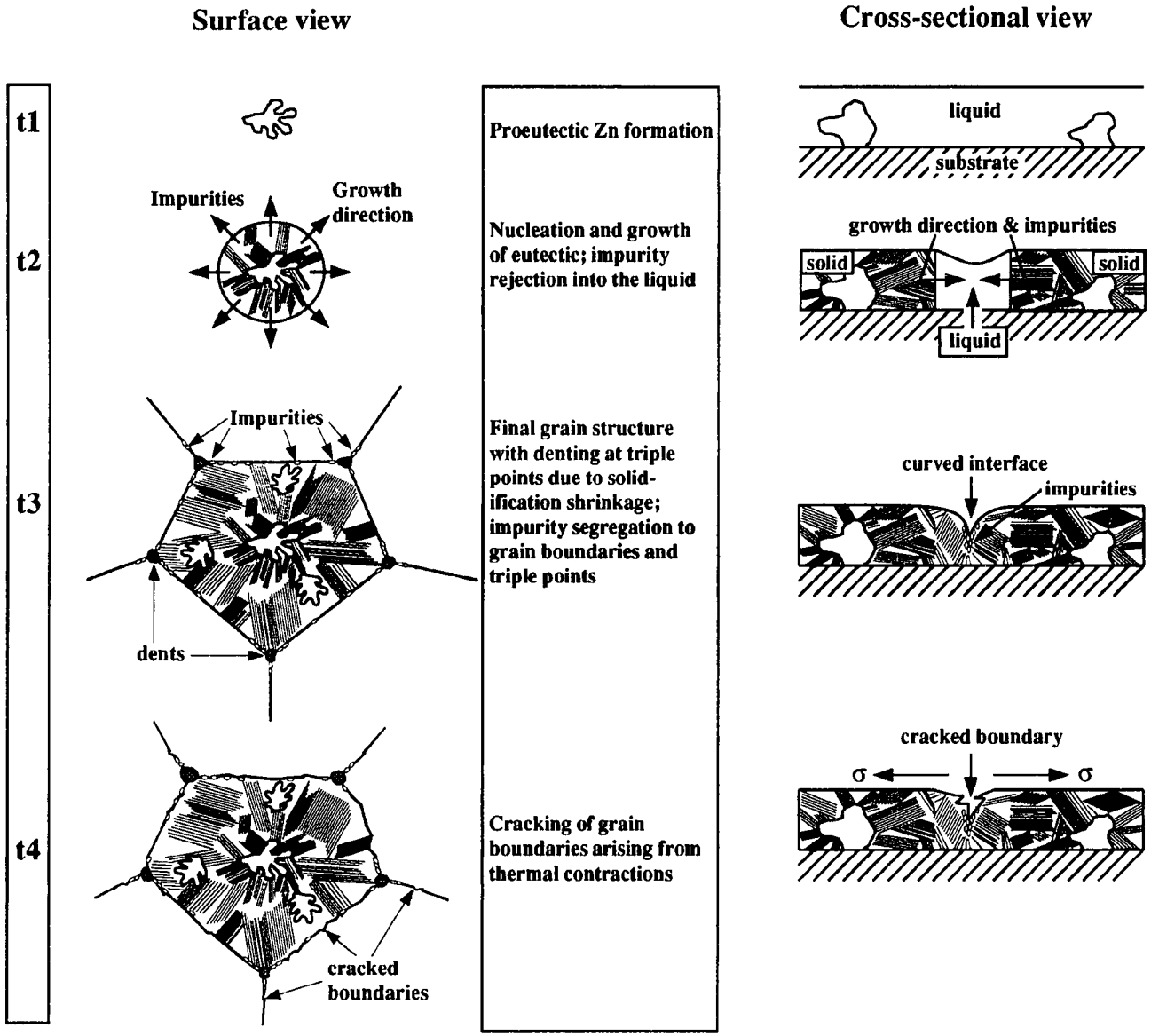

Figure 29. Proposed Galfan solidification mechanism, including dent and crack formation.

Impurity Segregation and Solidification Defects

During alloy solidification, any impurities which are not soluble in the newly forming solid are rejected into the liquid ahead of the growth front. As discussed in the section, "The Lamellar-Rod Transition", such impurity rejection may result in a transition from a planar to a cellular solidification front, any may further induce a transition in eutectic morphology from lamellae to rods. One further implication of impurity rejection is the resulting grain boundary segregation which occurs either at the edges of cells or grains that grow adjacent to each other, or at interfaces which impinge upon each other.

The segregation of impurities to grain boundaries may or may not have adverse effects on the bulk alloy properties, but it can result in solidification cracking, or "hot" cracking, as often discussed in the welding literature. Although most of the research on this topic has been conducted with stainless steels, solidification cracking can occur in any alloy system as long as i) impurity-rich, low melting point material exists at grain boundaries, and ii) tensile stresses result from the solidification and/or cooling process. When low melting point material accumulates at the grain boundaries, it remains as a liquid at temperatures well below the alloy solidification point. This allows contraction stresses to substantially increase before solidification of the grain boundary material can take place. Eventually, the strain across adjacent grains becomes great enough to rupture the grain boundary material (Davies and Garland, 1975). This process is somewhat dependant on grain size (Davies and Garland, 1975); as grain size increases, the solute or impurity-rich boundary layers ahead of advancing

solidification fronts increase in thickness. The result is wider intergranular regions which are more susceptible to solidification cracks.

In addition to hot cracking, an additional possible defect brought about by the solidification process is shrinkage cavity formation. This is simply due to the volumetric contractions associated with the transformation of the bulk alloy from the liquid to the solid state (Davies and Garland, 1975). Like solidification cracking, cavity formation has been associated with stainless steels (Kujanpää, 1984), but it can occur in any alloy where there is a large negative volume change upon solidification.

One or both of the above mentioned solidification defects may contribute to the denting problem in GALFAN coatings. To determine this with certainty, controlled experiments involving the Al-Zn solidification process and the effects of impurities must be conducted.

EXPERIMENTAL PROCEDURES

Al-Zn Alloy Fabrication

Master alloy ingots of eutectic and off-eutectic Al-Zn alloys were made by combining raw materials into 4mm ID x 6mm OD quartz tubes. The raw materials were in the form of 1-3mm Zn shot (99.9999% purity) and 1.0mm diameter Al wire (99.999% purity), both obtained from AESAR/Johnson Matthey. Once weighed to a specific alloy composition, the elements were encapsulated into the above mentioned tubes by evacuating to <50 millitorr and backfilling with pure argon. Each encapsulation typically contained 2-5g of raw materials. After encapsulation, the alloys were placed in a convection furnace at 450°C such that the Zn shot melted and surrounded the Al wire pieces, resulting in a compact specimen. To complete melting and ensure solute homogenization, encapsulations were either heated to above 700°C and physically shaken during solidification, or re-melted with the use of an induction furnace. All alloy ingots were subsequently weighed to quantify any Zn evaporation which may have taken place during melting procedures, and a sample population of these ingots was metallographically examined before test procedures in order to observe resultant microstructures and detect any alloy inhomogeneities.

DSC Sample Preparation & Analysis

Master alloy ingots containing 92-98wt% Zn in 1 wt% increments were sectioned into 50μm discs using a low-speed saw and diamond-impregnated copper

cutting wheel. Additional alloys made and sectioned into samples contained 94.5wt% and 95.5wt% Zn. Similar to a previously developed technique (Sutliff, 1990), these discs were melted on a hot plate between two glass microscope slides and "squeezed" to form a thin, smooth film. Using this film, a Gatan disc punch was used to make 3mm diameter samples which typically weighed 3-15mg and were used for differential scanning calorimetry (DSC) analysis. Glass discs of the same diameter were made from cover slips using a Gatan ultrasonic cutter. As shown in Figure 30, each alloy sample was placed between two of these glass discs during the DSC melting and solidification procedure in order to avoid i) interactions between the sample and the Al pan, and ii) Zn evaporation.

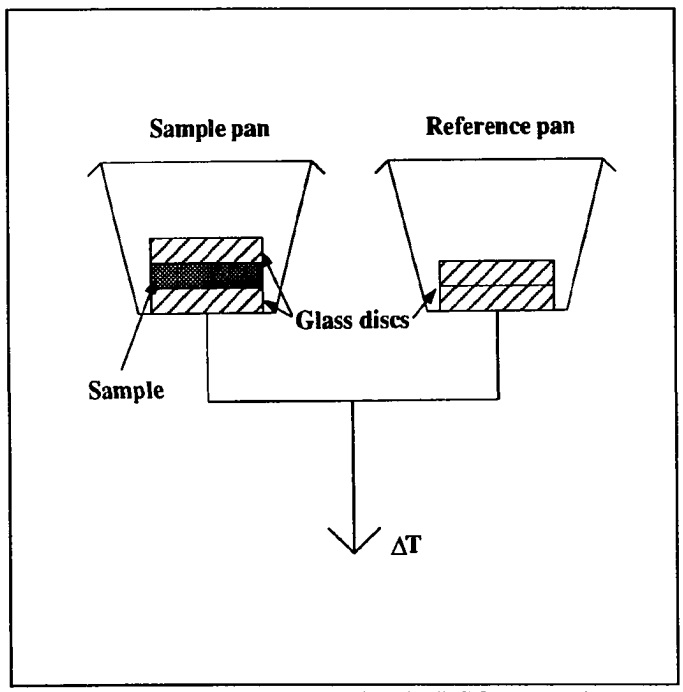

Figure 30. Sample configuration in DSC measuring cell.

During analysis, a Mettler differential scanning calorimeter was used to heat the samples into the liquid phase, hold for a period of time, and cool at rates varying from 1 to 80 K/minute. The hold times were sufficient to ensure homogeneity in the liquid prior to cooling. For example, hold times were typically as long as 6 minutes, which according to a diffusion coefficient of 2.04E-9 m/s^2 (Liu and Jones, 1992), would allow a solute atom to migrate approximately 860μm. Since preexisting proeutectic dendrites in the as-cast samples for all compositions were measured to be on the order of tens of microns in size, the hold times are considered justified. The DSC was periodically calibrated, and on each occasion that the DSC was used for analysis, the solidification temperature of a pure Zn sample was determined by cooling at 1 K/min so to measure any offset temperature by which to adjust the data of that day. To ensure reproducible results, no fewer than 3 samples of each composition and cooling rate were used to compile DSC data.

The DSC was used to obtain solidification temperatures and thermodynamic data for eutectic and off-eutectic Al-Zn alloys. Here, the difference in temperature is monitored between an empty reference sample holder and a sample holder containing the sample to be analyzed (Figure 30) as the heat input to the measuring cell is controlled by a predetemined linear temperature program. As shown in Figure 31 for the case of solidification, the temperatures of the reference (T_r) and the sample (T_s) necessarily lag behind that of the furnace (T_c) to permit a heat flow from the reference and sample. At the solidification temperature (T_f) there will be a significant ΔT between the reference and sample due to the associated heat of fusion.

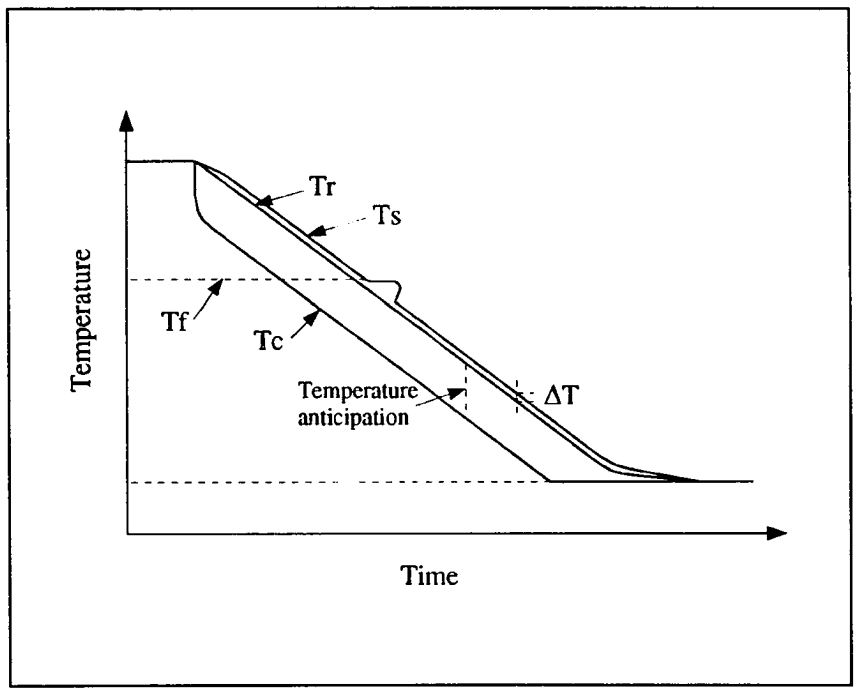

Figure 31. DSC temperature profiles during cooling and sample solidification.

The actual ouput from the DSC cell is a graphical measurement of heat flow to or from the sample, which is related to both the temperature difference between the sample and reference and the thermal resistance of the solid-state connection between the two. An example of a DSC trace obtained for the solidification of an off-eutectic Al-Zn alloy is shown in Figure 32, which illustrates the heat flow associated with the solidification of proeutectic and eutectic from the liquid phase. As is well known in thermal analysis (Brown, 1988), the transition temperature, or nucleation temperature in this case, is determined by the intersection of the trace baseline and the tangent of transformation curve. This procedure is shown graphically in Figure 33. In addition

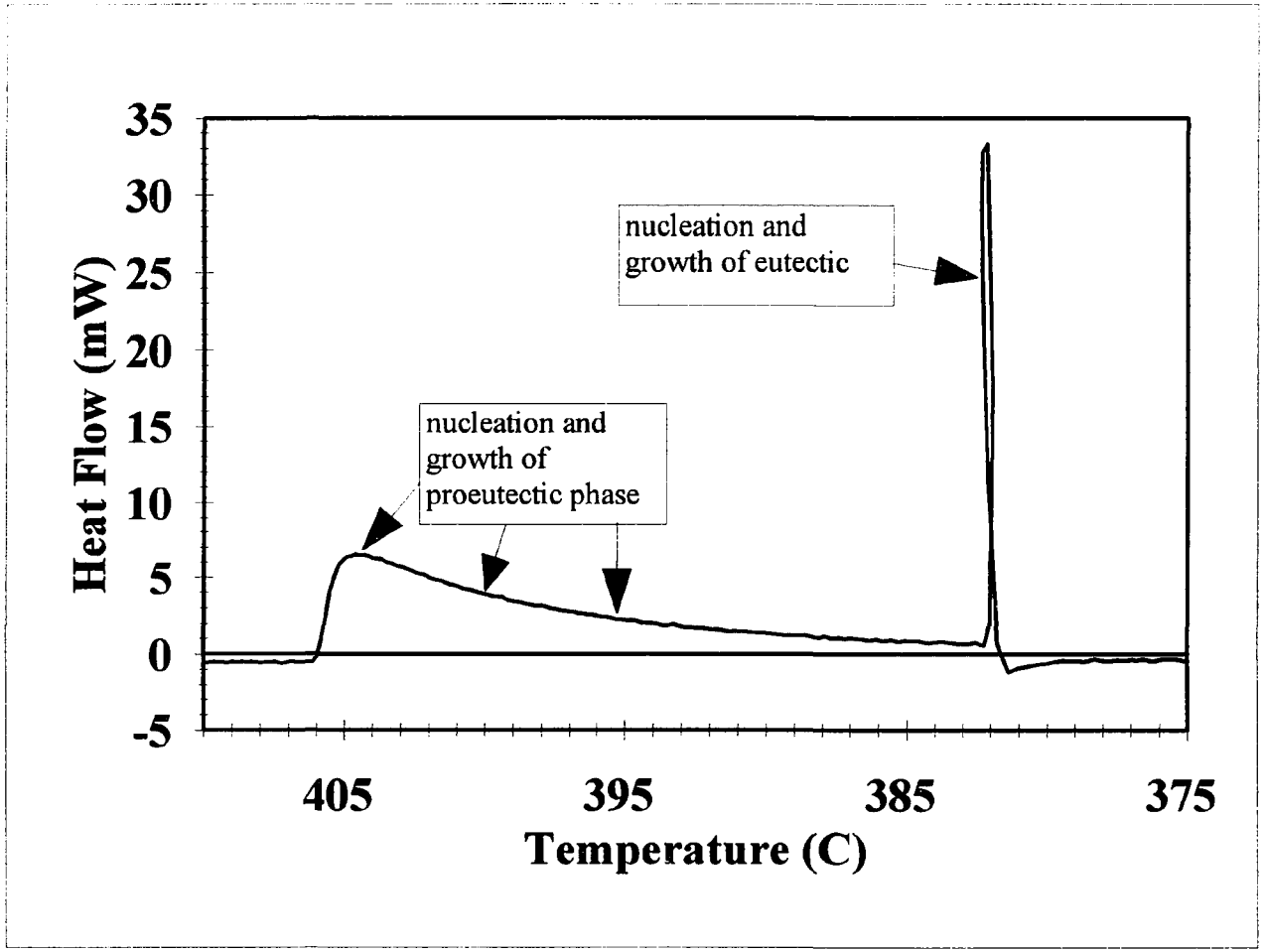

Figure 32. Typical heat flow trace as determined with the use of differential scanning calorimetry during the solidification of an off-eutectic alloy.

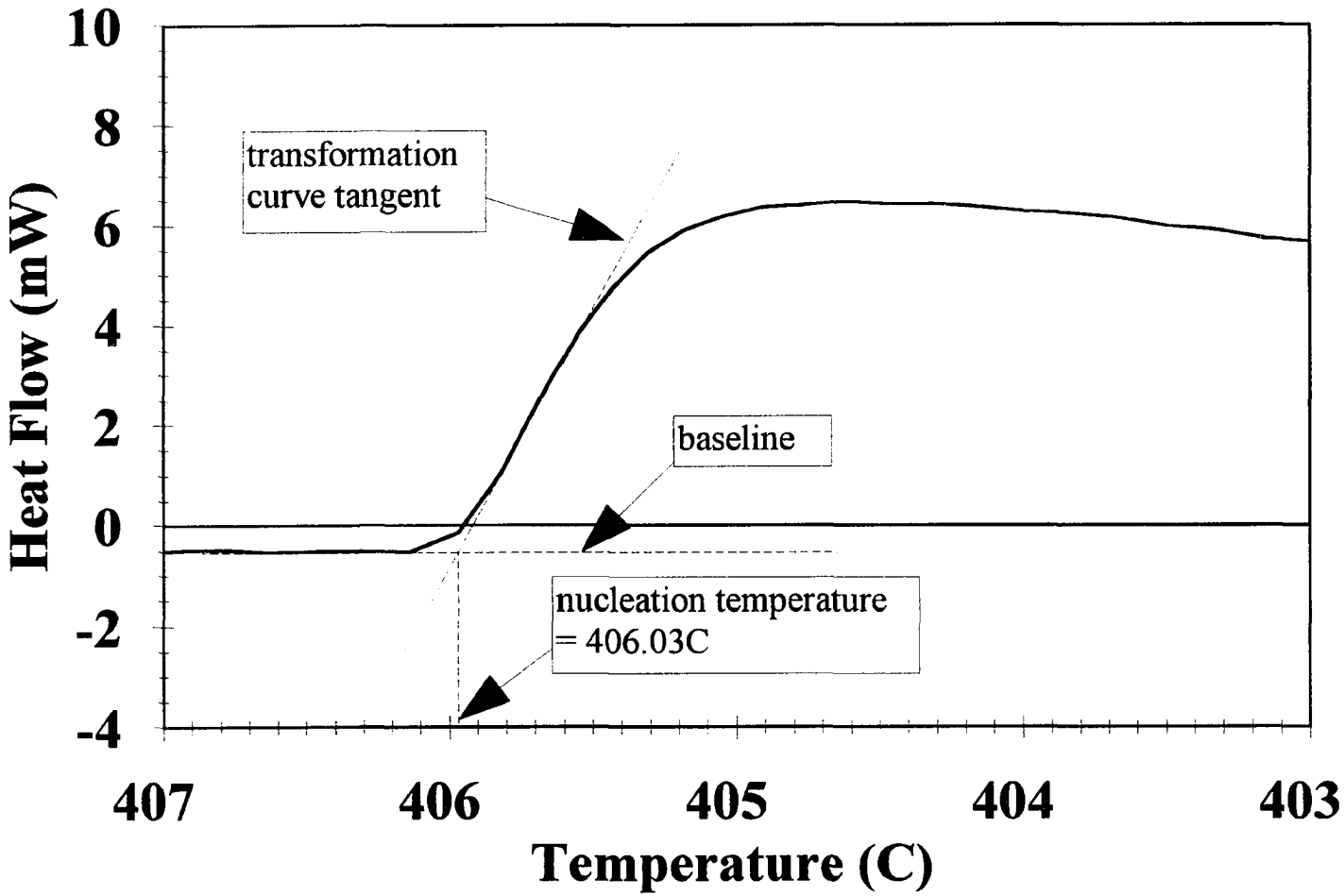

Figure 33. Schematic illustration of the method used to determine transformation temperatures from DSC plots.

to tranformation temperatures, the heat of reaction can be determined from a DSC trace, since in general,

$$\Delta H = \int_{t1}^{t2} H^{\cdot} dt$$

where H* is the heat flow and t1 and t2 and the transformation start and end times, respectively. Since the cooling rate is a constant during a DSC experiment, say 1 K/min, Figures 32 and 33 could be graphed as heat flow as a function of time, and the heat of reaction could be determined by calculating the area under the curve for a given transformation. For the thermodynamic data reported in this study, the heats of reactions were determined by using the trapezoidal rule with DSC output. The error of this method was calculated to be $<1\%$ when compared to the data computed by the DSC unit.

It should be noted that the data produced by cooling at rates greater than 20°C/min could not be used for analysis, since an appreciable lag can be expected between the reported and actual sample temperatures at these rates for the DSC system employed. However, the samples produced at these high cooling rates were useful in obtaining microstructural information.

Directional Solidification Sample Preparation & Analysis

Pure Al-Zn alloys containing 92-98wt% in 1wt% Zn increments, as well as alloys containing 94.5wt% and 95.5wt% Zn, were encapsulated into 4mm ID x 6mm OD quartz tubing in the same manner as described above for the DSC samples. In

this case, however, directional solidification directly followed encapsulation without any further sample preparation. To examine the effects of growth rate and liquid temperature gradient on the resulting microstructure of these samples, a zone refining unit was used for unidirectional solidification experiments. This apparatus is schematically illustrated in Figure 34. During an experiment, the heating coil remained at some constant temperature above the sample melting point and moved at a constant rate while the specimen position was fixed. The result was a liquid zone which moved along the length of a sample at a constant rate. After traversing a predetermined distance, samples were quenched in a water bath to preserve the solid/liquid interface for subsequent inspection.

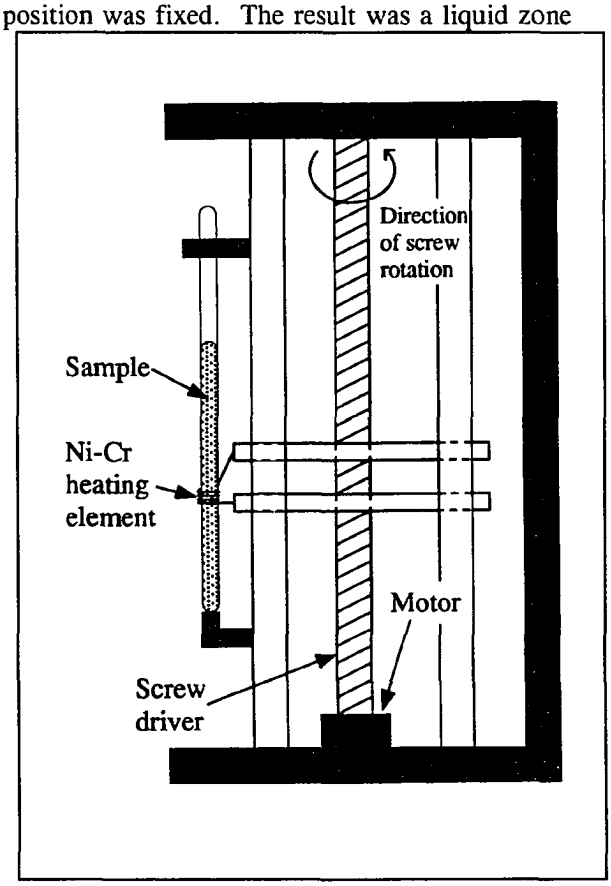

Figure 34. Zone refining apparatus used for directional solidification experiments.

Before samples were tested at a given set of growth conditions (velocity and temperature gradient in the liquid), the system was calibrated with a pure zinc specimen containing an inserted thermocouple within an alumina sheath. By logging the temperature profile at a fixed

location with a strip chart recorder during test conditions, the maximum temperature and the liquid temperature gradient were determined for all sets of testing conditions. In addition, the traverse rate of the zone refiner was calibrated prior to any experimental testing, yielding an exact linear relationship with the unit speed setting, thus giving confidence that the traverse rate remained constant during experimental procedures.

Metallographic Analysis Procedures

For metallographic inspection, samples were mounted in cold-setting epoxide and polished using the following steps: 600-grit silicon carbide paper, 6μm diamond paste, 0.3μm alumina slurry, and colloidal silica. Polishing of the DSC samples was often difficult since these discs were on the order of tens of microns in thickness, and re-polishing after problems such as contaminant scratches and overetching was usually impossible without removing the entire sample. The etchant used to reveal the eutectic microstructure was diluted HCl, with 1-2 parts H_2O per 1 part HCl.

Quantitative microstructural information was obtained with the use of manual and automated image analysis techniques. Manual image analysis consisted of the use of a Donsanto digitizing pad in conjunction with a Nikon Photophot light optical microscope. Automated image analysis refers to the use of a LECO 2001 system in conjunction with a Nikon Photophot light optical microscope and an Olympus stereomicroscope. The typical number of data points taken for various measurements is summarized in Table III. When data is reported throughout this thesis as $x \pm y$, x

and y represent an average value and one standard deviation, respectively. Details on analysis techniques for specific measurements are given as follows:

Table III. Metallographic analysis technique summary.

Measurement	Typical # of data points taken	Data collection method
Area% proeutectic phase	10 fields @ 200x	automated image analysis; point counting method
Interlamellar spacing	10	manual image analysis
Halo width	10-20	manual image analysis
Area% eutectic phases	10 fields @ 200-1000x	automated image analysis

Area% proeutectic phase

The area% of the proeutectic phases for DSC and directionally solidified samples were determined by automated image analysis techniques, wherein approximately 10 image fields at 200x magnification were measured per sample. When samples were stained due to etching procedures, the area% proeutectic phase was manually measured by observing the microstructure with a superimposed 100-point grid and counting the number of proeutectic

intercepts. Approximately 10 image fields at 200x magnification were used in this procedure.

Interlamellar spacing, λ

The eutectic interlamellar spacing was determined by superimposing a line of known length in a direction normal to the lamellar direction, and counting the number of lamellar intercepts. For DSC samples, the minimum apparent spacing, which is considered to be the "true" lamellar spacing as lamellae in this case are oriented normal to the plane of viewing, was measured in various sample regions to yield an average value of λ. For directionally solidified samples, the minimum apparent spacing at 2mm intervals along the growth direction was measured. The average λ values reported for all samples is therefore an average minimum spacing of usually no less than 10 measurements.

Halo width

Zinc halo widths around proeutectic aluminum dendrites were determined by measuring the distance from the dendrite to the outer halo boundary in at least two locations per halo. Typically, no less than 10 halos per sample were measured.

Area% eutectic phases

Based on grey-level differentiation, automated image analysis techniques were used to determine the relative amounts of eutectic phases within the eutectic structure. Approximately 10 fields of view at magnifications of 200-1000x were analyzed per sample for this purpose.

RESULTS & DISCUSSION

Master Alloy Analysis

After melting procedures, all alloy ingots were weighed and some were metallographically inspected in order to determine any changes in i) bulk composition due to zinc evaporation, and ii) compositional variations along a casting length. Weight measurements indicate that losses were typically not greater than 20mg, and at a maximum, corresponded to a compositional change in zinc weight percent of 0.035. The change in ingot composition due to zinc evaporation is therefore considered to be minimal and inconsequential for subsequent use of these alloys.

In order to determine the extent of solute inhomogeneities along a casting length, the area% primary phase was measured at 5mm intervals using quantitative image analysis (QIA) techniques. From these data, theoretical compositions were calculated based on the equilibrium phase diagram so that the solute distribution could be determined. For example, the areas examined in the ingot containing 4.005wt% Al were found to contain a minimum and maximum area% η dendrites of 22.90% and 27.10% respectively, corresponding to 4.08wt% and 3.92wt% Al according to the phase diagram. The maximum compositional variation for this ingot is therefore said to be 4.08-3.92= 0.16wt% Al. The largest such variation for all ingots examined was 0.55wt% Al, and although this value seems large, the data obtained through this analysis are inherently liberal given the systematic errors of QIA techniques. For example, the η lamellae in the eutectic are sometimes included in the measurement of

proeutectic η when the lamellar spacing is large. The proeutectic phase measurement is therefore dependent on the observable eutectic spacing in a given field of view. In light of such errors, the solute variation within a the master alloy ingots is considered to be minimal.

Differential Scanning Calorimetry Results

The sections to follow discuss the undercooling associated with the nucleation of the eutectic by the proeutectic Al-Zn phases, and the effects of the measured undercoolings on eutectic microstructure.

Eutectic Nucleation

The proeutectic and eutectic nucleation temperatures measured by DSC performed at a 1 K/min cooling rate is shown graphically in Figure 35. The liquidus and eutectic lines, as reproduced from the published equilibrium phase diagram (Murray, 1983), are also drawn on this graph. Figure 35 clearly shows that non-reciprocal nucleation behavior is observed for the Al-Zn system. For all samples with Zn concentrations <95wt%, where Al is the proeutectic phase, an average undercooling of 0.25°C below the eutectic temperature of 381.0°C is required for Zn nucleation and subsequent eutectic formation. Conversely at Zn concentrations >95wt%, where proeutectic Zn exists, an average undercooling of 4.0°C is necessary for aluminum nucleation and subsequent eutectic growth. These undercooling values were determined by averaging undercooling temperatures for at least 14 samples for both hypo- and hypereutectic alloys cooled at 1 K/min. Although the undercooling required for the nucleation of Al by Zn is considered to be small in comparison to other systems where one phase is a poor nucleant of the other, the trend shown in Figure 35 is nonetheless reproducible and shows Al to be a better

nucleant of Zn than vice-versa.

The basis for the differences in nucleating abilities for each primary phase is not clear, but it has previously been related to the melting point of the primary phase and interfacial energy measurements. (Sundquist and Mondolfo, 1961) (Southin and Chadwick, 1978) In consideration of Figure 36, it is seen that the solid/liquid interfacial energy of a nucleation catalyst (σ_{CL}) can be considered to be part of the driving force for solidification, while the solid/liquid interfacial energy of the nucleated solid (σ_{SL}) can be considered to be a barrier for nucleation. In other words, an increase in σ_{CL} would tend to decrease the wetting angle, θ, of the nucleated embryo, while an increase in σ_{SL} would tend to increase θ. It follows that metals which have high solid/liquid interfacial energies (and high θ's) are difficult to nucleate and will tend to be good nucleating agents, and metals with low solid/liquid interfacial energies (low θ's) will be easy to nucleate and will act as poor nucleating agents. Furthermore, since elements having high melting temperatures typically have higher σ_{SL} 's than elements with lower melting temperatures and equal crystal structures, those elements with higher melting points should be better nucleants than those with lower melting temperatures (Sundquist and Mondolfo, 1961) (Southin and Chadwick, 1978).

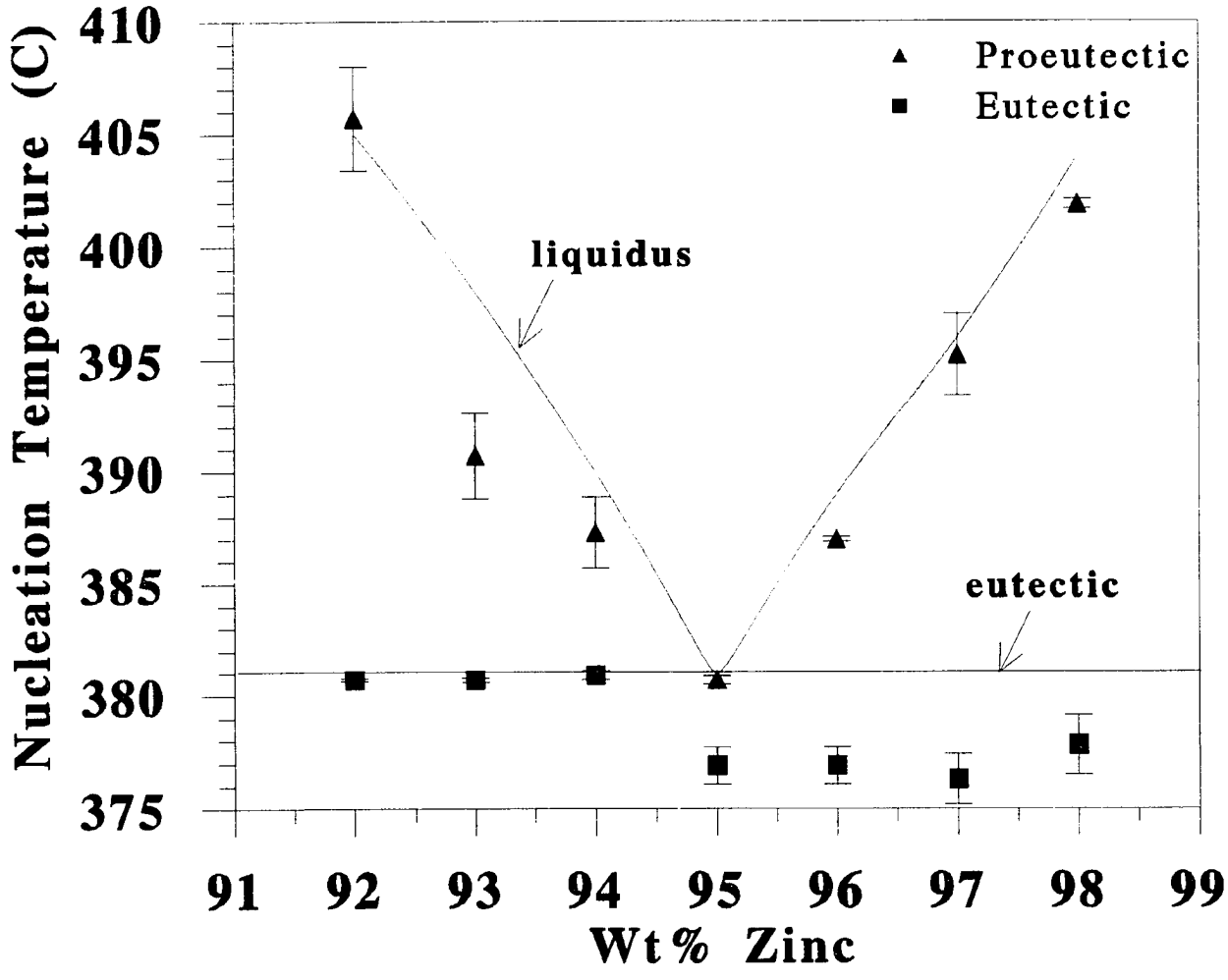

Figure 35. Nucleation temperatures for Al-Zn alloys. The square symbols represent the temperatures at which the proeutectic phase nucleates the other eutectic phase. (Solid lines taken from the equilibrium phase diagram).

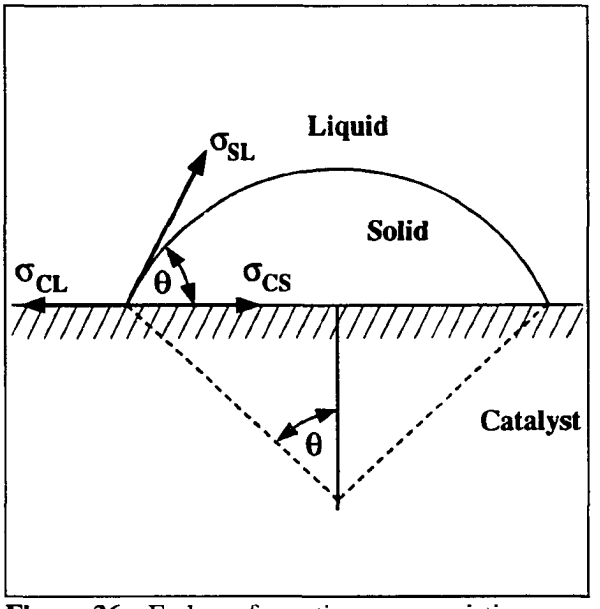

Figure 36. Embryo formation on an existing substrate and associated interfacial energies.

For the Al-Zn system, the nucleating abilities of the primary phases cannot be directly related to melting points since these elements are of different crystal structures. However, the relationship between interfacial energy and nucleating ability does not hold true. σ_{SL} can be calculated (Smithells, 1983) (Liu and Jones, 1992) (Kurz and Fisher, 1989) to be 0.101 and 0.127 J/m^2 for Al and Zn, respectively. In this case, the element with the lower interfacial energy (Al) is the better nucleant as shown in Figure 35. As discussed by Southin and Chadwick (1978), crystal structure is an important factor in heterogeneous nucleation, but its exact influence is not known with certainty and is perhaps the influencial factor in the atypical nucleation of Al-Zn alloys.

In the sections to follow, the effects of the non-reciprocal nucleation characteristics on off-eutectic Al-Zn microstructure are discussed in terms of Zn halos and eutectic structure.

Zn halos

For hypoeutectic Al-Zn alloys (>5wt% Al), Zn halos are typically found surrounding Al primary dendrites (Figure 37). The origin and significance of halos in eutectic systems has been examined by many researchers (Spittle, 1977) (Porot et al., 1987) (Kofler, 1950) (Sundquist et al., 1962) (Salli et al., 1975) (Barclay et al., 1973) (Suk et al., 1992) (Yilmaz and Elliott, 1984). Sundquist et al. (1962), and later Salli et al. (1975), explained the formation of halos on the basis of the undercoolings required for the nucleation of primary and eutectic phases. Given an alloy of composition C1 as shown in Figure 38, proeutectic β will nucleate from the liquid at some temperature at or below the liquidus, T1, and continue to grow as the temperature is decreased. If β is a poor

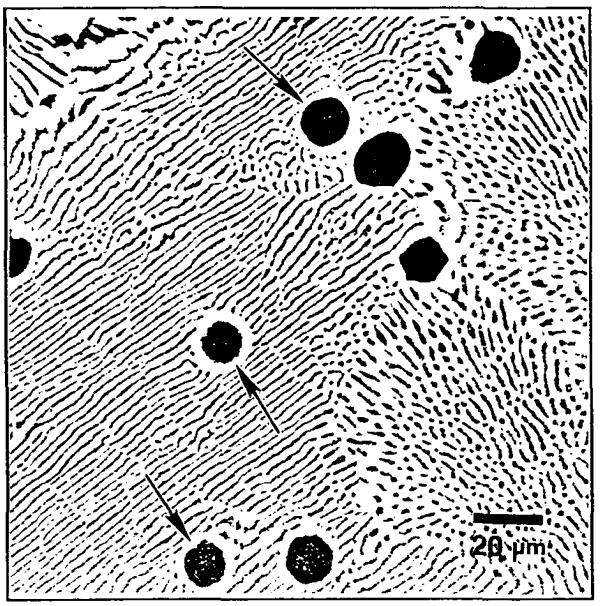

Figure 37. Typical hypoeutectic Al-Zn microstructure. Zn halos around proeutectic Al are indicated.

nucleant of α, the liquid composition will follow the metastable liquidus line to a temperature T2, which can be significantly below the eutectic temperature T_e. Upon the nucleation of α at T2 and C2, the remaining liquid is supersaturated in element A, and therefore a halo of α will form about the primary β phase in order to bring the system back to the eutectic composition, C_e, so that the eutectic can grow. According to this theory (Sundquist et al, 1962) (Salli et al., 1975), the size of the halo should be proportional to the undercooling required for second phase nucleation, and halos should exist only when the primary phase is not a good nucleant of the second phase.

In contrast to the findings of Sundquist et al. (1962) and Salli et al. (1975), Kofler (1950) found that halos are formed due to coupled zone arguments rather than undercooling considerations. In a binary system, the coupled zone defines the alloy compositions and interface undercoolings at which the growth rate of eutectic exceeds that of either single phase. When outside of the coupled zone, dendritic growth of one phase will proceed ahead of the eutectic growth front, and the microstructure will therefore consist of both dendrites and eutectic. Thus, as shown in Figure 39 for an alloy of composition C1, if a primary phase β nucleates the second phase α at T2 and C2, a halo of α will develop since the system is outside of the coupled zone. Conversely, for an alloy of composition C3, a halo of β cannot develop around primary α since, regardless of the undercooling required for nucleation of the second phase, the system will be within the coupled zone. Other studies involving unidirectional solidification experiments (Gigliotti et al., 1970) (Barclay et al., 1973) (Suk et al., 1992) (Yilmaz and Elliott, 1984) agreed with Kofler in that halo

formation is explained in terms of the growth rates of phases at certain temperatures and compositions. The coupled zone of growth for eutectic systems therefore seems to be of critical importance in predicting which systems will have halos of one or both phases.

Because Zn halos were found for DSC samples which do not undergo unidirectional solidification, the theories for halo development based on competitive growth arguments cannot be directly applied to explain the formation of Zn halos around Al proeutectic phase. Furthermore, since the coupled zone of growth must contain the eutectic point itself, it seems unlikely that the slight undercooling of 0.25°C required for the nucleation of the Zn halo by Al would be sufficient to have the system pass through the coupled zone region even if the zone was skewed to the Al-rich side of the eutectic. The results of this study are also in disagreement with the theories for halo formation which are based on solute enrichment in the liquid (Sundquist et al., 1962) (Salli et al, 1975). The 0.25°C extension of the Al liquidus line below the eutectic point represents a very small undercooling for the nucleation of Zn by Al, and halo formation is therefore not necessary to bring the liquid composition back to eutectic. In addition, halo widths were found to be inversely related to cooling rate (Figure 40), but not with any specific functional relationship. This is contrary to the predictions of Sundquist et al. (1962) and Salli et al. (1975), since according to these theories, a higher undercooling below the eutectic, which can be expected by a faster cooling rate, should result in more solute enrichment in the liquid, and hence, a larger halo. Rather, it seems that the size of the halo is limited

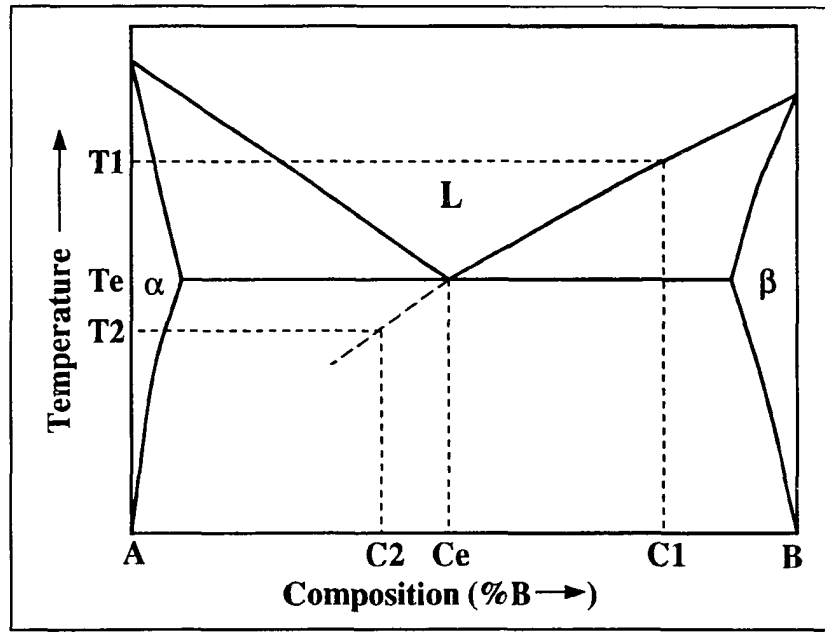

Figure 38. Hypothetical phase diagram showing β as a poor nucleant of α.

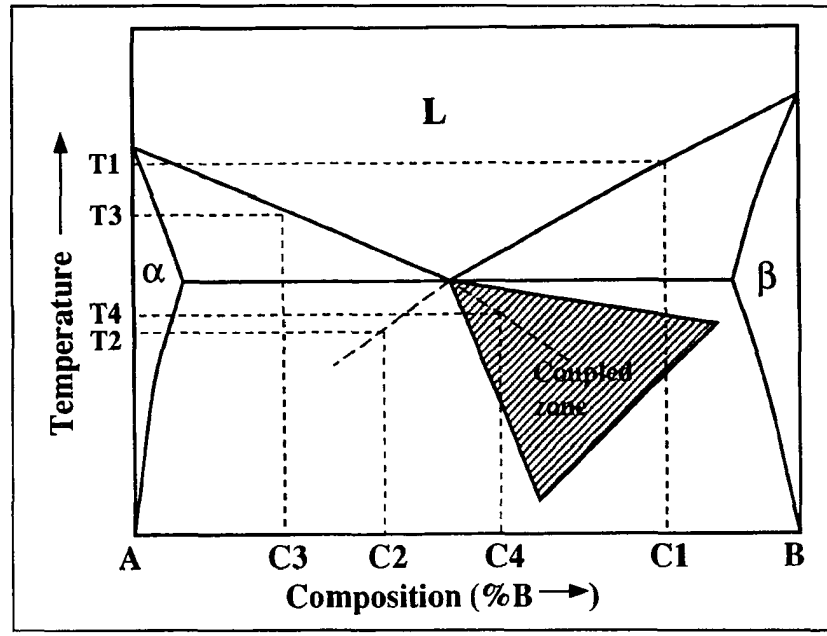

Figure 39. Hypothetical phase diagram showing zone of coupled growth, wherein halos of β around proeutectic α cannot develop.

by the growth rate of Zn and the time necessary to reach the temperature at which Zn will nucleate Al.

Based on the observations mentioned above, it is proposed that nucleation phenomena, rather than growth considerations, control halo formation. The halo is thought to result from the fact that Zn is a poorer nucleant of Al than vice versa, as shown in Figure 35. Just as the proeutectic Zn phase requires an undercooling below the eutectic temperature to nucleate Al, the Zn halo will also grow to some undercooling before Al nucleation and steady-state growth can occur. This is evidenced by the differences in the DSC eutectic peaks for Al-rich (<95wt% Zn) and Zn-rich (>95wt% Zn) alloys, shown in Figures 41 and 42 respectively. As shown in these graphs, the eutectic peak for a typical hypoeutectic alloy is wider than that for a typical hypereutectic alloy because there are two nucleation events within the hypoeutectic peak: i) the nucleation of the Zn halo by the Al proeutectic phase, and ii) the nucleation of Al lamellae on the Zn halo. While the average eutectic peak width for hypoeutectic alloys cooled at 1 K/min was 1.5°C (standard deviation = 0.2°C), the width for hypereutectic alloys were negative in value due to the temperature increase resulting from the eutectic heat of fusion (see Figure 42). Although these two separate events are not discernable from the "eutectic peak" in Figure 41, it can be generally stated that the nucleation of the Zn halo occurs at the onset temperature, and "true" eutectic nucleation (after which cooperative eutectic growth can ensue) occurs at some temperature less than 1.5°C below said onset temperature.

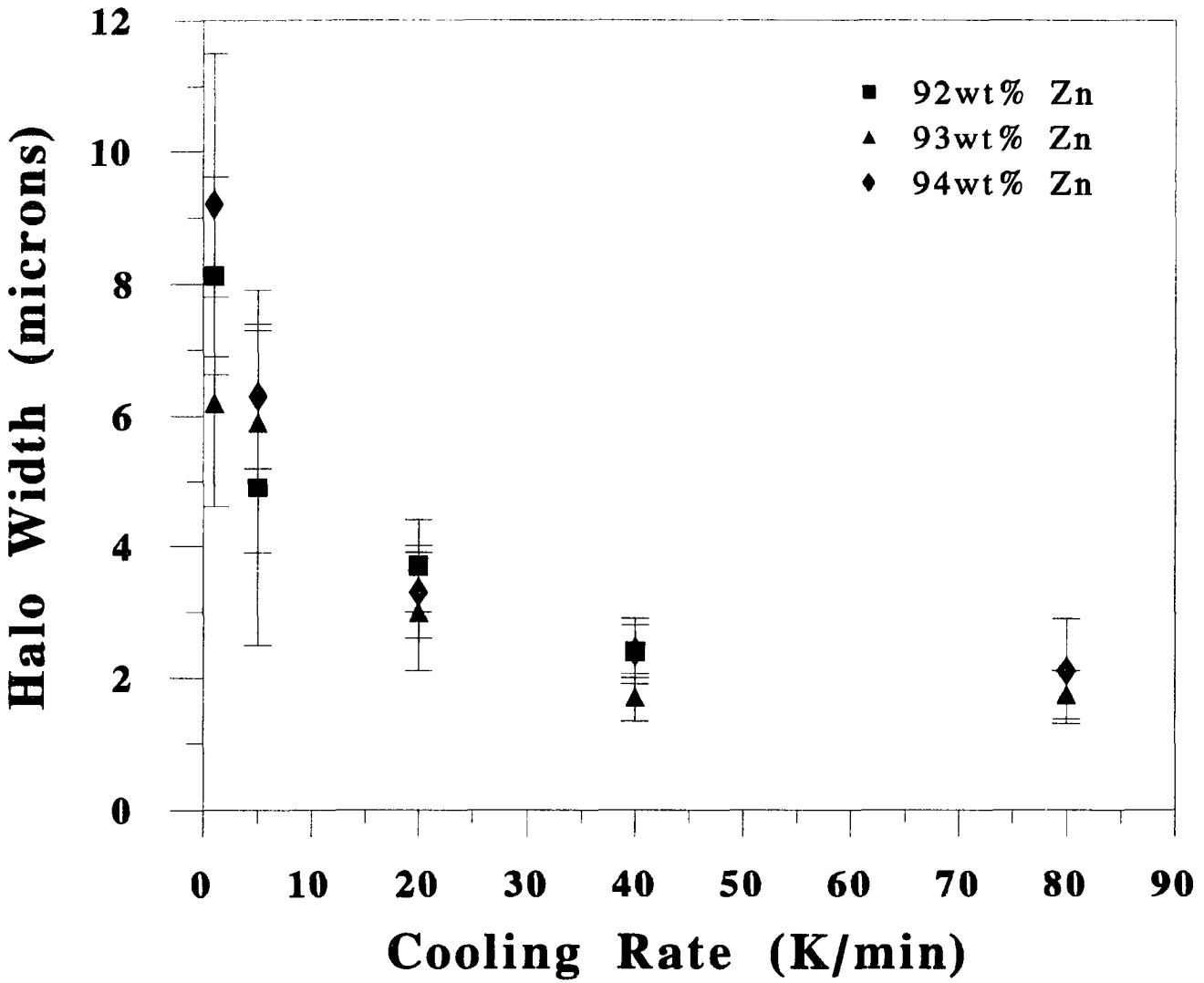

Figure 40. Halo width as a function of cooling rate.

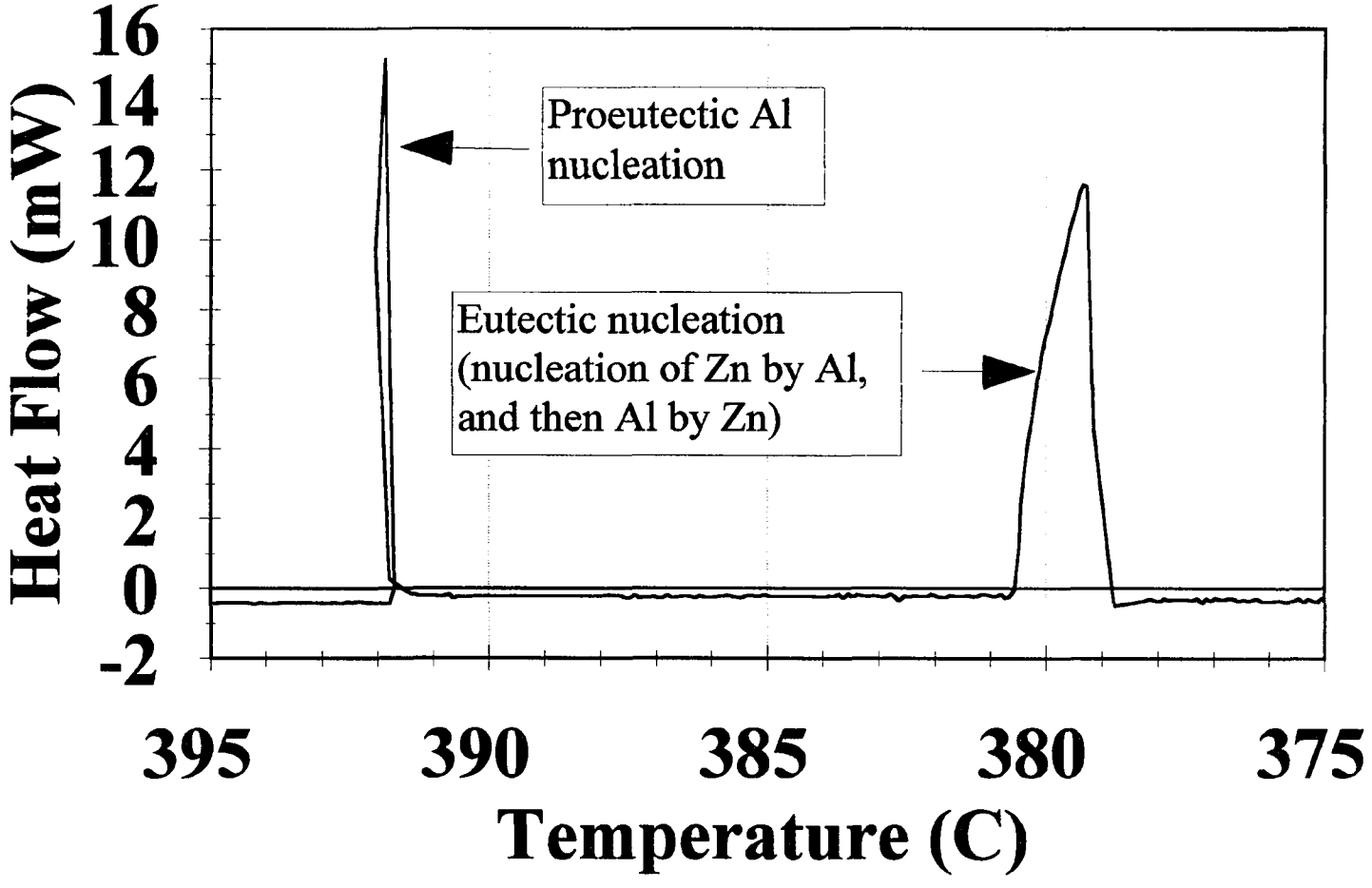

Figure 41. DSC trace for the solidification of a hypoeutectic Al-Zn alloy cooled at 1 K/min.

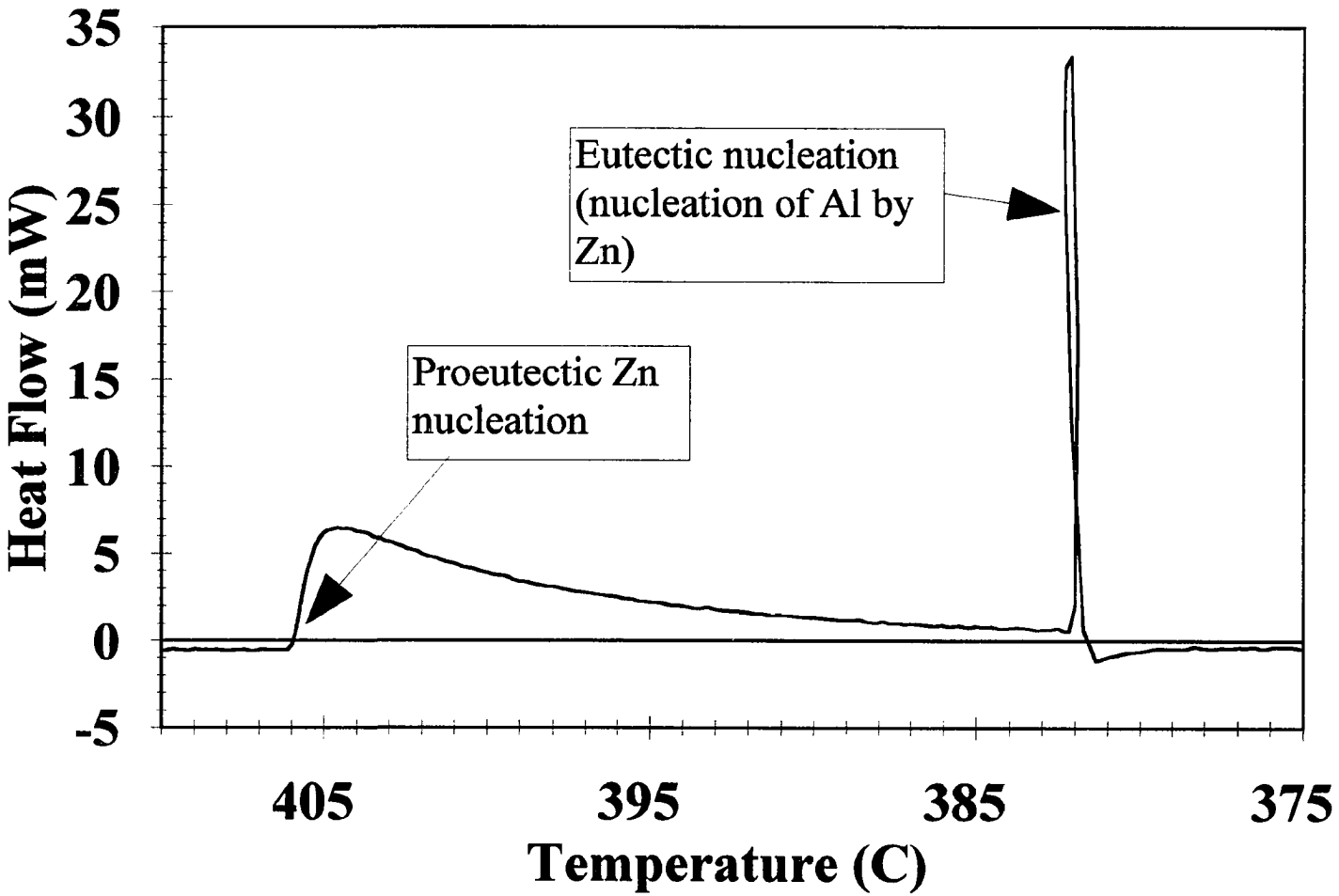

Figure 42. DSC trace for the solidification of a hypereutectic Al-Zn alloy cooled at 1 K/min.

Interlamellar Spacing

As originally put forth by Jackson and Hunt (1966), the total undercooling during metallic eutectic growth can be expressed as follows:

$$\Delta T = \Delta T_c + \Delta T_r \,, \tag{8}$$

where ΔT_c and ΔT_r are the undercoolings due to solute diffusion and interface curvature considerations, respectively. From equation (1), and equation which relates interlamellar spacing (λ) and growth rate (V) can be derived as

$$\lambda^2 V = \frac{K_r}{K_c} \,, \tag{13}$$

where K_c and K_r are solute and curvature constants, respectively. Assuming growth to occur under extrenum conditions, where the undercooling is a minimum for a given growth rate,

$$\frac{d(\Delta T)}{d\lambda} = 0 \,, \tag{11}$$

and therefore,

$$\Delta T = K_c \lambda V + \frac{K_r}{\lambda} \,. \tag{10}$$

Solving for V and substituting into equation (2) yields

$$\Delta T \lambda = 2K_r \,; \quad \lambda = \frac{2K_r}{\Delta T} \,. \tag{36}$$

K_r is defined as

$$K_r = \frac{2(1-f)|m_\beta|\Gamma_\alpha \sin(\theta_\alpha) + 2f|m_\alpha|\Gamma_\alpha \sin(\theta_\alpha)}{f(1-f)(|m_\alpha| + |m_\beta|)}, \quad (37)$$

where f is the volume fraction of second phase in the eutectic, m is the liquidus slope, Γ is the Gibbs-Thomson coefficient, and θ is the lamellar angle for phases α and β. The values used for these variables were either experimentally determined or taken from the literature, and are listed in Table IV. By solving for K_r, equation (10) can be used to predict λ as a function of ΔT. As shown in Figure 43, the interlamellar spacing for the Al-Zn eutectic is very sensitive to small changes in undercooling ("theory" curve), and the measured λ values for alloys cooled at 1 K/min are in good agreement with theory. The differences in eutectic nucleation temperatures as shown in Figure 35 therefore results in a significant difference in the eutectic structure for hypo- (<95wt% Zn) and hypereutectic (>95wt% Zn) alloys. Because the undercooling required for second phase nucleation is greater for hypereutectic alloys, the eutectic structure is notably finer. The agreement between experiment and theory as shown in Figure 43 provides microstructural confirmation for the measured undercooling values. It should be mentioned here that, as previously discussed, the exact eutectic nucleation temperature for Al-rich alloys is not known with absolute certainty because the DSC eutectic peak for these alloys also contains zinc halo nucleation and growth (Figure 41). However, because the mass of liquid which transforms to eutectic far exceeds the mass of liquid which transforms into zinc halos, it seems likely that the eutectic transformation results in the peak heat flow of the eutectic DSC peak. The eutectic temperature for hypoeutectic Al-Zn alloys can

therefore be said to be some temperature greater than the temperature associated with the peak heat flow, which is typically about 1°C less than the eutectic peak onset temperature. In light of this discussion, the correlation between measured λ and theory shown in Figure 43 remains valid.

Table IV. Values used to calculate K_r.

Parameter	Value
f	0.28
m_{Al}	-8.0 K/wt%
m_{Zn}	10.16 K/wt%
Γ_{Al}	9.0 E -8 mK
Γ_{Zn}	1.1 E -7 mK
θ	80°

As shown in Figure 44, the difference in interlamellar spacing when comparing hypo- and hypereutectic alloys decreases with an increased cooling rate. Some data points are missing in this graph since, for alloys containing 92 and 93wt% Zn, only a rod eutectic structure formed at higher cooling rates. Because for hypereutectic alloys eutectic nucleation occurs at an undercooling of at least 3°C for all cooling rates, large differences in undercooling at undercoolings in excess of 3°C will result in only small changes in λ as shown in Figure 43. The interlamellar spacing values for alloys containing ≥95wt% Zn therefore change minimally for cooling rates ≥5 K/min. For hypoeutectic alloys, however, eutectic nucleation occurs at very small undercoolings at low cooling rates, and consequently, any small increases in undercooling due to an increased cooling rate results in a large decrease

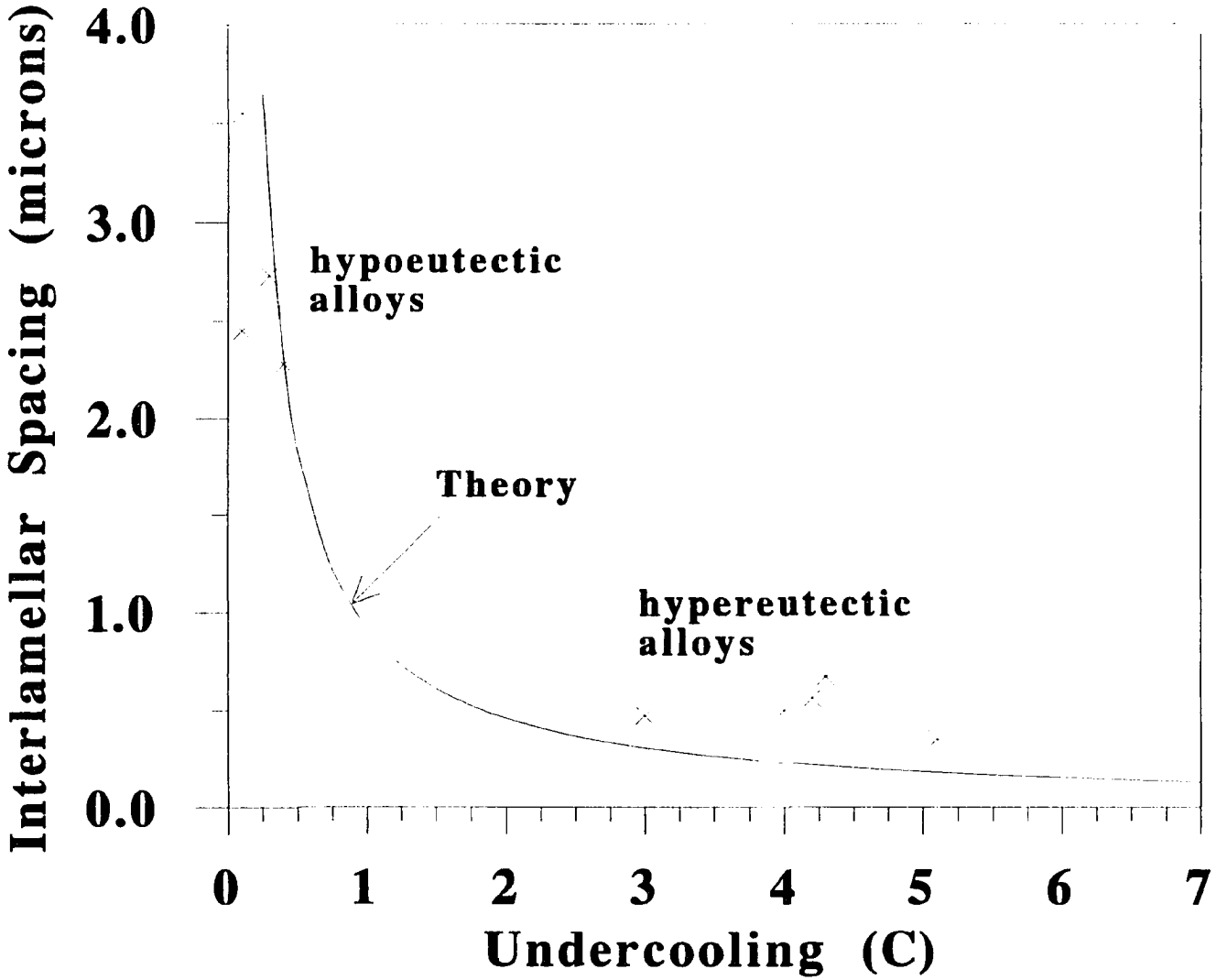

Figure 43. Interlamellar spacing as a function of undercooling for the Al-Zn eutectic. (X= measured values for samples cooled at 1 K/min)

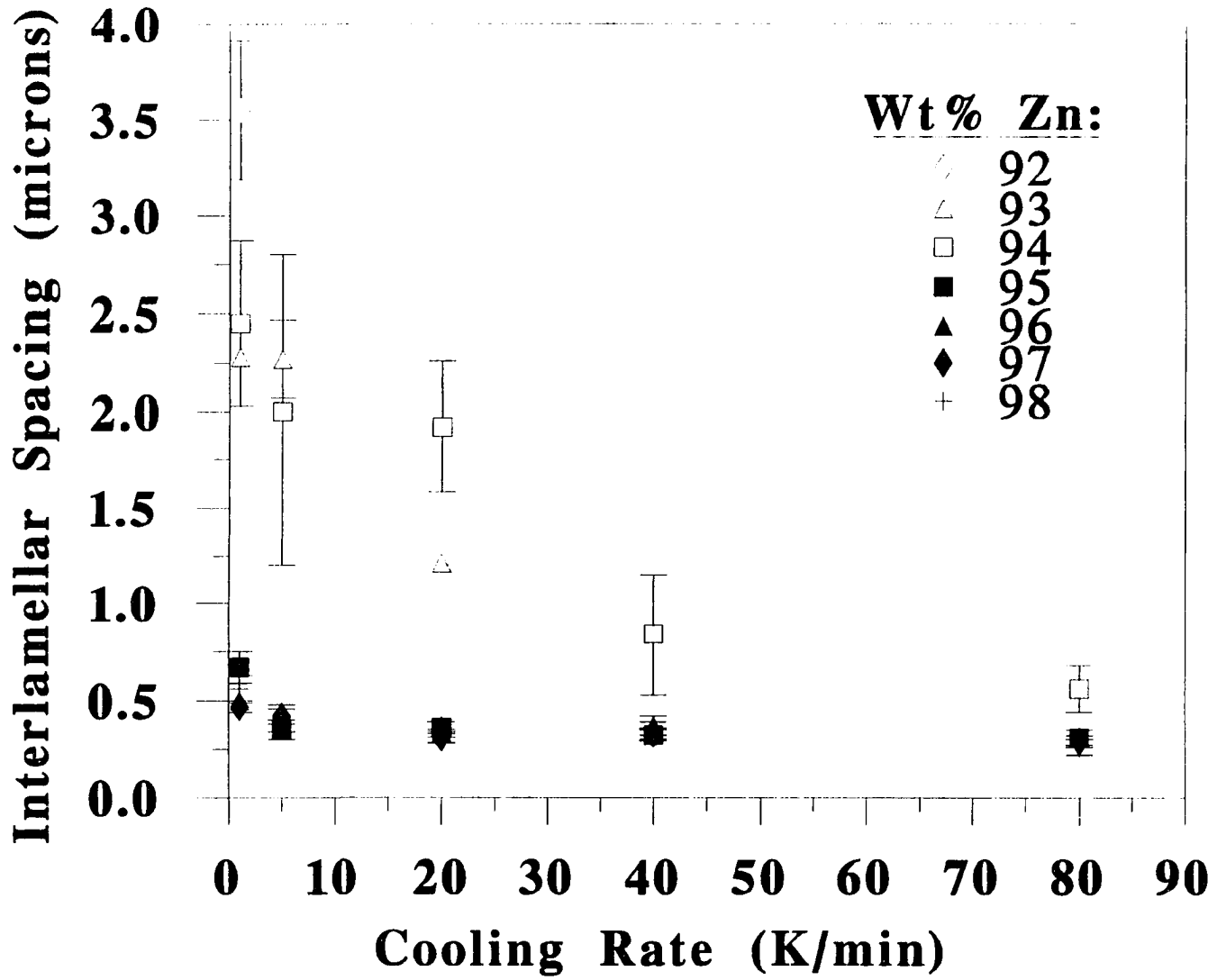

Figure 44. Measured λ values for Al-Zn alloys, as a function of cooling rate. Open symbols represent hypoeutectic alloys (<95wt% Zn).

in λ due to the large negative slopein the λ-ΔT curve (Figure 43) at low ΔT values. In quantitative terms, the difference in λ for hypo- and hypereutectic alloys can be up to 3μm (a 7-fold difference) when the cooling rate is 1 K/min, while it is only 0.3μm (a 2-fold difference) at a cooling rate of 80 K/min.

Volume Fraction of Second Phase in Eutectic and Eutectic Morphology

Because of the depressed eutectic temperature for alloys containing $\geq$95wt% Zn, the volume fraction of each phase in the eutectic structure is consequently altered. A 4°C extension of the Zn liquidus below the 381°C eutectic temperature results in a shift in the eutectic composition from 95wt% to approximately 94wt% Zn. By using the lever rule, one can expect the volume fraction of the Al phase in the eutectic to therefore increase from 0.28 to 0.35. On the other hand, no significant change in the volume fraction of the Al phase is expected for hypoeutectic alloys, since an undercooling of only 0.25°C was required for eutectic nucleation. In good agreement with predicted values, the measured area fraction of the Al phase in the eutectic as determined via automated image analysis was found to be an average of 0.26 (standard deviation = 0.03) and 0.40 (standard deviation = 0.05) for hypo- and hypereutectic alloys, respectively. Like the measured λ values, the area fraction data provide microstructural confirmation of the measured ΔT values.

The difference in the volume fraction of the minor (Al) phase in the eutectic results in a difference in eutectic morphology. Typical microstructures for all alloys cooled at 1 K/min are shown in Figure 45a-g. Although the eutectic structure for

alloys containing ≥95wt% Zn is strictly lamellar, the structure for hypoeutectic alloys consists of rods, or rods and lamellae. Following the discussion of Cooksey et al. (1964) on eutectic morphology, this difference can be explained through interfacial energy arguments. The length of the interface surface per unit cross section in a lamellar morphology is independent of the relative thicknesses of the lamellae and is directly proportional to $2/\lambda$. For a rod structure, however, the interphase surface area is dependent on the relative volume fractions of the two eutectic phases. Based on Figure 46, the number of cross-sectional "triangles" resulting from rod formation is $4/\sqrt{3}\lambda^2$, with each triangle containing an interfacial length of πr. The interfacial length is therefore $4\pi r/\sqrt{3}\lambda^2$, and substituting for r, it is calculated to be $3.816F^{1/2}/\lambda$, where F is the volume fraction of the minor phase. The surface energy associated with rod and lamellar growth is therefore as shown in Figure 47 is expected at low F values (<0.28), whereas for higher F values, a lamellar morphology is predicted. This analysis provides rationale for the lamellar structure found in hypereutectic alloys (>95wt% Zn, for which F=0.40) and the rod structure observed for hypoeutectic alloys (<95wt% Zn, for which F=0.26). The volume fraction measurement for hypoeutectic alloys was so close to the transition point that the presence of a mixed rod/lamellar structure was not surprising.

Figure 45a.

100μm

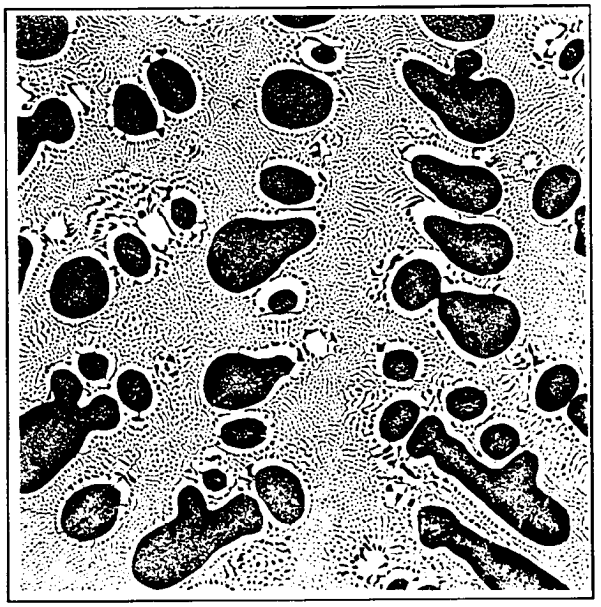

Figure 45b.

100μm

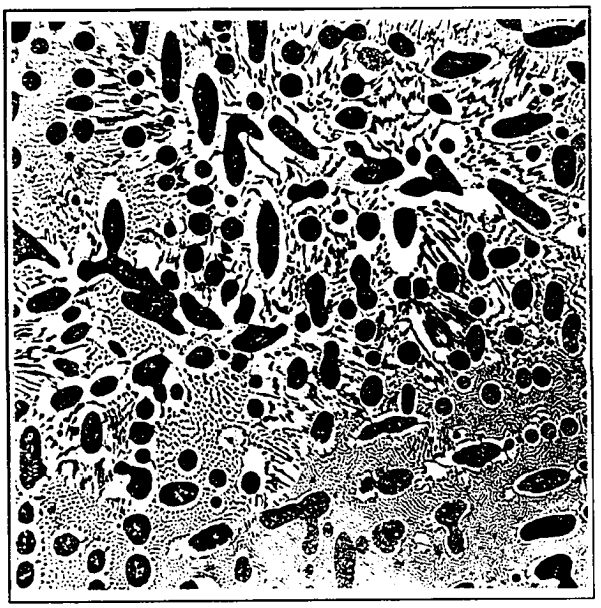

Figure 45. Typical microstructures for Al-Zn alloys cooled at 1 K/min: (a-g correspond to 92-98wt% Zn, respectively).

Figure 45c.

100μm

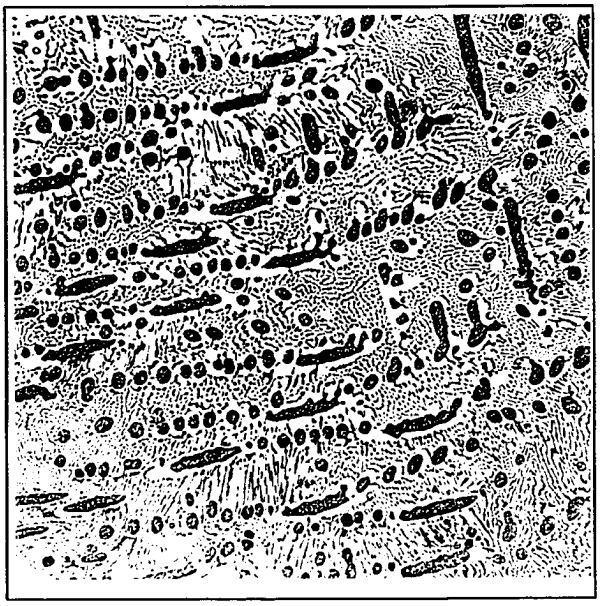

Figure 45d.

100μm

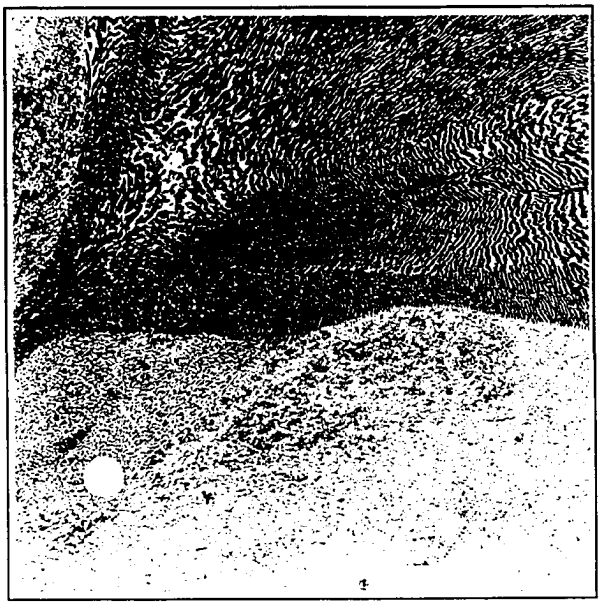

Figure 45. Typical microstructures for Al-Zn alloys cooled at 1 K/min: (a-g correspond to 92-98wt% Zn, respectively).

Figure 45e.

100μm

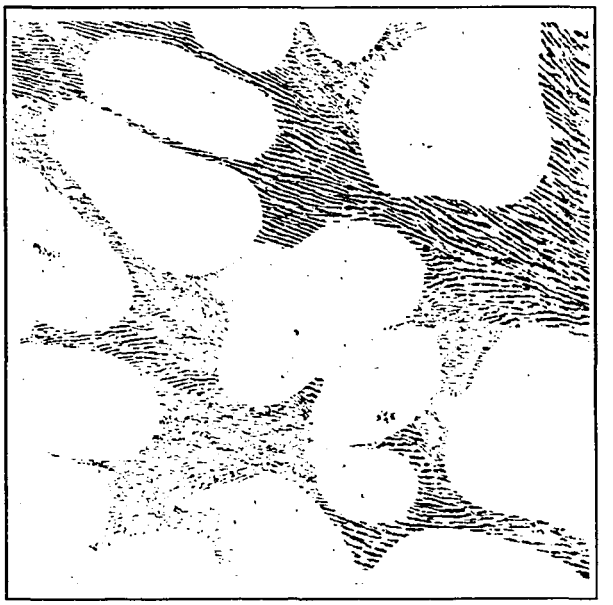

Figure 45f.

100μm

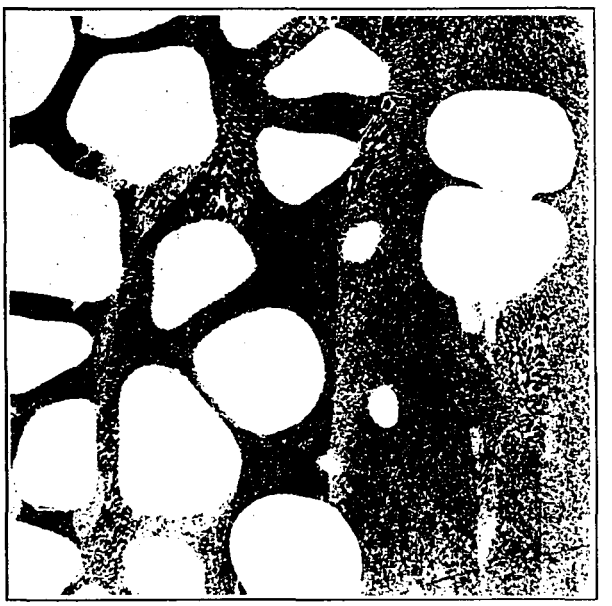

Figure 45. Typical microstructures for Al-Zn alloys cooled at 1 K/min: (a-g correspond to 92-98wt% Zn, respectively).

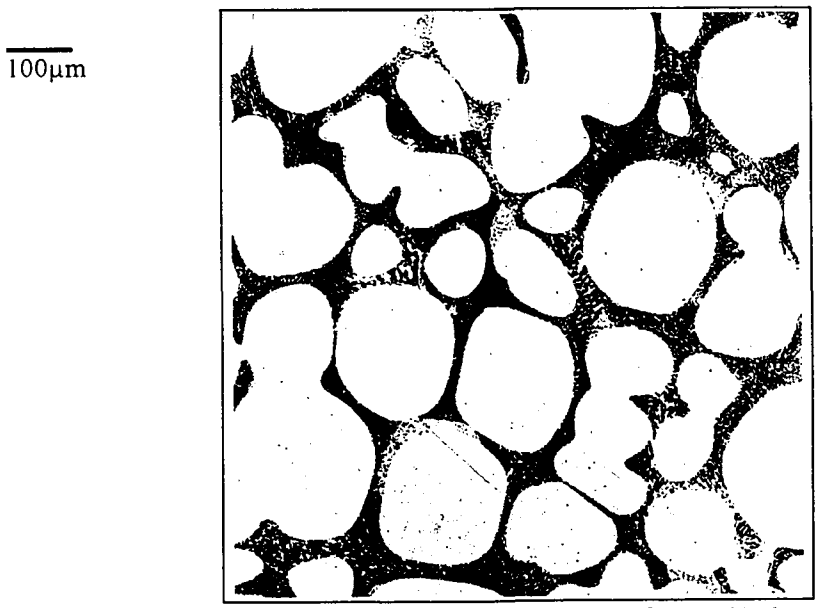

Figure 45g. Typical microstructure for 2wt%Al-98wt%Zn alloy cooled at 1 K/min.

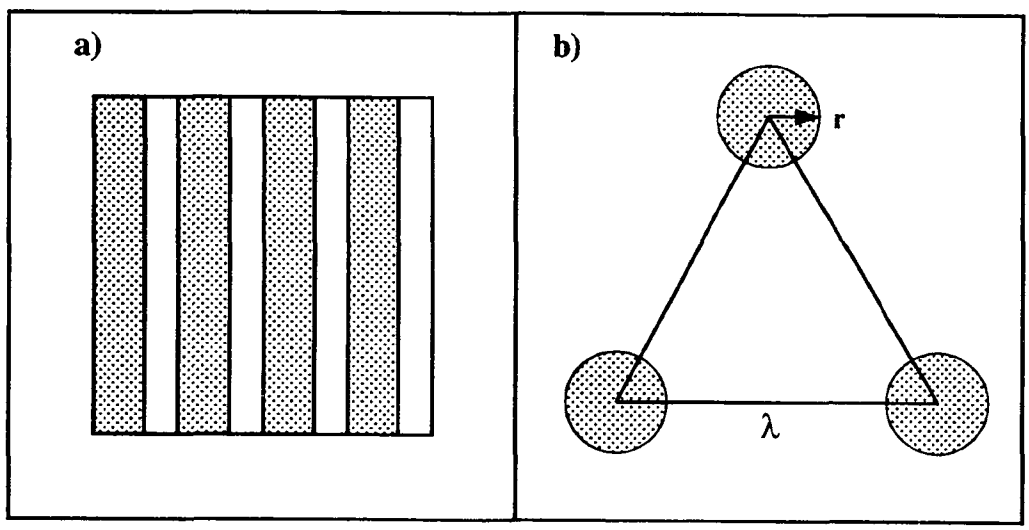

Figure 46. Cross-sections of a) rod, and b) lamellar eutectic morphologies.

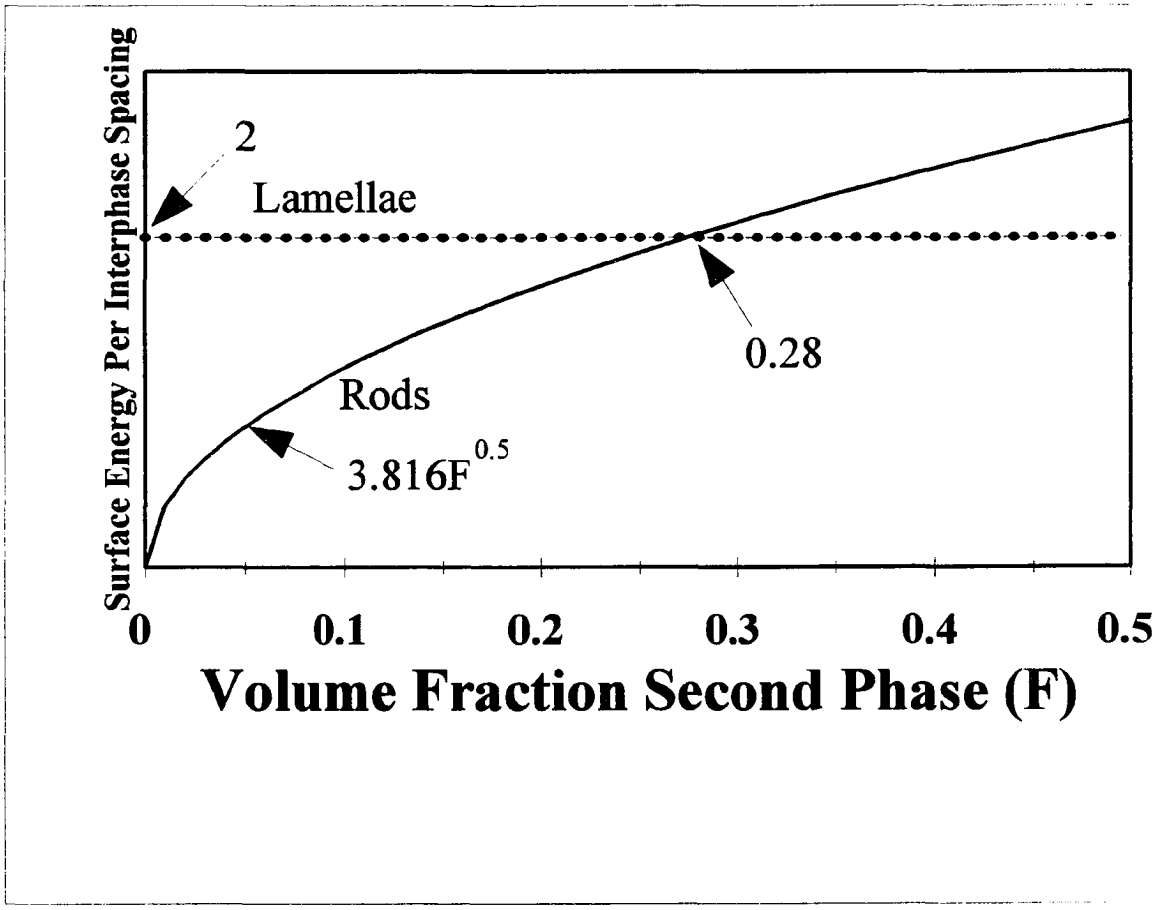

Figure 47. Surface energy produced by rod and lamellar eutectic growth, as a function of volume percent second phase (after Cooksey et al., 1964).

Unidirectional Eutectic Growth

The sections to follow discuss the microstructures developed during the unidirectional solidification of Al-Zn eutectic and off-eutectic alloys.

Interlamellar Spacing

The interlamellar spacing (λ) data collected for all directionally solidified samples can be seen in Figure 48, which is a plot of λ as a function of growth rate. As expected, the data show a significant drop in λ as the growth rate is increased over the order of magnitude as shown in the graph. Consistent with the eutectic growth theories of Tiller (1958) and Jackson and Hunt (1966), λ is shown to be linearly proportional to the inverse square root of growth rate in Figure 49. Figure 49 includes a best fit linear curve determined by regression analysis, which in this case, yields an error rate (r^2) of 0.94 (this number signifies the relative accuracy of the curve formula, where a value of 1.0 indicates complete or near-complete accuracy; the closer this number to 1.0, the more accurate the curve fit).

As Figure 50 shows, the λ data collected in this study is consistent with data reported by other researchers (Chadwick, 1963b) (Cooksey et a., 1964) (Moore and Elliottm 1969) (Livingston et al., 1970) (Tuček et al., 1986), who have collectively measured the λ for Al-Zn eutectic alloys for growth rates from about 0.2-2000 microns/second. At least one of these other studies (Cooksey et al., 1964) contend that the λ for the Al-Zn eutectic is proportional to inverse cube root, rather than the

inverse square root, of growth rate. Indeed, when all of the data from all of the work on the Al-Zn eutectic is considered, the data is found to best fit a $\lambda \propto V^{-1/3}$ relationship ($r^2=0.85$) more accurately than a $\lambda \propto V^{-1/2}$ relationship ($r^2=0.77$). However, there are two points to consider when making this judgement: First, the data collected for the lowest growth rates will be the least accurate due to the difficulties in measuring such velocities and the fact that samples solidified at the lowest growth rates will be the ones most affected by small changes in growth rate. If the λ data is reconsidered without the slowest growth rate values, which consist of four (4) points taken at $V <$ 1.25 microns/second by Cooksey et al. (1964), λ is found to be more accurately related to the inverse square root of growth rate. This can be seen by comparing Figures 51 and 52, which show λ as a function of $V^{-1/2}$ ($r^2=0.93$) and $V^{-1/3}$ ($r^2=0.89$), respectively. The second point is that fitting the λ data to $V^{-1/3}$ results in a significantly negative y-intercept, or a negative λ value as $V \rightarrow \infty$ (Figure 52). Theoretically this is not possible, and one must therefore question the physical significance of relating λ to $V^{-1/3}$ for all growth rates. In consideration of these two factors, the Al-Zn eutectic is considered to conform to $\lambda \propto V^{-1/2}$.

Comparison of DSC and DS Results: λ

In contrast to the DSC work where λ was found to be largely dependent on alloy composition, λ was determined to only depend on growth rate for unidirectionally solidified alloys. As can be seen in Figure 53, for which the average standard deviation for all data points shown is 0.10, λ is independent of alloy

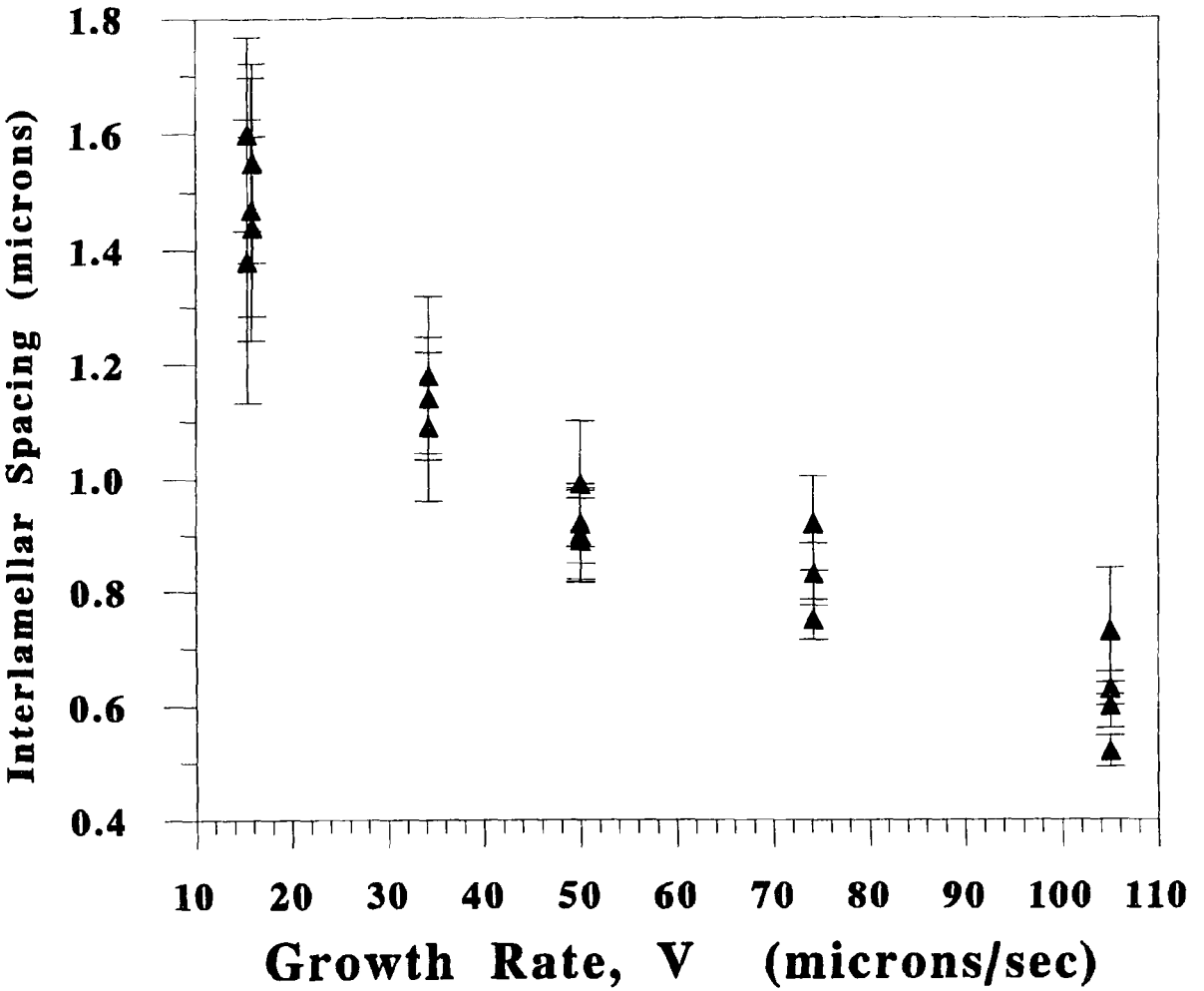

Figure 48. Interlamellar spacing as a function of growth rate during directional solidification for all samples used in this study.

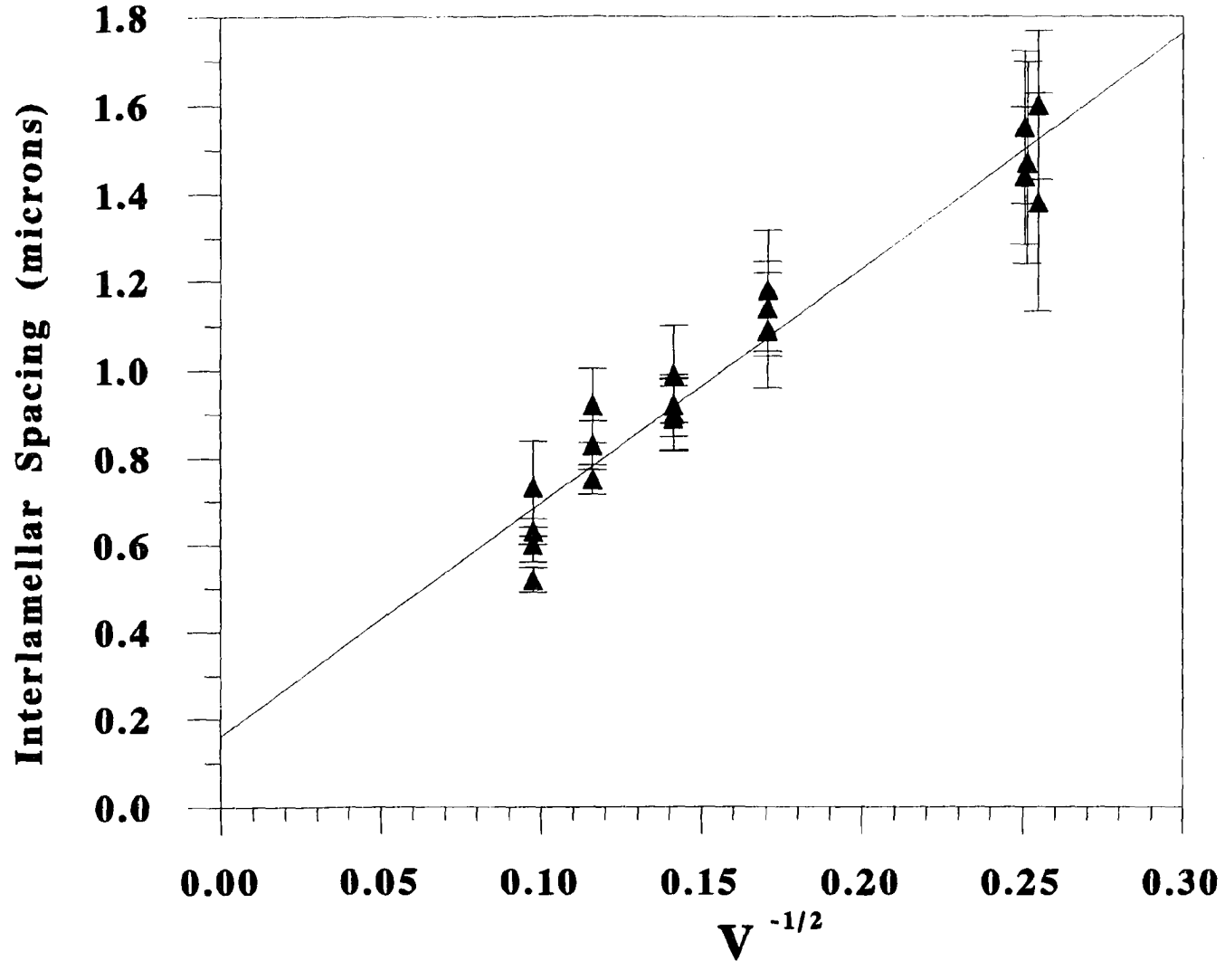

Figure 49. Correlation between interlamellar spacing and $V^{-1/2}$ for all directionally solidified samples used in this study.

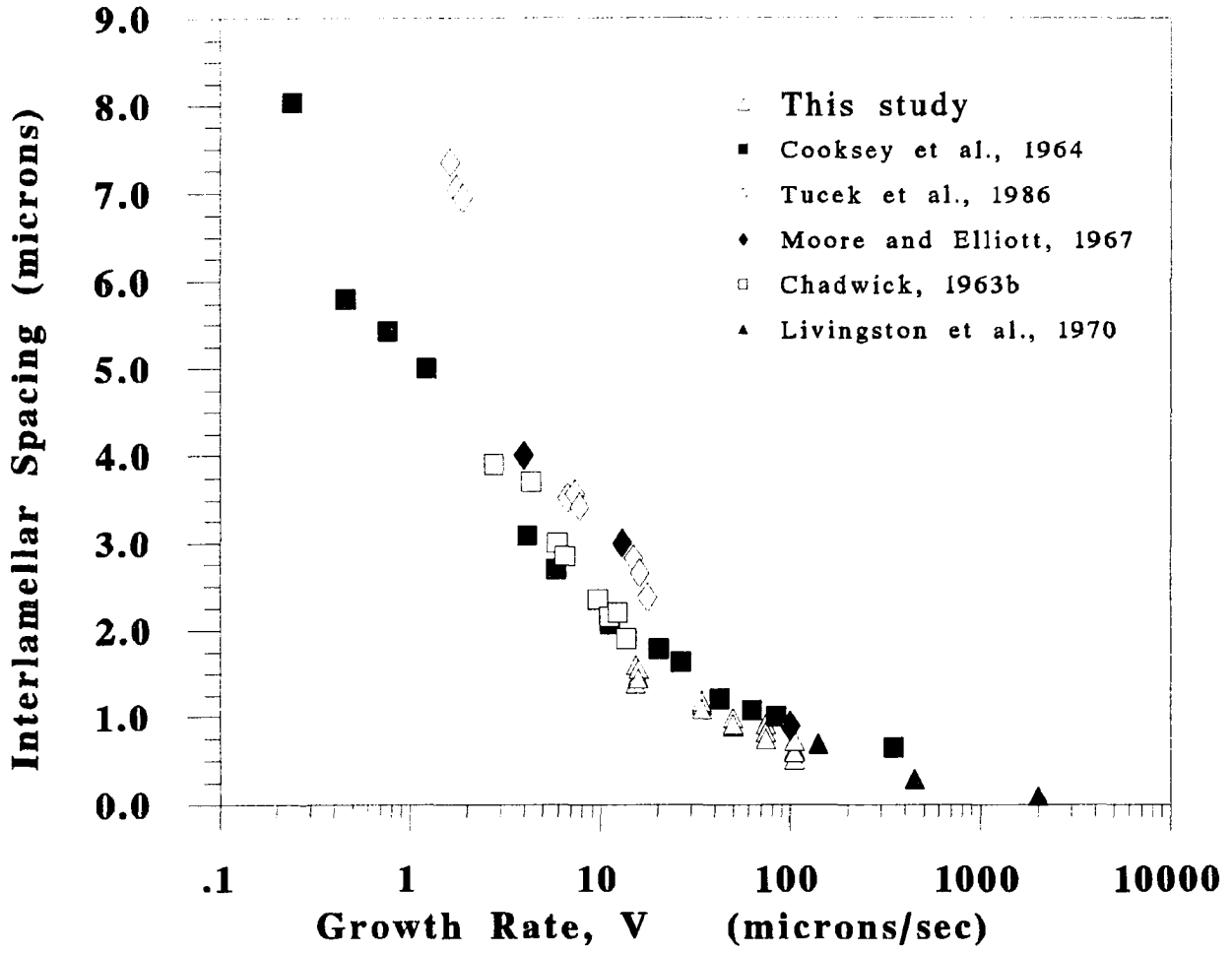

Figure 50. Interlamellar spacing as a function of growth rate for the Al-Zn eutectic.

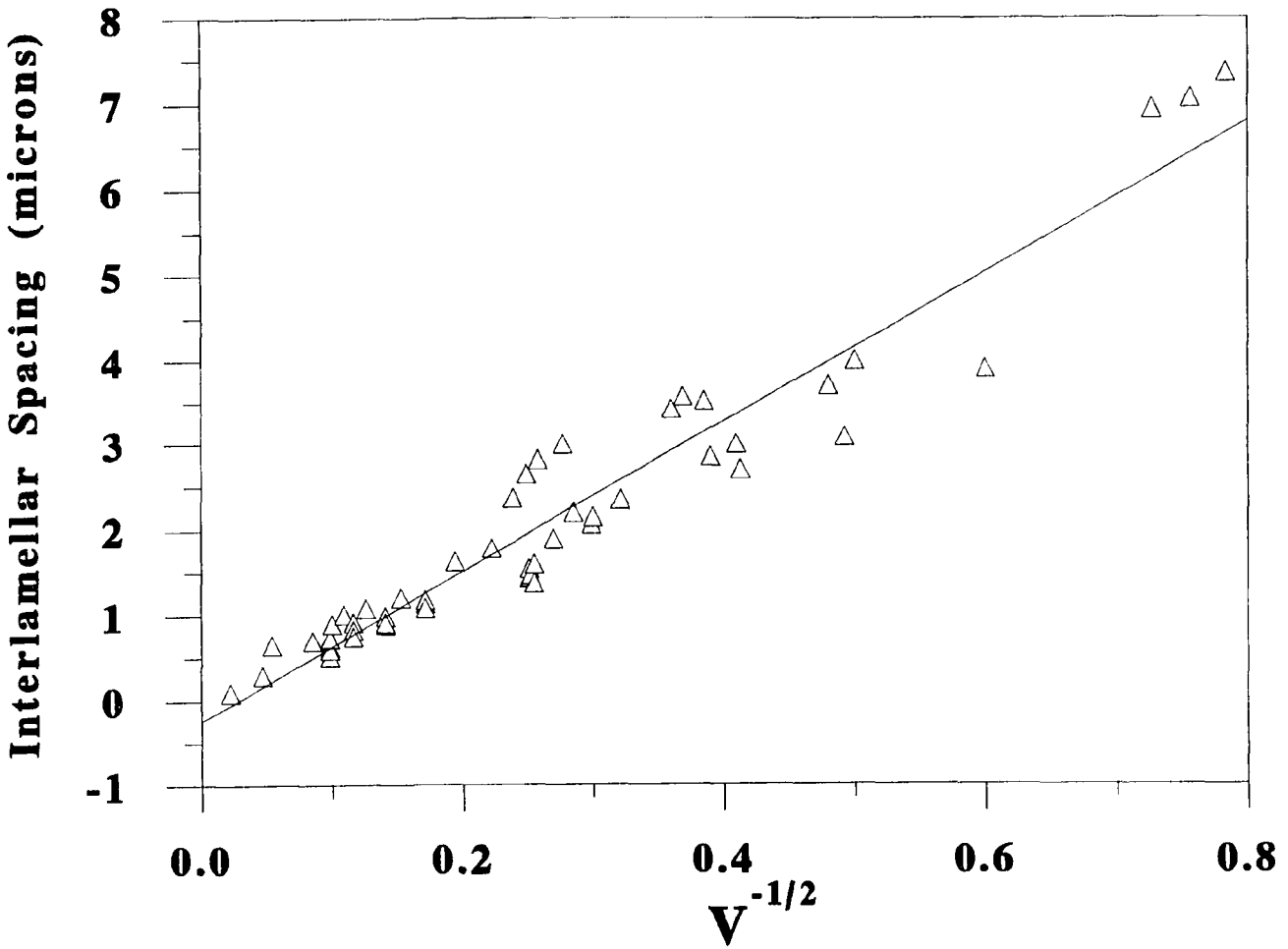

Figure 51. Interlamellar spacing as a function of $V^{-1/2}$ for the Al-Zn eutectic as collected from all published work on the subject.

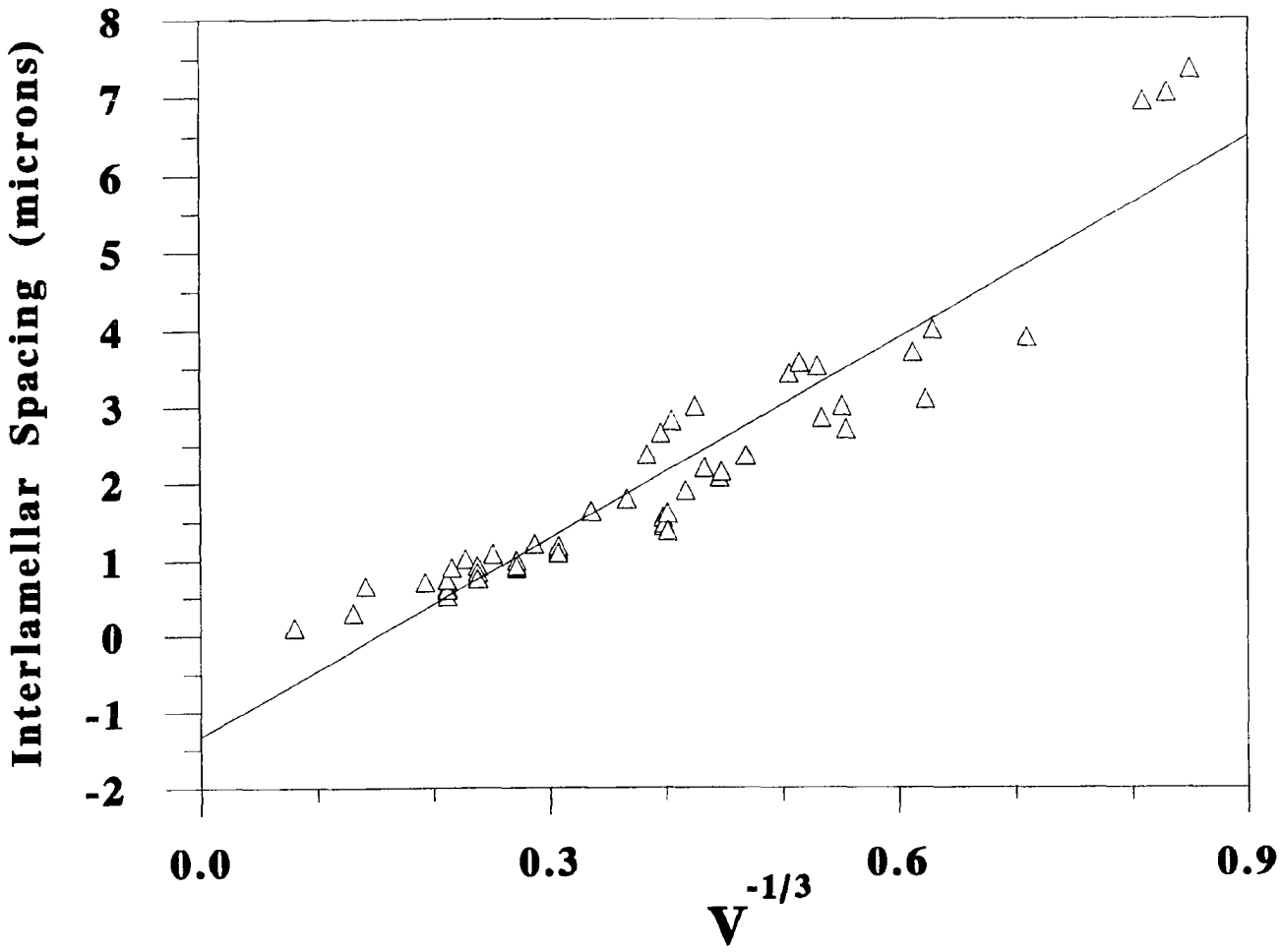

Figure 52. Interlamellar spacing as a function of $V^{-1/3}$ for the Al-Zn eutectic as collected from all published work on the subject.

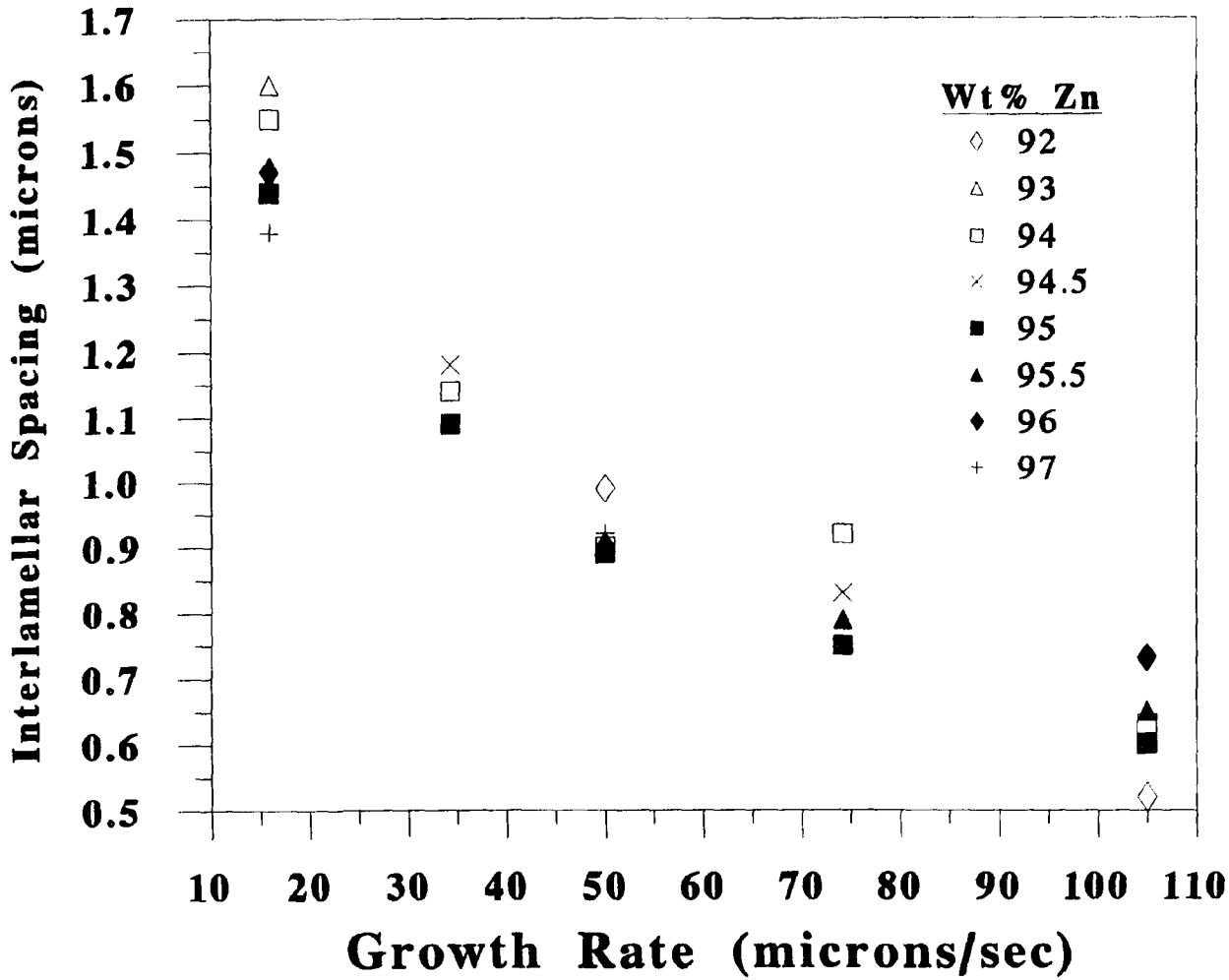

Figure 53. Interlamellar spacing as a function of growth rate and Al-Zn alloy composition.

composition. The difference between alloys solidified in the DSC and those directionally solidified regarding the dependence of λ on composition is due to nucleation and undercooling considerations. For the samples solidified in the DSC, the proeutectic dendrites served as the eutectic nucleation sites. Thus, as previously discussed, the eutectic structure was dependent on the ability of a proeutectic phase to serve as a nucleant for the other respective eutectic phase. Where the proeutectic phase was a poor nucleant of eutectic, as was the case for primary zinc dendrites, the large undercooling required for eutectic nucleation resulted in a finer lamellar structure when compared to alloys having aluminum as the proeutectic phase. For directionally solidified alloys, however, eutectic nucleation on preexisting dendrites usually does not occur and the growth rate is the primary factor which governs undercooling, and therefore, λ. Theoretically, the undercooling is derived as follows:

> as previously in the background section on "Eutectic Growth: Interlamellar Spacing and Interface Undercooling", the undercooling associated with an advancing eutectic solid/liquid interface can be expressed as (Jackson and Hunt 1966):
>
> $$\Delta T = \Delta T_c + \Delta T_r, \tag{8}$$
>
> or
>
> $$\Delta T = K_c \lambda V + \frac{K_r}{\lambda}. \tag{10}$$
>
> Since growth is assumed to occur at the minimum undercooling for a given interlamellar spacing,

$$\frac{d(\Delta T)}{d\lambda} = 0, \tag{11}$$

and therefore,

$$\lambda^2 V = \frac{K_r}{K_c}. \tag{13}$$

Solving for λ and substituting into (10) yields

$$\Delta T = 2\sqrt{K_c K_r V}, \tag{32}$$

or

$$\Delta T = \sqrt{V} \cdot constant. \tag{33}$$

Equation (33) shows that, for directionally solidified alloys, the interface undercooling will be a direct result of the growth rate. Furthermore, as the constants in equation (32) can be defined as

$$K_r = \frac{2(1-f)|m_\beta|\Gamma_\alpha \sin(\theta_\alpha) + 2f|m_\alpha|\Gamma_\alpha \sin(\theta_\alpha)}{f(1-f)(|m_\alpha|+|m_\beta|)} \tag{37}$$

and0

$$K_c = \frac{|m_\alpha||m_\beta|}{|m_\alpha| + |m_\beta|} \cdot \frac{C'}{2\pi D}, \tag{38}$$

where the variables are as previously described, and C' is the length of the eutectic tie-line and D is the diffusion coefficient in the liquid. Using the values listed in Table IV (p.81), and C'=15.7wt% and D=2.04E-09 m/s^2 (Liu and Jones, 1992a),

the theoretical undercooling for the Al-Zn eutectic as a function of growth rate can be calculated by means of equation (32). In order to compare theory with experimental results, the actual undercooling of the eutectic interface was estimated by using measured interlamellar spacing data to calculate the total interface undercooling as the sum of undercoolings from solute diffusion and lamellar curvature effects, where

$$\Delta T_c = K_c V\lambda \; ; \; \Delta T_r = \frac{K_r}{\lambda} \; . \tag{39}$$

The results can be seen in Figure 54, which shows the predicted and estimated interfacial undercooling as a function of growth rate. The measured λ values used to calculate the estimated undercoolings were average values for all alloy compositions and for each growth rate used. For all growth rates considered, the interface undercooling estimation from measured λ values was consistently greater than that predicted by theory (equation 32). Although this difference never exceeds 1°C, it does suggest that either the Al-Zn eutectic does not grow under extrenum conditions and thus the underlying assumptions of equation III.11 are not entirely valid, or that there is some other contribution to the interface undercooling such as the kinetic undercooling (Jackson and Hunt, 1966) which is not normally associated with the solidification of metallic systems. These possibilities are further discussed in the section "Interface Morphology and Thermodynamic Calculations for ß-Al" (p. 128).

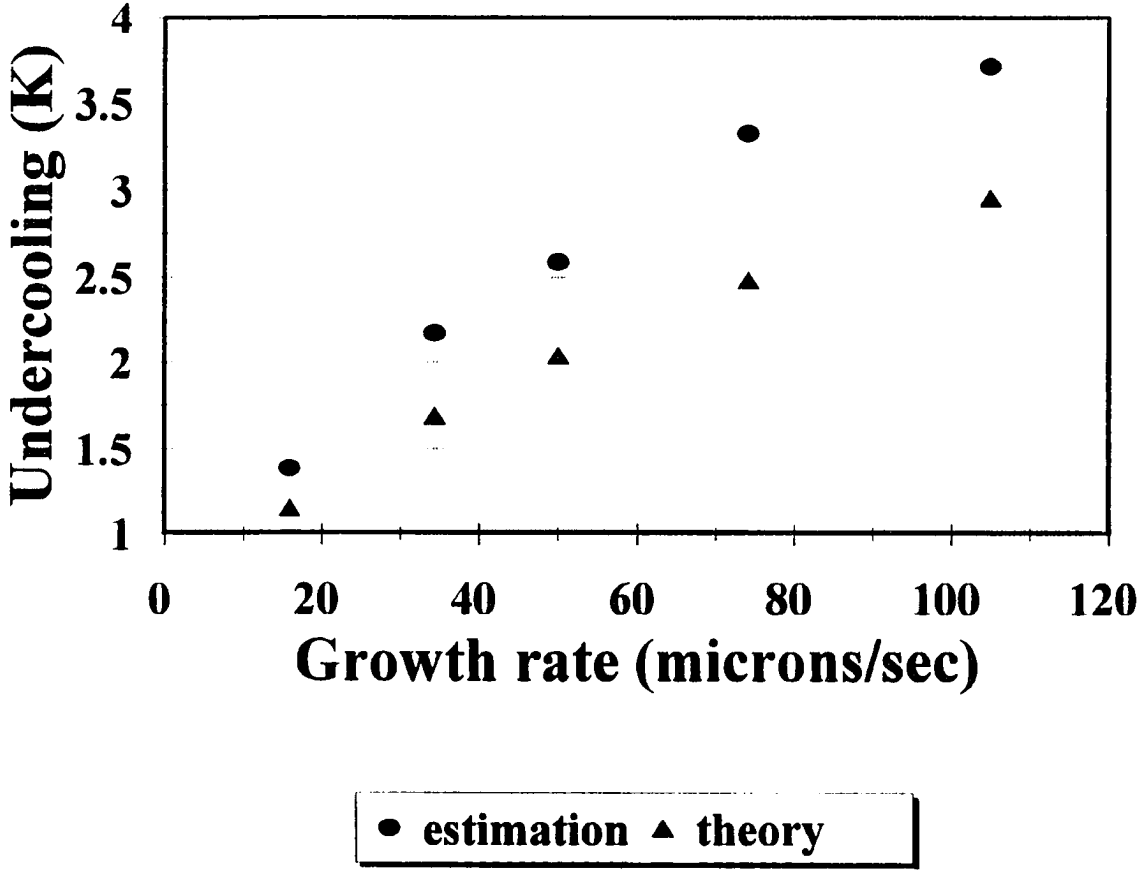

Figure 54. Predicted and estimated interfacial undercooling for directionally solidified alloys.

Volume Fraction of Second Phase in Eutectic and Eutectic Morphology

With few exceptions, the eutectic morphology for all of the directionally solidified alloys was lamellar in structure. Recalling Figure 47, the lamellar structure should be expected since the eutectic was measured to have an average volume fraction second phase (β-Al) of 0.47 $\pm$ 0.04 for all directionally solidified samples. For these samples, there was no significant difference between hypo- and hyper-eutectic Al-Zn alloys, which were measured to contain 0.46 $\pm$ 0.03% and 0.47 $\pm$ 0.04 β-Al, respectively. Rods were found in only two instances: (1) when the eutectic nucleated on a primary dendrite ahead of the solid/liquid interface, and (2) when the eutectic solidification front encountered a preexisting primary dendrite, causing a breakdown in the planar solid/liquid interface. Each of these are discussed in some detail below.

Given the relatively low temperature gradient in the liquid (G_{max}= 12.2 K/mm) for all directionally solidified alloys, it was common to find primary phase dendritic growth ahead of the eutectic solid/liquid interface regardless of growth rate. An example of this can be seen in Figure 55, which shows a quenched solid/liquid interface for a hypereutectic Al-Zn alloy. In this micrograph, primary η dendrites can be seen to exist a distance of approximately 800μm ahead of the eutectic interface at the time of the quench. Occasionally, and particularly for hypoeutectic alloys, some eutectic was found to nucleate on dendrites ahead of the eutectic interface. As shown in Figure 56, subsequent growth occurs outwardly from the dendrite to form abrupt interfaces when the eutectic front passes through the region. In Figure 56

200μm

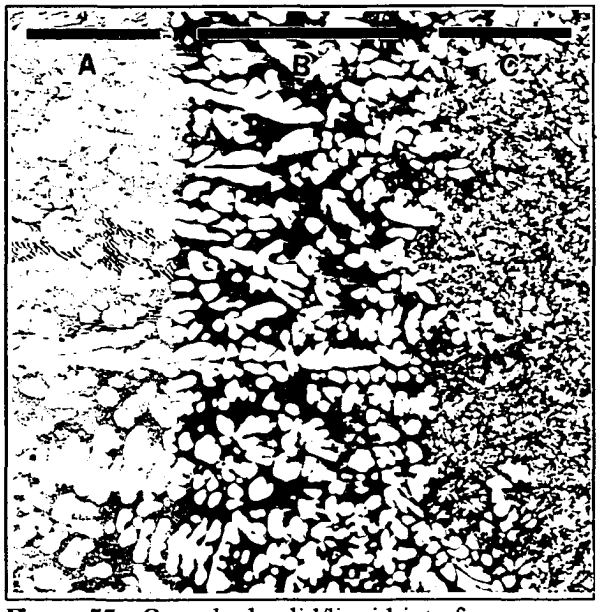

Figure 55. Quenched solid/liquid interface following directional solidification. (A=eutectic s/l interface, B=quenched zone containing η dendrites, C=non-melted material).

100μm

Figure 56. Directionally solidified Al-rich alloy. (A=directionally solidified eutectic, B=β dendrite, C=eutectic grown from β dendrite).

lamellar eutectic can be seen oriented to the direction of growth in regions where eutectic nucleation on β-Al dendrites has not occurred, and randomly-oriented lamellae and rods are found in eutectic regions where nucleation on the proeutectic phase has taken place. This phenomenon was found only for alloys grown at rates $\geq 50\mu$m/s, providing a basis for the following rationale: for alloys grown at high rates ($\geq 50\mu$m/s), the corresponding interfacial undercooling will be increased, thus leading to an increased temperature and time lag between a volume element of fixed position within the melt zone and the solid/liquid interface. At growth rates $\geq 50\mu$m/s, this lag becomes large enough to allow the temperature of a significant portion of eutectic liquid within the melt zone to drop below the equilibrium eutectic temperature. Any heterogeneous nucleation sites, such as proeutectic dendrites, can therefore nucleate the eutectic solid. In accordance with the previously discussed findings where proeutectic β-Al was found to nucleate eutectic with little undercooling, only nucleation on β-Al dendrites was found for directionally solidified alloys. Although η-Zn dendrites were found to grow ahead of the eutectic interface (Figure 55), nucleation on these dendrites was not observed for any growth rate.

In addition to nucleation and growth on a proeutectic dendrite resulting in a rod eutectic morphology, a breakdown of the normally eutectic lamellar structure was found in regions "behind" proeutectic dendrites due to a resulting change in local growth direction. In other words, because a preexisting dendrite disrupts the eutectic interface and the solute diffusion process to and from adjacent lamellae, the region immediately behind preexisting dendrites with respect to the growth direction will

have a rod eutectic structure. This is shown in Figures 57 and 58 for Al- and Zn-rich alloys, respectively. As can be seen from these micrographs, the regions containing the eutectic rod structure are often tapered in shape due to the influence of stable lamellar cells which surround the rod structure regions. The breakdown of stable Al-Zn lamellae into rods was also reported by Hunt and Chilton (1963b), who found that this transition would take place when the eutectic interface became curved for any reason. Hunt and Chilton cite the examples of growth around a mechanical obstacle or dendrite, and the formation of a curved eutectic interface due to impurity additions and resultant cell formation.

There are several differences between the rod eutectic regions formed due to nucleation on proeutectic dendrites and those formed due to the disruption of the solid/liquid interface. The two are easily distinguished by the positioning of rod eutectic growth: for regions which have nucleated on preexisting dendrites, growth will occur in all directions from the dendrite and there will be an abrupt, rough interface with the lamellar eutectic regions; for regions which form due to the disruption of the interface, growth is limited to the regions behind the dendrites and there is a smooth interface with the lamellar regions. More significantly, there is a measurable difference between the volume fraction second phase (β-Al) between the two rod-type regions. It can be expected that when the eutectic nucleates on the β-Al proeutectic dendrites near the equilibrium eutectic transformation temperature as discussed in the previous paragraphs, the amount of β-Al in the eutectic will closely correspond to that predicted by the use of the lever rule and the equilibrium phase

50μm

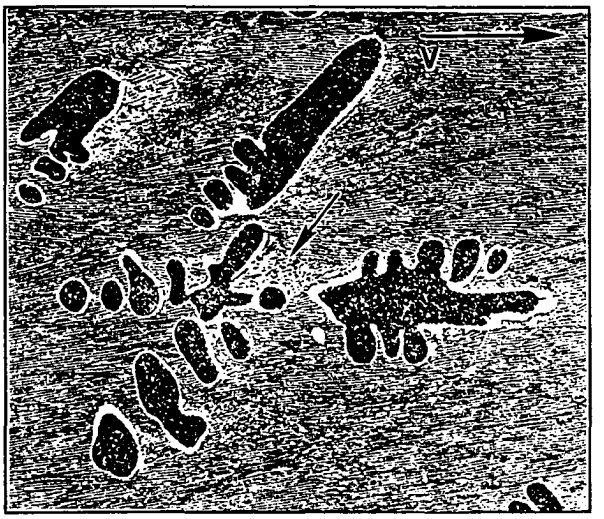

Figure 57. Breakdown of lamellar structure due to the disruption of the eutectic interface by a proeutectic β-Al dendrite.

50μm

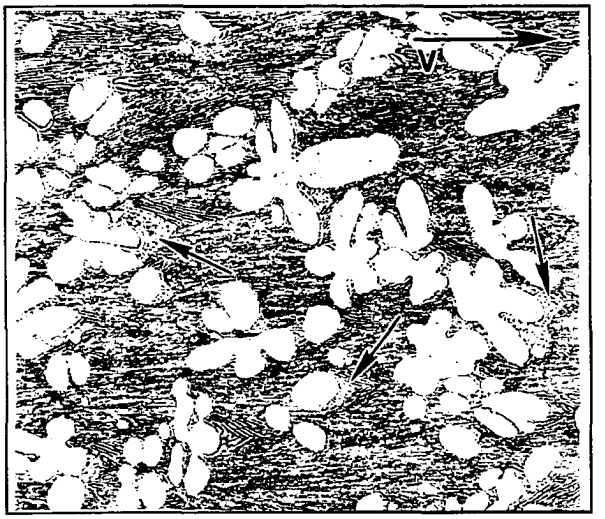

Figure 58. Breakdown of lamellar structure due to the disruption of the eutectic interface by η-Zn proeutectic dendrites.

diagram (the reader is referred to the section "Eutectic Growth: Volume Fraction of Second Phase in Eutectic"). The volume fraction β-Al in these rod eutectic regions was measured to be 0.24 $\pm$ 0.04, which is compared to a value of 0.28 as calculated from the phase diagram. In contrast, a value of 0.34 $\pm$ 0.03 measured for the rod regions formed due to the disruption of the eutectic interface from proeutectic dendrites. This confirms that the breakdown to a rod structure is due to eutectic interface disturbances rather than undercooling considerations, since as shown in Figure 47 and confirmed by samples solidified with the use of the DSC, a lamellar structure is energetically more favorable at second phase volume fractions greater than 0.28.

Comparison of DSC and DS Results: Volume Fraction of Second Phase in Eutectic and Eutectic Morphology

Recalling the microstructural observations regarding eutectic morphology found for samples solidified in the differential scanning calorimeter, hypoeutectic Al-Zn alloys possessed a rod structure regardless of cooling rate and composition, while hypereutectic alloys always contained a lamellar or a mixed lamellar and rod structure. The microstructures of these samples are analogous to cast structures, where the undercooling required for eutectic nucleation on proeutectic phases dictate the resultant structure. This is in contrast to directionally solidified samples, where the undercooling and resultant structure is primarily a function of growth rate and is irrespective of alloy composition. The only exception to this is when eutectic nucleation occurs on primary phase dendrites growing ahead of the interface, which

only occurs at growth rates ≥50μm/second.

Regardless of how the Al-Zn eutectic is solidified, the above results indicate interface undercooling to be the controlling factor in determining the volume fraction second phase in the eutectic and the eutectic morphology. An excellent example of this can be seen by comparing Figure 59 to Figure 57, which show the as-cast and directionally solidified regions of the same Al-rich off-eutectic Al-Zn alloy, respectively. As a cast structure (Figure 59), this alloy possesses a rod eutectic structure having a volume fraction second phase (β-Al) of 0.28 ± 0.02. The same alloy, directionally solidified at 15.9μm/second, has a lamellar structure with a volume fraction second phase (β-Al) of 0.46 ± 0.03. The eutectic in the cast structure

50μm

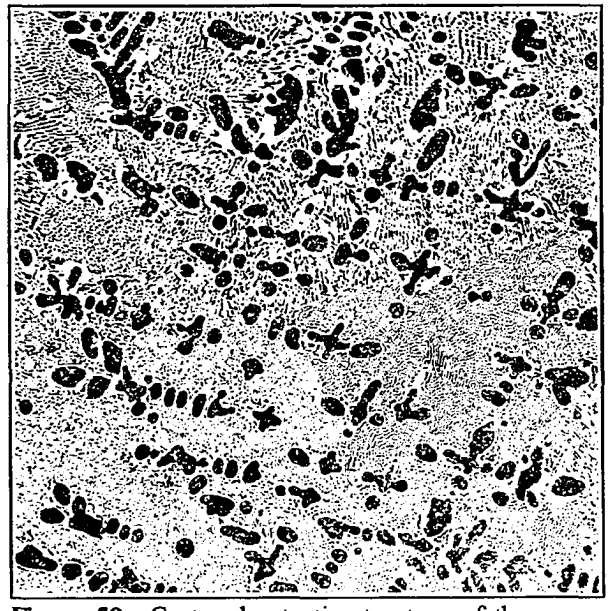

Figure 59. Cast rod eutectic structure of the directionally solidified alloy shown in Figure 57.

nucleated on preexisting β-Al dendrites with a relatively small undercooling along the Al liquidus, resulting in a eutectic structure having a volume fraction of phases equal to that predicted by the equilibrium phase diagram. When directionally solidified, the eutectic structure of this same alloy is altered due to an apparently significant imposed undercooling which is dictated by growth rate. The large increase in the volume fraction of β-Al in the eutectic, which was found for all directionally solidified alloys (average β-Al of 0.47 ± 0.04), suggests that the eutectic point is "shifted" to higher aluminum concentrations during directional solidification. The exact effects of solidification conditions on stable microstructural growth is further discussed in the section "Coupled Zone and Microstructure Map for the Al-Zn Eutectic".

Coupled Zone and Microstructure Map for the Al-Zn Eutectic

The coupled zone for a eutectic system defines the range of solidification conditions, i.e. composition and undercooling, which will produce a pure eutectic structure without primary phase growth. Generally, the structure which grows with the highest velocity at a given undercooling, or with the lowest undercooling at a given velocity, will be preferred by the system and will constitute the resultant microstructure (Jackson, 1968). As discussed in the Background of this thesis, a coupled zone may be symmetric about the eutectic composition, or it may be skewed to one side of the eutectic. The zone is normally symmetric about the eutectic composition for most metallic systems as shown in Figure 15 since most metals grow anisotropically. In systems where one of the eutectic phases grows anisotropically or requires a high undercooling for nucleation, a skewed couple zone may exist as shown in Figure 16.

The coupled zone for the Al-Zn eutectic has been suggested to be skewed to the Al-rich side of the eutectic (Spittle, 1977). In this reference, it is argued that since Zn halos are found surrounding Al proeutectic dendrites, this is a probable indication that Al is a better nucleant of Zn than vice-versa and therefore, the coupled zone of growth may be skewed to the Al-rich side of the eutectic. These suggestions are made, however, in the absence of any quantitative data.

The results obtained via directional solidification facilitate a determination of the Al-Zn microstructure map. By noting the sample microstructure and estimating the undercooling encountered during directional solidification in the manner described

in the section "Comparison of DSC and DS Results: λ", the experimentally determined coupled zone is shown in Figure 60. Unlike other studies which speculate on the placement of the coupled zone for the Al-Zn system (Spittle, 1977), Figure 60 offers a quantitative assessment of the Al-Zn microstructure map.

As can be seen in Figure 60, the coupled zone of growth is skewed to the Al-rich side of the eutectic. Such a skewed zone is considered to be unusual for metallic systems, particularly when both eutectic phases are classified as non-faceted. The reason for the skewed zone is not immediately evident, but it may be related to the findings discussed in the section "Comparison of DSC and DS Results: λ", which suggest the Al-Zn eutectic to grow under non-extrenum conditions. If this is the case, it may be that one of the phases, namely β-Al, requires a significant kinetic undercooling for growth, thus slowing its growth rate and permitting the eutectic to outgrow β-Al dendrite formation for a wide range of interfacial velocities and undercoolings. This concept becomes more fully apparent when considering Figures 15 and 16, which are reproduced below. Figure 15 teaches that, for a symmetric coupled zone, the β phase in a β-rich off-eutectic alloy will have the highest growth rate for a given undercooling, or the lowest undercooling for a given growth rate, for almost all V-ΔT combinations. Only at very low and high undercoolings will the system enter the coupled zone wherein the eutectic structure outgrows the β phase. For a skewed coupled zone as shown in Figure 16, the growth rate of β is slower, resulting in eutectic formation at lower undercoolings and growth rates when compared to a symmetric coupled zone.

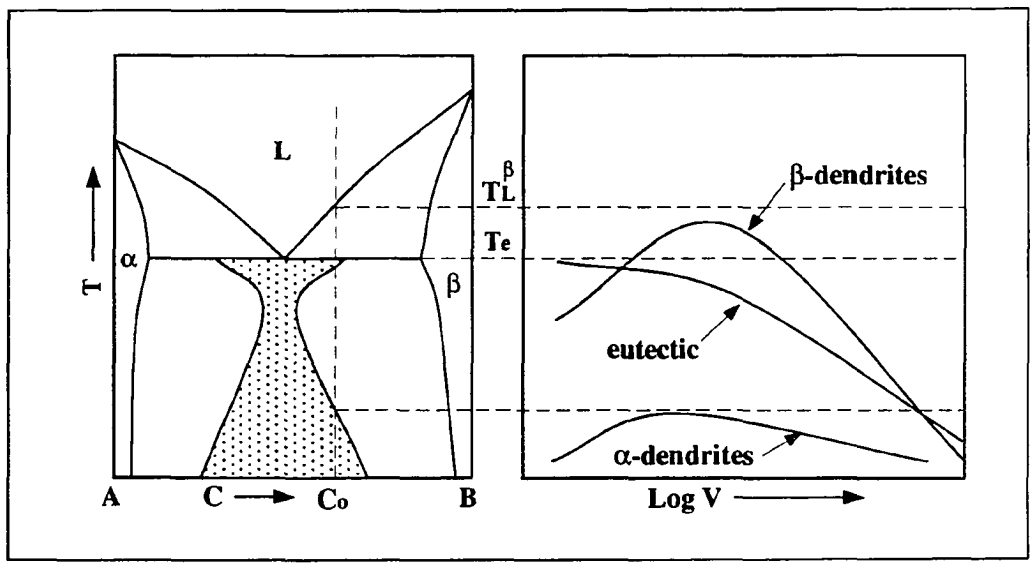

Figure 15. Coupled zone and corresponding temperature-velocity diagram for a normal eutectic system.

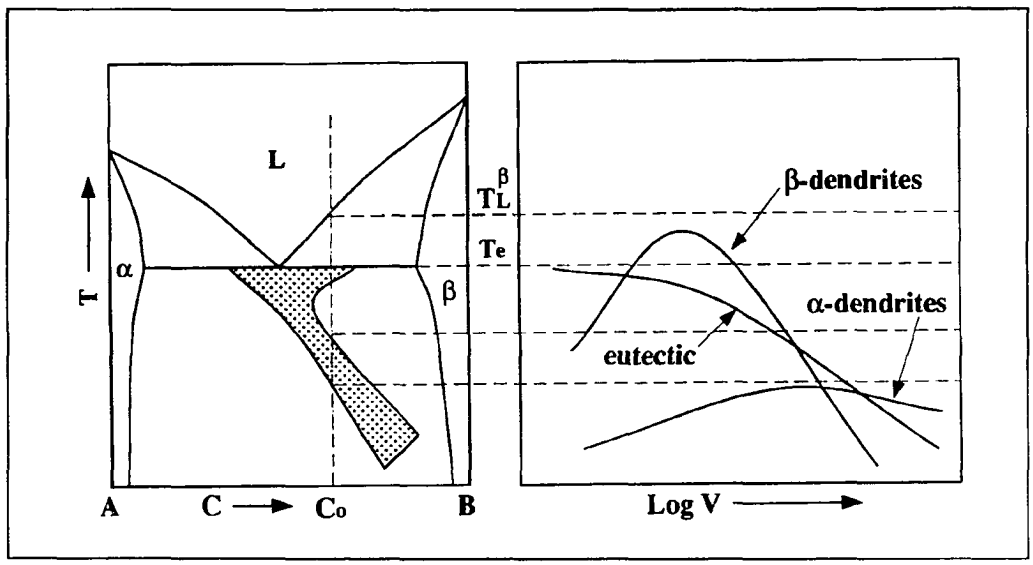

Figure 16. Skewed coupled zone and corresponding temperature-velocity diagram for a eutectic system where one phase grows anisotropically or may require a large undercooling for growth.

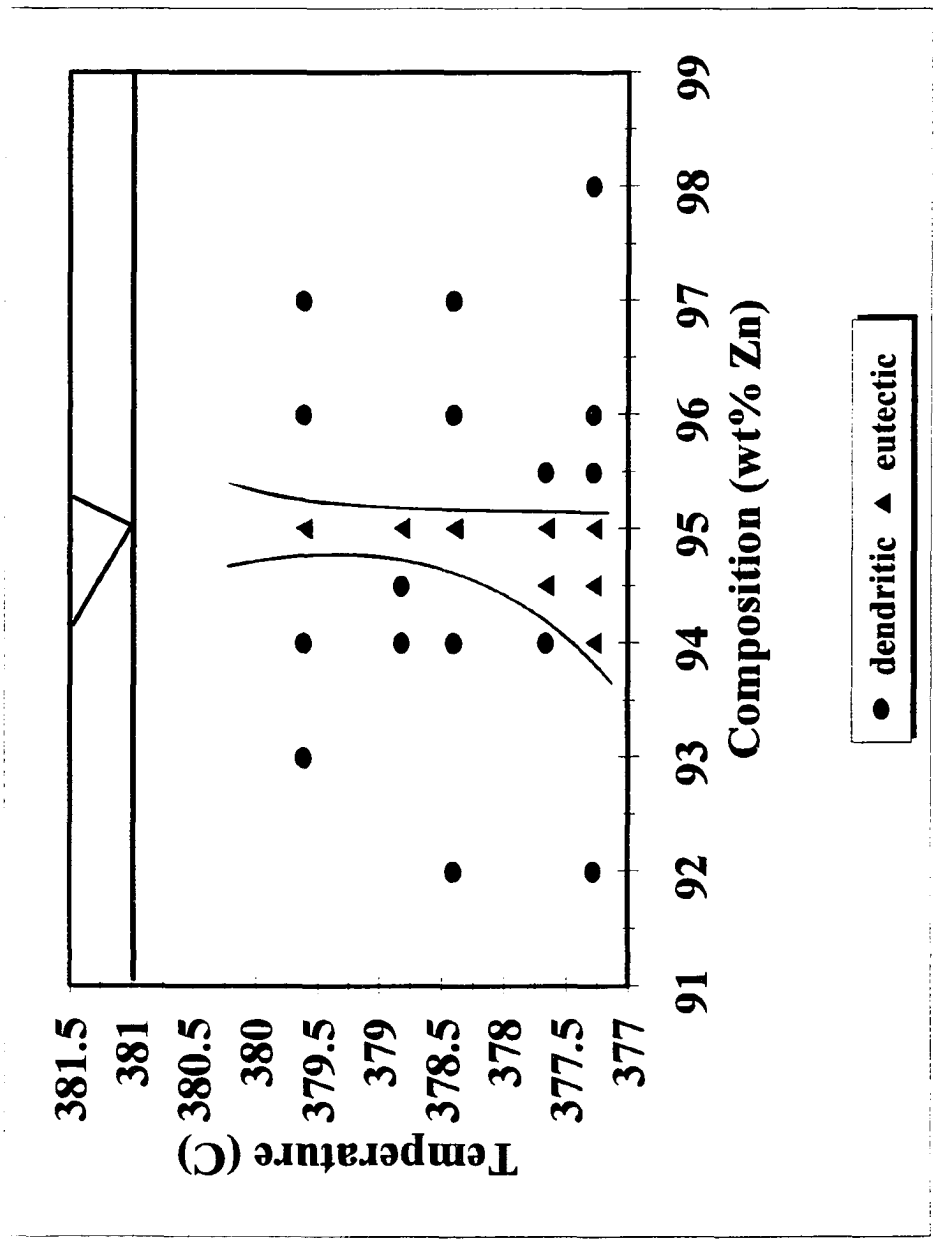

Figure 60. Proposed microstructure map for the Al-Zn eutectic.

As discussed in the Background section "The Eutectic-Dendritic Transition", there have been different approaches to the theoretical prediction of stable microstructures for eutectic systems. Mollard and Flemings (1967) qualitatively showed good agreement between the predictions of the constitutional supercooling criterion (CSC) and the experimentally determined dendritic-eutectic transition. In contrast, Hunt and Jackson (1967), and later Jackson (1968) argue that the competitive growth criterion dictates the stable microstructure, wherein the structure with the highest growth rate at a given undercooling (or with the lowest undercooling at a given growth rate) will be preferred and constitutes the solidified morphology. The results obtained in the present study were compared with the predictions of the CSC in order to determine if the CSC is relevant to the Al-Zn eutectic during unidirectional solidification. According to the CSC, a planar eutectic interface is expected to be stable when

$$\frac{G}{V} \geq -\frac{m(\Delta C_o)}{D}, \qquad (40)$$

or when growth occurs in the presence of a high temperature gradient in the liquid and/or at low growth rates. Using values of m_β=-8.0 K/wt%, m_η=10.2 K/wt%, D=2.04 E-09 m/s^2 (Liu and Jones, 1992a), and ΔC_o= the difference between the alloy and eutectic compositions, the CSC was calculated for the Al-Zn system as shown by the dashed line in Figure 61. As can be seen in the graph, the CSC predicts a stable eutectic microstructure for a very narrow range of alloy compositions and G/V values, as mixed eutectic + dendritic microstructures are expected outside of

the dashed line. Experimentally determined G/V values and corresponding resultant microstructures are also shown in this graph. As is clearly seen in Figure 61, the CSC does not accurately predict the stable microstructure for the Al-Zn system. At low G/V values, pure eutectic microstructures are formed in off-eutectic Al-rich alloys. Since G, the temperature gradient within the liquid, was similar and low for all samples (2.9-12.2 K/mm), the samples which did not conform to the CSC were generally grown at relatively high velocities, and therefore, higher undercoolings. This is in agreement with the microstructure map as shown in Figure 60. The conclusion of these observations must be that the Al-Zn microstructure is determined by the competitive growth criterion as described above, where the structure which grows with the greatest velocity at a given undercooling is most stable and will comprise the final microstructure. As the interfacial undercooling increases during solidification, the eutectic outgrows β-Al dendritic formation and will therefore be formed at hypoeutectic Al-Zn compositions.

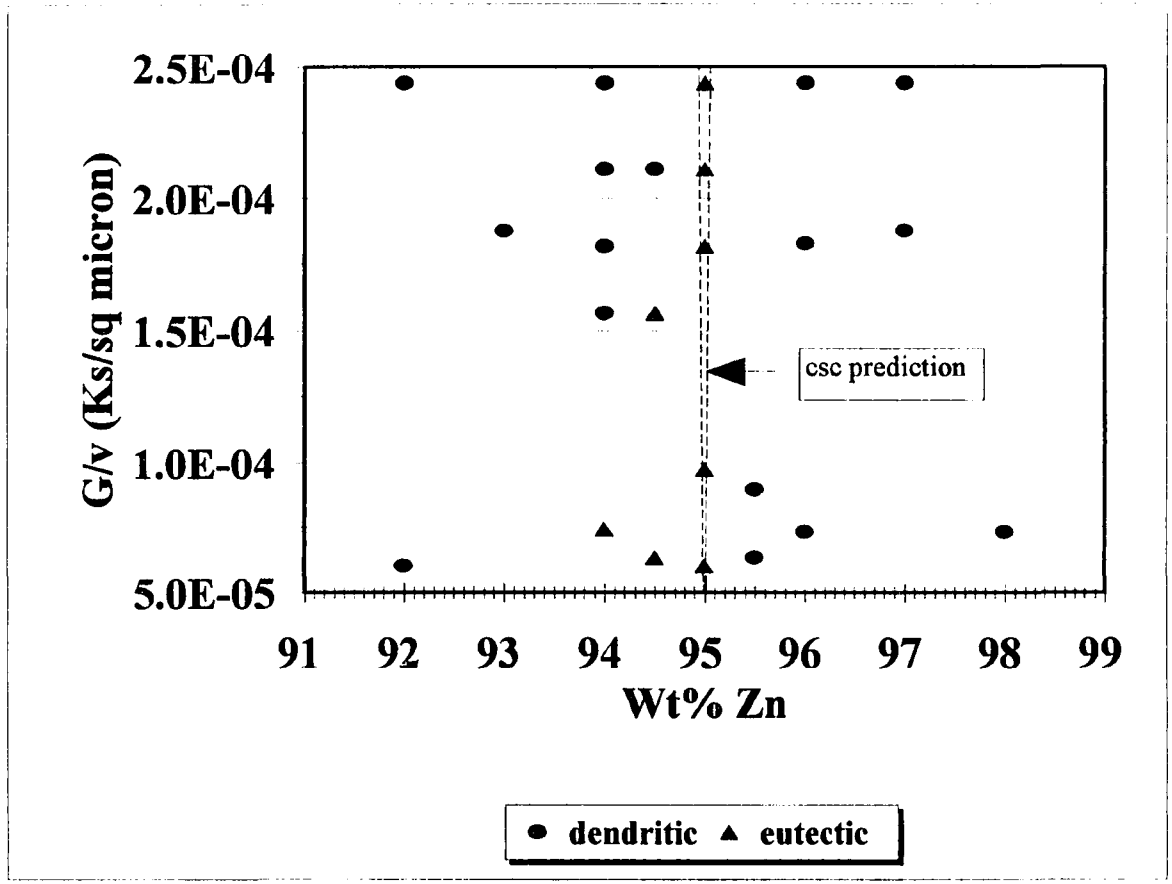

Figure 61. Observed microstructures as a function of G/v and alloy composition. The narrow range of stable eutectic growth as predicted from the constitutionally supercooling criterion is shown.

Zinc halos in unidirectionally solidified samples

Zinc halos around β-Al dendrites were found for all directionally-grown hypoeutectic Al-Zn samples. The widths of these halos were found to be dependent on sample growth rate and the eutectic structure of the surrounding matrix. As shown in Figure 62, the average halo width was found to be greater when in a rod eutectic matrix than when in a matrix of lamellar eutectic. Examples of halos in both types of eutectic for a directionally solidified hypoeutectic Al-Zn alloy can be seen in Figure 63. The mechanism for halo formation in the rod eutectic regions, which form when there is a significant distance between the eutectic interface and β-Al dendrites growing ahead of the interface, is analogous to that for the cast structures solidified in the DSC. As previously discussed, the size of halos formed by this mechanism is limited by the growth rate of the Zn as a halo and the time necessary to reach the temperature at which Zn will nucleate Al. It follows, therefore, that the halo width should be inversely proportional to growth rate as shown in Figure 62. The halos formed in lamellar eutectic regions can be said to have been formed with little undercooling, because eutectic nucleation on these halos did not occur. The size of these halos are limited by the distance between the eutectic interface and the β-Al dendrites because halo growth is interrupted when enveloped by the growing eutectic interface. Since the size of the halos in lamellar eutectic regions was found to decrease with an increasing growth rate (Figure 62), it can be hypothesized that the distance between the eutectic interface and the β-Al dendritic growth ahead of the interface generally decreases with an increase in growth rate. This is in agreement

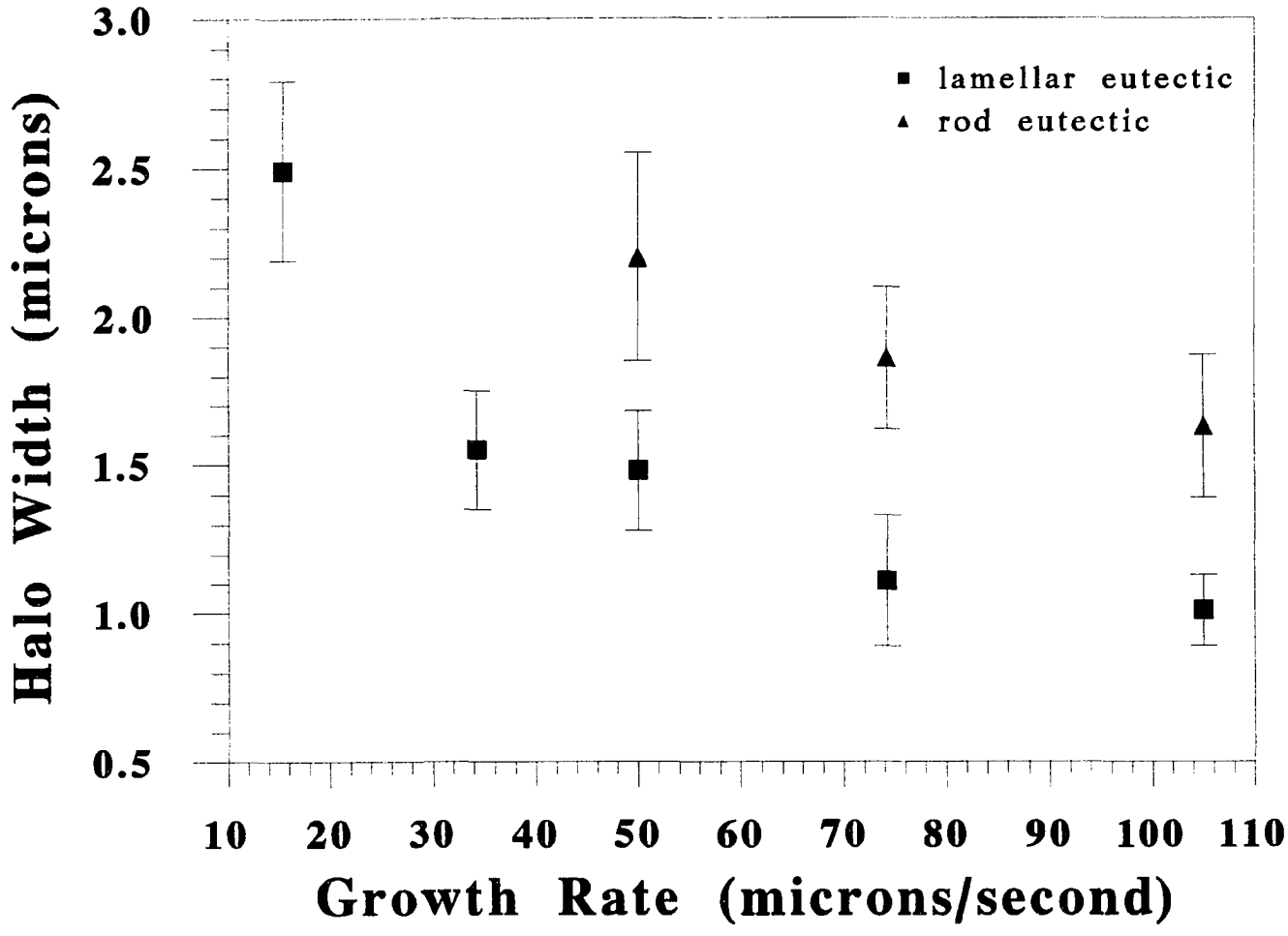

Figure 62. Zinc halo width as a function of growth rate for directionally solidified hypoeutectic Al-Zn alloys.

with Figure 60, which suggests that velocity of the eutectic increases relative to the velocity of β-Al dendritic growth with an increase in undercooling (or imposed growth rate).

Although the size of halos in directionally solidified samples is related to the

Figure 63. Directionally solidified Al-rich Al-Zn alloy showing zinc halos around β-Al dendrites in (A) rod and (B) lamellar eutectic regions.

coupled zone of growth as described above, the results of this study indicate that the mechanism for halo formation is unrelated to the coupled zone. As previously described, Zn halos around proeutectic Al form as a result of Zn being a poor nucleant of Al. Since proeutectic Al will readily nucleate Zn, but Zn requires a significant undercooling to nucleate Al, Zn halos will grow about Al proeutectic dendrites until the liquid becomes significantly undercooled, thus forcing Al nucleation. This theory

is in contrast to the current literature on halo formation (Gigliotti et al., 1970) (Barclay et al., 1973) (Yilmaz and Elliott, 1984) (Suk et al., 1992), which relates halo formation to the competitive growth between phases and the coupled zone of growth.

Banding

Directionally solidified alloys containing 94-96wt% Zn grown at ≤50μm/second were found to have macroscopic bands oriented normal to the growth direction (Figure 64). Banding in directionally solidified Al-Zn alloys has not previously been reported in the literature. As shown in Figure 64, these bands are continuous across different eutectic grains, indicating that the banding mechanism is associated with the solid/liquid interface. As pointed out elsewhere for banding in Al-$CuAl_2$ alloys (Kraft and Albright, 1961), bands delineate isotherms at different times during directional solidification. When observed at higher magnifications, these banded regions can be seen to be precipitation zones for either of the two eutectic phases. The precipitation of β-Al and η-Zn phases can be seen in Figures 65 and 66, respectively. A more striking example of η-Zn can be seen in Figures 67 and 68, which show low and high magnification micrographs of band formation at a quenched solid/liquid interface, respectively.

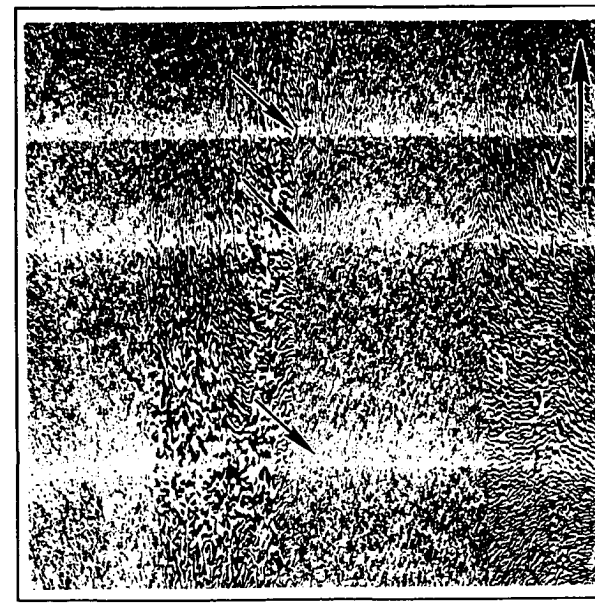

Figure 64. Banding in directionally solidified Al-Zn alloy.

50μm

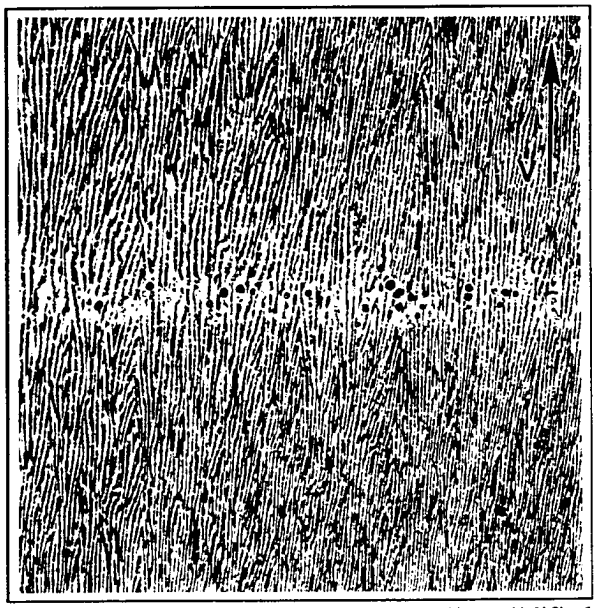

Figure 65. β-Al banding in directionally solidified Al-Zn alloy.

100μm

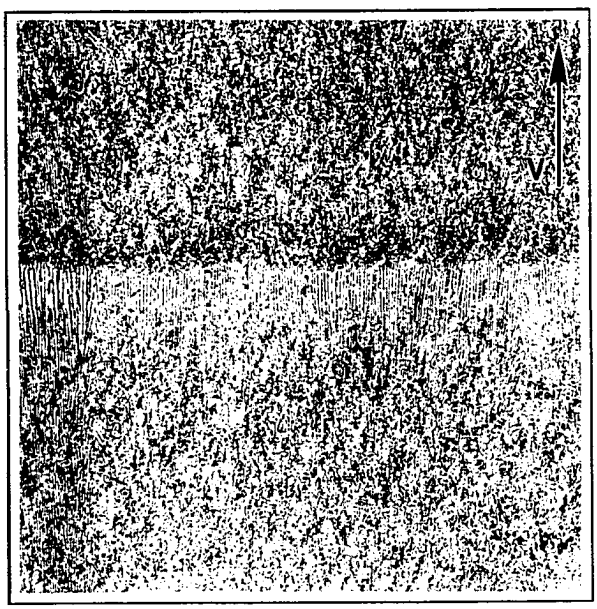

Figure 66. η-Zn banding in directionally solidified Al-Zn alloy.

200μm

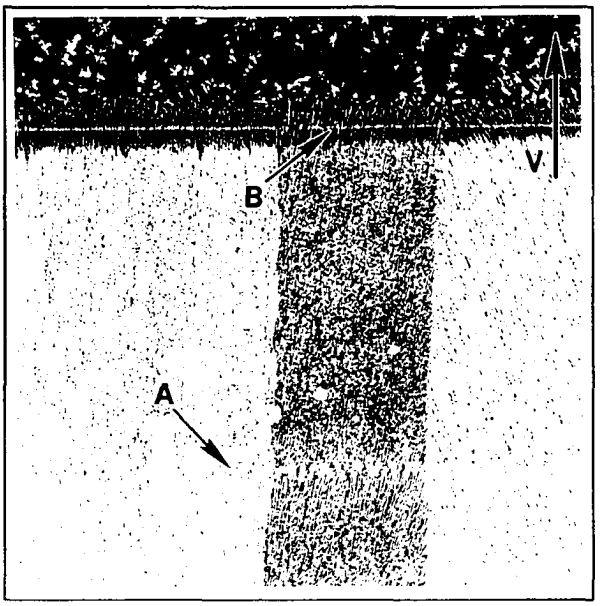

Figure 67. η-Zn banding in matrix (A) and at quenched solid/liquid interface (B) for a directionally solidified Al-Zn alloy.

50μm

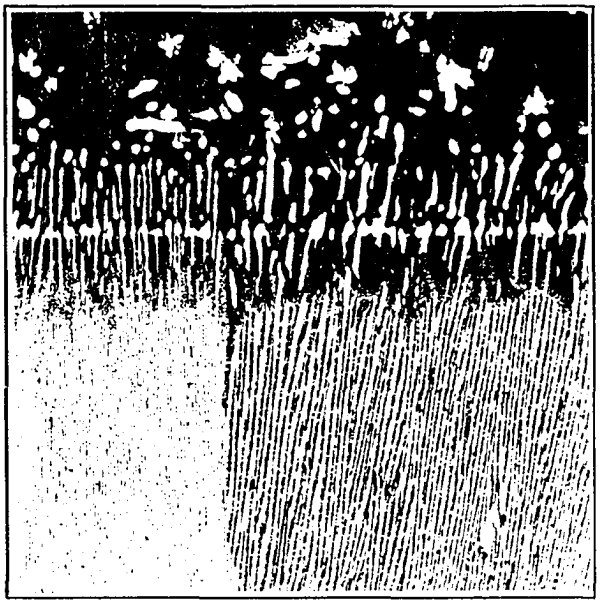

Figure 68. Higher magnification view of the quenched solid/liquid interface shown in Figure 67.

There are two explanations for the banding found for the present set of experiments. The first, as proposed by Kraft and Albright (1961) for banding in Al-$CuAl_2$ alloys, is that at low enough growth rates, the solute distribution in the melt is sufficiently uniform to result in the lateral solidification of the solute when its solubility level is reached. So during eutectic growth, when one of the solute or eutectic phases accumulates at the solid/liquid interface to a concentration which cannot be absorbed by the growing eutectic or sustained as a boundary layer by the advancing interface, a precipitation of that phase will occur as a band. At higher growth rates, the solute is absorbed by the growing eutectic, possibly resulting in a breakdown of the planar interface into cells. Two separate studies on the directional solidification of the Al-$CuAl_2$ have observed banding at only low growth rates (Jordan and Hunt, 1971) (Kraft and Albright, 1961), giving credence to this explanation. The second possible explanation for banding is that there were slight changes in growth rates, jogs, or power variations during directional solidification in this and other studies which reported banding. At least one of the cited references (Kraft and Albright, 1961) recognize that this may have been a factor, but claim this to be unlikely since banding was encountered for two separate groups of experiments using different solidification techniques. In the present work, the growth rate of the zone refiner has been carefully calibrated, yielding the near-perfect linear relationship shown in Figure 69 between velocity setting and the measured growth rate. Any changes in growth rate during experimentation were therefore improbable. In addition, the bands were not regularly spaced from each other and thus, an

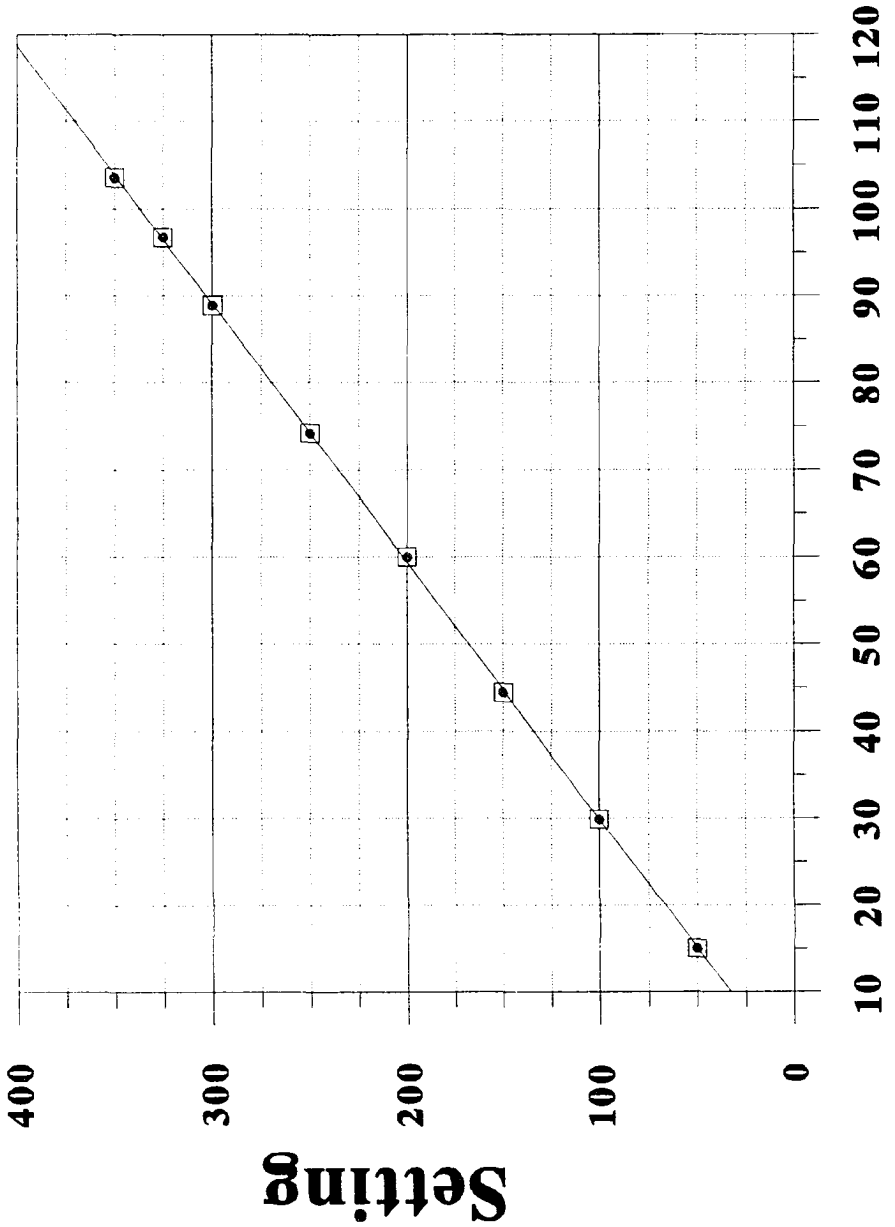

Figure 69. Zone refiner apparatus traverse rate setting as a function of measured velocity.

irregularity in the zone refiningapparatus drive mechanism also seems unlikely because this would produce a regularly-repeating jog in the growth rate and corresponding band spacing.

In light of the above discussion, it is theorized that banding in directionally solidified Al-Zn alloys is the result of solute accumulation ahead of the solid/liquid interface and subsequent precipitation. However, there are still some remaining aspects of the banding mechanisms which remain unclear. For example, it is not known why some bands form by the adjustment of the eutectic interlamellar spacing and the volume fraction of the phases as shown in Figure 66, while other bands form by phase precipitation ahead of the solid/liquid interface as shown in Figures 65, 67 and 68. The temperature gradient in the melt (G) may play a role in banding microstructural development because a high G would prevent phase growth ahead of the interface, but a more detailed study with a wider range of G values is necessary to determine the effects of G on banding more conclusively.

Interface Morphology and Thermodynamic Calculations for β-Al

The heat and entropy of fusion for β-Al is of particular interest in studying the Al-Zn eutectic reaction. Because there is some question about whether the system grows at the extrenum condition or if there is a significant kinetic undercooling contribution to the total interfacial undercooling, the interpretation of thermodynamic data can be useful for making such determinations. Results presented in this thesis which suggest non-extrenum growth for the Al-Zn system, or a large kinetic undercooling associated with β-Al growth include the following:

1. interfacial undercooling estimations during directional solidification exceeding theoretical predictions,

2. a decreasing distance between the eutectic interface and ß-Al dendritic growth ahead of the interface with an increasing growth rate during directional solidification,

3. a skewed coupled zone of growth to the ß-Al side of the Al-Zn eutectic, and

4. a sometimes apparently faceted ß-Al interface (see Figure 37, p. 71).

Perhaps the most often used indicator of interfacial growth mechanism and associated

undercooling is Jackson's α-factor, which can be used to predict interfacial roughness (Jackson, 1958). Based on a statistical analysis assuming equilibrium between a solid interface and a melt of identical composition and that the interfacial roughness would be dictated by free energy considerations, Jackson derived the interfacial energy of a solid/liquid interface to depend on the interface morphology as follows:

$$\frac{\Delta G_s}{NkT_E} = \alpha N_A \frac{N-N_A}{N^2} - \ln \frac{N}{N-N_A} - \frac{N_A}{N} \ln \frac{N-N_A}{N_A} \quad ,$$

where ΔG_s is the interfacial free energy, α is a dimensionless entropy factor = $\Delta S_f/R$, N is the number of sites a solid atom can attach itself to the solidifying interface and N_A is the number of atoms existing on a plane of the growing interface. In other words, if $N_A/N = 0.5$, half of the available sites on the growing interface will be occupied and the interface is said to be completely "rough". If $N_A/N = 0$ or 1, none or all of the available sites on a growing plane will be occupied, and the interface is said to be atomically flat or faceted. The dependence of the free energy of a solidifying system on α can be seen in Figure 62, which plots free energy as a function of N_A/N for various α values. It can be seen from the graph that for materials with high entropies of fusion (ΔS_f) and therefore high α's (≥ 2), the free energy of the system will be minimized with a faceted solid/liquid interface. Such growth occurs slowly and requires a significant kinetic undercooling for interfacial movement. For most metallic systems, however, $\alpha \approx 1\text{-}1.5$, and growth usually occurs with a rough or non-faceted interface.

The thermodynamic data for pure zinc and aluminum are well known (Liu and

Jones, 1992a) and suggest the Al-Zn eutectic phases to grow with non-faceted interfaces. However, the aluminum phase in the Al-Zn eutectic reaction L → η(Zn) + β(Al) actually contains more zinc than aluminum (67.0at%, 83.1wt% Zn), and the thermodynamic properties of this phase at such compositions have not been characterized. In addition, this phase sometimes gives the appearance of being faceted, as shown in Figure 37, thus suggesting a high entropy of fusion and α-factor. The heat and entropy of fusion for this phase was determined from data obtained from the DSC solidification experiments cooled at 1 K/min. The method of calculation is as follows:

$$\Delta H = \frac{k\ (\textit{area under the proeutectic}\ \beta\ \textit{peak})}{(\textit{mass fraction proeutectic}\ \beta)(\textit{total sample weight})},$$

where k is a constant for the DSC cell (0.75 in this case), and

$$\textit{mass fraction proeutectic}\ \beta = (\textit{vol fraction}\ \beta)\left(\frac{\rho_\beta}{\rho_{\textit{eutectic}}}\right).$$

The density of the β-Al phase and the eutectic can be calculated as:

$$\rho_\beta = \frac{M}{V} = \frac{4(0.33(26.98)+0.67(65.38))}{(6.02E\ 23)\ (4.030E\text{-}8)^3} = 5.35\ g/cm^3$$

$$\rho_{\textit{eutectic(rod)}} = 0.26(\rho_\beta) + 0.74(\rho_\eta) = 0.26(5.35) + 0.74(7.13) = 6.67\ g/cm^3\ .$$

The heat of transformation is therefore

$$\Delta H = \frac{0.75\ A}{(\textit{vol fraction}\ \beta)\ (5.35/6.67)\ (\textit{total sample mass})}\ .$$

Using the data collected for eight (8) hypoeutectic Al-Zn alloys, the influence of the

high zinc content in β-Al was found to be almost negligible. The heat of fusion (ΔH_f) and the entropy of fusion at the solidification temperature (ΔS_f) were calculated to be 7.53 $\pm$ 2.34 kJ/mol and 10.9 $\pm$ 3.49 J/mol$\cdot$K, respectively, compared to 9.49 kJ/mol

and 10.2 J/mol$\cdot$K reported in the literature. The resulting α-factor for β-Al is calculated to be $\Delta S_f/R = 1.31 \pm 0.42$, which closely corresponds to the 1.36 value cited by Jackson in the original work on alpha (Jackson, 1958).

Based on the analysis, it seems improbable that a significant kinetic undercooling is necessary for β-Al growth. According to the well-accepted theory of Jackson (1958), solidification of this phase should proceed with an atomically rough, non-faceted interface, as has been found for pure aluminum.

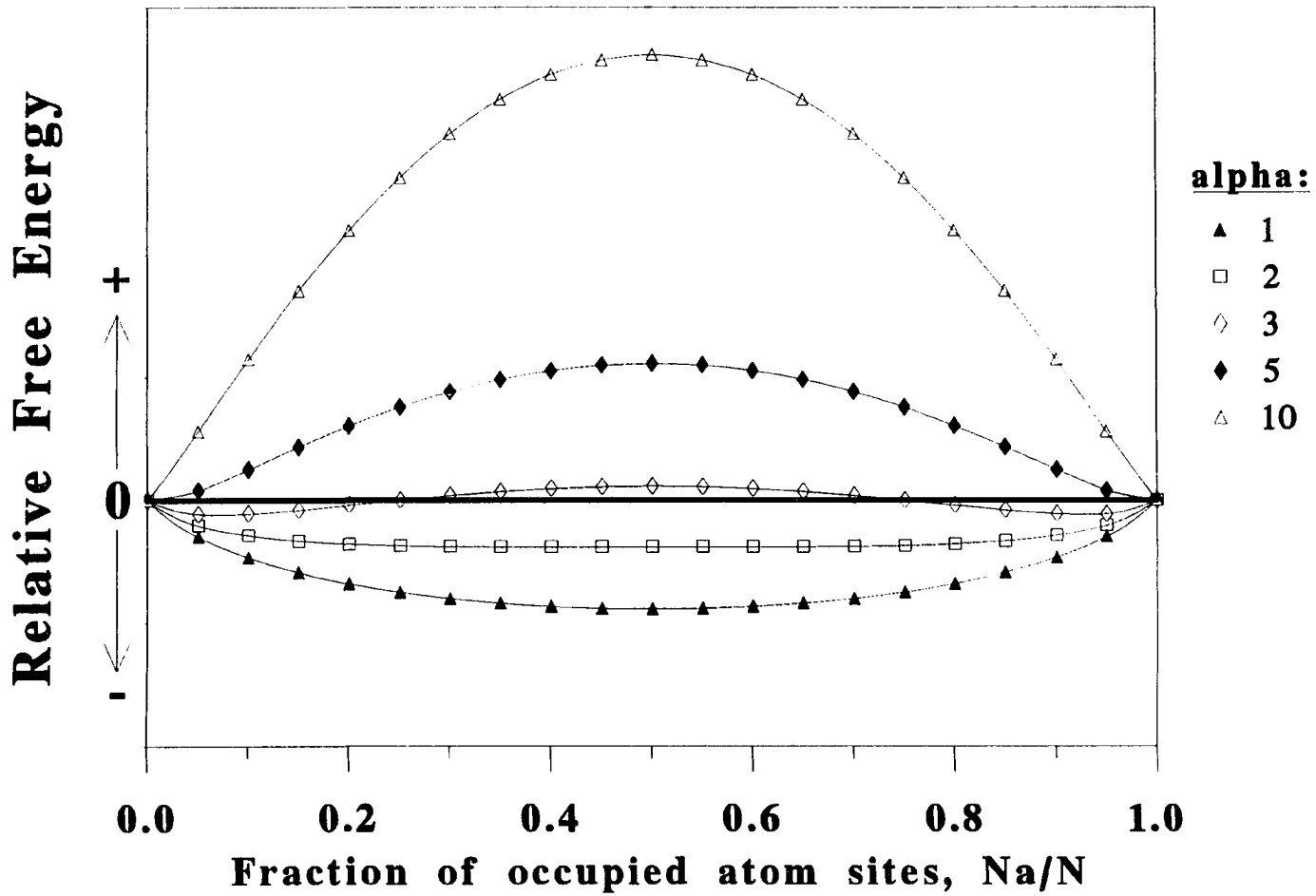

Figure 70. Free energy as a function of the fraction of planar occupied atom sites. (from Jackson, 1958)

SUMMARY & CONCLUSIONS

The nucleation and growth of eutectic and off-eutectic Al-Zn alloys was examined with the use of differential scanning calorimetry and directional solidification experimental techniques. Through the quantitative metallographic examination of solidified microstructures and the analytical treatment of the experimental data, the following conclusions can be made:

1) Non-reciprocal nucleation characteristics were found for the Al-Zn system. For alloys with zinc concentrations less than 95wt% where aluminum is the proeutectic phase, an average undercooling of 0.25°C below the eutectic temperature is required for zinc nucleation and subsequent eutectic formation at a cooling rate of 1 K/min. In comparison, an average undercooling of 4.0°C is necessary for aluminum nucleation on proeutectic zinc in alloys containing $\geq$95wt% zinc at the same cooling rate. Aluminum is therefore said to be a better nucleant of zinc than vice-versa. This is in contrast to previous discussions on non-reciprocal nucleation characteristics, which predict elements with higher solid/liquid interfacial energies to be better nucleants than vice versa. Thus other factors, such as crystal structure, may play a role in non-reciprocal nucleation.

2) The non-reciprocal nucleation characteristics of the Al-Zn system result in the formation of zinc halos around proeutectic aluminum in Al-rich off-eutectic alloys.

Once zinc is nucleated by proeutectic aluminum, it requires a significant undercooling before nucleating aluminum for eutectic growth. The result is a zinc halo around proeutectic aluminum, the size of which is limited by the growth rate of zinc and the time necessary to reach the temperature at which zinc will nucleate aluminum. In contrast to published literature on halo formation, the present study indicates that the coupled zone for the Al-Zn system indirectly affects halo size but does not influence the mechanism for halo formation.

3) The non-reciprocal nucleation characteristics of the Al-Zn system result in a significant difference in the eutectic interlamellar spacing (λ) when comparing hypo- and hypereutectic alloys having a cast structure. Since a negligible undercooling is required for hypoeutectic alloys, where proeutectic aluminum must nucleate zinc for eutectic growth to occur, λ is greater for these alloys than for hypereutectic alloys. At low cooling rates, this difference can be as much as 7-fold. The measured λ values for all alloy compositions used were in agreement with theoretical predictions of λ based on measured undercoolings.

4) The non-reciprocal nucleation characteristics for the Al-Zn system result in a difference in the volume fraction of second phase in the eutectic and in the eutectic morphology when comparing hypo- and hypereutectic alloys having a cast structure. Because of the significant undercooling required for eutectic nucleation of Zn-rich off-eutectic alloys, the volume fraction of each phase in the eutectic structure cannot be

predicted from the equilibrium phase diagram. For example, the volume fraction of second phase (β-Al) in these alloys was measured to be an average of 0.40, which is considerably greater than the equilibrium value of 0.28. In contrast the volume fraction of β-Al in Al-rich off-eutectic alloys was measured to be an average of 0.26, which can be expected due to the minimal undercooling for eutectic nucleation associated with these alloys. In agreement with surface energy considerations, the eutectic structure for Al-rich alloys was therefore found to consist of rods, or rods and lamellae, whereas the eutectic structure of Zn-rich alloys was found to consist only of lamellae.

5) In agreement with theory, the interlamellar spacing for unidirectionally solidified Al-Zn alloys was found to be proportional to $V^{-1/2}$. Unlike alloys having a cast structure, the measured λ values for directionally solidified alloys were found to be independent of alloy composition. This difference arises since, for cast alloys, the undercooling associated with eutectic growth is controlled by composition and the ability of proeutectic phases to nucleate the eutectic, whereas for directionally solidified alloys, the undercooling associated with eutectic growth is only a function of growth rate.

6) In contrast to alloys having a cast structure, directionally solidified Al-Zn alloys were found to grow with a lamellar eutectic structure. Rod eutectic structures were found in these samples only when (1) the eutectic nucleated on a primary dendrite

ahead of the solid/liquid interface during growth, and/or (2) the eutectic solidification front encountered a preexisting primary dendrite, causing a breakdown in the planar solid/liquid interface. The former mechanism was found to occur only at growth rates $\geq 50\mu$m/second due to a relatively high interfacial undercooling, which leads to an increased temperature and time lag between the interface and a volume element within the melt zone. This can allow a significant portion of the liquid within the melt zone to drop below the equilibrium eutectic temperature, and eutectic nucleation can therefore occur on heterogeneous nucleation sites. The volume fraction of second phase in the rod regions was found to depend on the mechanism by which the rods formed. By the former process, the volume fraction of β-Al in the eutectic was determined to be an average of 0.28 whereas for the latter mechanism, this value was 0.46.

7) The coupled zone for the Al-Zn system was found to be skewed to the Al-rich side of the eutectic. It was found that the constitutional supercooling criterion did not accurately predict the eutectic-dendritic transition for this system. Instead, it is hypothesized that the competitive growth criterion controls the formation of the stable microstructure. Therefore, it is suggested that the eutectic structure outgrows β-Al dendrite formation at undercoolings $> 3°C$ below the eutectic temperature when in the presence of low temperature gradients in the melt (2.9-12.2 K/mm).

8) Banding was found for directionally solidified alloys having a composition of 94wt% - 96wt% zinc when grown at rates $\leq 50\mu$m/second. A close examination of the bands indicates these regions to be precipitation zones for either of the two eutectic phases. Banding is thought to occur when, during eutectic growth, one of the eutectic phases accumulates at the solid/liquid interface to a concentration which cannot be absorbed by the growing eutectic or sustained as a boundary layer by the advancing interface. This "solute adjustment" can manifest itself as a change in the eutectic interlamellar spacing, a change in the volume fraction of the eutectic phases, and/or the phase precipitation ahead of the solid/liquid interface.

9) The interfacial undercoolings during directional solidification, as estimated from measured values of λ, were found to be higher than those predicted from theory. This, along with the finding of a skewed coupled zone of growth, suggests that either the Al-Zn eutectic does not from under extrenum conditions or that there is some other contribution to the interface undercooling. The skewed coupled zone, in particular, suggests that there may be a significant kinetic undercooling associated with β-Al growth. However, thermodynamic data for β-Al obtained via differential scanning calorimetry yields an entropy of fusion of 10.9 J/mol•K, and therefore, an α-factor of 1.31. These data are in agreement to published values for aluminum, which, in accordance with Jackson's theory on faceting, predict anisotropic growth and a negligible kinetic undercooling.

Suggestions for Future Work

Although the research presented here provides much insight into the solidification processes in Zn-5%Al as an alloy and a coating, further work should be conducted to determine the exact effects of alloy nucleation and growth on coating structure and properties. There are many difficulties which arise when trying to emulate a commercial process in the laboratory, and it is important to recognize the difficulties and errors which may arise when extrapolating experimental results. For example, when characterizing the nucleation characteristics for the Al-Zn system, cooling rates of up to 80 K/min were used in the laboratory. This is in contrast to Galfan coatings, the cooling rate for which is considered to be on the order of several hundred degrees per minute. In addition, the samples used during cooling experiments were placed on glass slides to avoid interactions with a reactive substrate, when clearly this is not the case for galvanized coatings as a whole. To truly apply the results of this study to zinc coatings, an additional study should be conducted on a pilot galvanizing line to determine the effects of controlled parameters such as cooling rate, impurity content, etc.. on coating characteristics. One interesting aspect of such a work would be to consider the role of intentionally-added nucleating agents, such as zinc powder, on coating structure. Although many Galfan producers use this process in line (so-called Heurtey process), not much is known about its effects on coating structure and surface characteristics.

It was hoped that computer modelling of the hot-dipping process could be

incorporated into this work, but the complexity of this problem made it impossible. Through finite element analysis techniques, the heat flow characteristics of the steel sheet entering and leaving the zinc pot can be determined as a function of various processing conditions. The effects of variables such as sheet preheat temperature, bath temperature, wipe pressure, line speed, and bath residence time, on strip thermal history, and therefore coating microstructure, can be predicted by this method.

The role of Pb on Al-Zn solidification should be examined. There has recently been a great deal of discussion within the galvanizing community concerning the influence of lead on coating nucleation, growth, and final microstructure. Theories which have sometimes been conflicting have been proposed on these subjects, often without experimental verification. A thorough study on the effects of lead content on zinc solidification would help resolve some questions still outstanding on the role of lead during galvanizing.

Finally, a reassesment of the Al-Zn phase diagram may be a worthwhile endeavor. During the course of this study, an alloy containing 83wt% Zn was was found to contain interdendritic eutectic even though the solubility of Zn in Al solid solution is indicated to be 83.1wt% in the most widely accepted version of the phase diagram. Also, the Al-rich alloys used in this study were consistently found to have more proeutectic phase than the amount predicted by the current phase diagram. This is unexpected since these alloys did not undercool below the equilibrium eutectic temperature in order to nucleate the eutectic. Considering that the placement of the Al liquidus and solvus lines were last examined in 1949 and 1951, respectively, and

that some researchers still question the presence of a peritectic reaction in this system, a thorough evaluation of the phase diagram using modern techniques may be informative and applicable to the engineering of Zn-based hot-dip coatings.

REFERENCES

(Barclay et al., 1973):
R.S. Barclay, P. Niessen, and H.W. Kerr, *J. Cryst. Growth*, 20(1973)175.

(Botschwar, 1934):
A.A. Botschwar, *Z. Anorg. Chem.*, 220(1934)334.

(Burden and Hunt, 1974):
M.H. Burden and J.D. Hunt, *J. Cryst. Growth*, 22(1974)109.

(Chadwick, 1963a):
G.A. Chadwick, *Prog. Mat. Sci.*, 12(1963)97.

(Chadwick, 1963b):
G.A. Chadwick, *J. Inst. Met.*, 92(1963)18.

(Chen et al., 1990):
Z.W. Chen, J.T. Gregory, and R.M. Sharp, The 18th Australian Chemical Engineering Conference [Proc. conf.], Auckland, p. 296.

(Chu et al., 1984):
M.G. Chu, Y. Shiohara, and M.C. Flemings, *Met. Trans. A*, 15A(1984)1303.

(Clark and Elliott, 1976):
J.N. Clark and R. Elliott, *Met. Trans. A*, 7A(1976)1197.

(Cooksey et al.):
D.J.S Cooksey, D. Munson, M.P. Wilkinson, and A. Hellawell, *Phil. Mag.*, 10(1964)745.

(Davies, 1964):
V. de L. Davies, *J. Inst. Met.*, 93(1964-65)10.

(Ellwood, 1940):
E.C. Ellwood, *J. Inst. Met.*, 66(1940)87.

(Ewen and Turner, 1910):
D. Ewen and T. Turner, *J. Inst. Met.*, 4(1910)140.

(Fink and Willey, 1936):
W.L. Fink and L.A. Willey, *Trans. AIME*, 122(1936)244.

(Fuller and Wilcox, 1935):
M.L. Fuller and R.L. Wilcox, *Trans. AIME*, 117(1935)338.

(Gayler and Sutherland, 1938):
M.L.V. Gayler and E.G. Sutherland, *J. Inst. Met.*, 63(1938)123.

(Gigliotti et al., 1970):
M.F.X. Gigliotti, G.A. Colligan, and G.L.F. Powell, *Met. Trans.*, 1(1970)891.

(Goldak and Parr, 1963):
G.R. Goldak and J.G. Parr, *J. Inst Met.*, 92(1963-64)230.

(Hanson and Gayler, 1922):
D. Hanson and M.L.V. Gayler, *J. Inst. Met.*, 27(1922)267.

(Heycock and Neville, 1897):
C.T. Heycock and F.H. Neville, *J. Chem. Soc.*, 71(1897)383.

(Hirose, 1985):
Y. Hirose, "Influence of Aluminum Contents of Coating on the Properties of Galfan", Proceedings of the 7th Galfan Licenses Meeting, Belgium, 1985, p. 1.

(Holloman and Turnbull, 1951):
J.H. Hollomon and D. Turnbull, *Trans. AIME*, September (1951) 803.

(Hunt, 1966):
J.D. Hunt, *J. Inst. Met.*, 94(1966)125.

(Hunt and Chilton, 1963a):
J.D. Hunt and J.P. Chilton, *J. Inst. Met.*, 92(1963-64)21.

(Hunt and Chilton, 1963b):
J.D. Hunt and J.P. Chilton, *J. Inst. Met.*, 92(1963-64)338.

(Hunt and Jackson, 1966):
J.D. Hunt and K.A. Jackson, *Trans. AIME*, 236(1966)843.

(Hunt and Jackson, 1967):
J.D. Hunt and K.A. Jackson, *Trans. AIME*, 239(1967)864.

(Jackson, 1958):
K.A. Jackson, Liquid Metals and Solidification, ASM, Ohio, 1958, pp. 174-186.

(Jackson, 1968):
K.A. Jackson, *Trans. AIME*, 242(1968)1275.

(Jackson and Hunt, 1966):
K.A. Jackson and J.D. Hunt, *Trans. AIME*, 236(1966)1129.

(Jaffrey and Chadwick, 1969):
D. Jaffrey and G.A. Chadwick, *J. Inst. Met.*, 97(1969)118.

(Jordan and Hunt, 1971):
R.M. Jordan and J.D. Hunt, *J. Cryst. Growth*, 11(1971)141.

(Kofler, 1950):
A. Kofler, *Z. Metallk.*, 41(1950)221.

(Kraft and Albright, 1961):
R.W. Kraft and D.L. Albright, *Trans. AIME*, 221(1961)95.

(Kurz and Fisher, 1979):
W. Kurz and D.J. Fisher, *Int. Met. Rev.*, 5/6(1979)177.

(Kurz and Fisher, 1989):
W. Kurz and D.J. Fisher: Fundamentals of Solidification, 3rd ed., Trans Tech Publications, Switzerland, 1989.

(Lamberigts and Leroy, 1992):
M. Lamberigts and V. Leroy, "Galfan Reactivity With Steel Substrate, Mg Containing Galfan and Classical Galfan Ductility", Progress Report CRM no 25, 1992.

(Lamberigts et al., 1990):
M. Lamberigts, D. Coutsouradis, and V. Leroy, "Continuous Galfan Coating of Steel Sheet and Wire, ILZRO Project no 22, 1990.

(Lamberigts et al., 1991):
M. Lamberigts, V. Leroy, and F.E. Goodwin, The Third International Zinc Coated Sheet Conference, Barcelona, 1991, S1D/1.

(Lemaignan, 1981):
C. Lemaignan, *Acta metall.*, 29(1981)1379.

(Lemaignan et al., 1980):
C. Lemaignan, M.C. Cheynet, and N. Eustathopoulos, *J. Cryst. Growth*, 50(1980)720.

(Liu and Jones, 1992a):
H.Y. Liu and H. Jones, *Acta Metall. Mater.*, 40/8(1992)229.

(Liu and Jones, 1992b):
H.Y. Liu and H. Jones, *Acta Metall. Mater.*, 40/8(1992)2003.

(Livingston et al., 1970):
J.D. Livingston, H.E. Cline, E.F. Koch, and R.R. Russell, *Acta Metall.*, 18(1970)399.

(Mäkimattila, 1986):
S.J. Makimattila, *Scand. J. Met.*, 15(1986)224.

(Marder, 1990):
A.R. Marder, Proceedings of Zinc-Based Steel Coating Systems: Metallurgy and Performance, ed. by G. Krauss and D.K. Matlock, TMS, Pennsylvania, 1990.

(Marder, 1992):
A. Marder, "A Fundamental Investigation of the Occurrence of Grain Boundary Dents in Galfan", Proceedings of the 17th Galfan Licensees Meeting, Tokyo, 1992, p. I-1.

(Mathieu et al., 1991):
S. Matieu, F.E. Goodwin, and M. Lamberigts, The Third Interntaional Zinc Coated Sheet Conference, Barcelona, 1991, S4H/1.

(Mollard and Flemings, 1967a):
F.R. Mollard and M.C. Flemings, *Trans. AIME*, 239(1967)1526.

(Mollard and Flemings, 1967b):
F.R. Mollard and M.C. Flemings, *Trans. AIME*, 239(1967)1534.

(Moore and Elliott, 1967):
A. Moore and R. Elliott, *J. Inst. Met.*, 95(1967)369.

(Murray, 1983):
J.L. Murray, *Bull. Alloy Ph. Diags.*,4/1(1983)55.

(Nayak, 1973):
A.K. Nayak, *J. Inst. Met.*, 101(1973)309.

(Perepezko, 1984):
J.H. Perepezko, *Mat. Sci. Eng.*, 65(1984)125.

(Porot et al., 1987):
P.A. Porot, N. Ventham, R.D. Jones, and J.A. Spittle, *Metallography*, 20(1987)181.

(Powell and Colligan, 1971):
G.L.F. Powell and G.A. Colligan, *Met. Trans.*, 2(1971)849.

(Radtke and Herrschaft, 1983):
S.F. Radtke and D.C. Herrschaft, *J. Less Common Met.*, 93(1983)253.

(Roman, 1989):
M.P. Roman, Proceedings of the International Conference on Zinc and Zinc Alloy Coated Steel Sheet, 1989, The Iron and Steel Institute of Japan, p. 359.

(Roman and Lynch, 1989):
M.P. Roman and R.F. Lynch, *Met. Bull. Monthly*, 222/6(1989)50.

(Rosenhain and Archbutt, 1911):
W. Rosenhain and S.L. Archbutt, *J. Inst. Met.*, 6(1911)236.

(Salli et al., 1975):
I.V. Salli, V.Z. Dolinskaya, and D.G. Borshchevskaya, *Fiz. metal. metalloved.*, 40(1975)1020.

(Seetharaman and Trivedi, 1988):
V. Seetharaman and R. Trivedi, *Met. Trans. A*, 19A(1988)2955.

(Shepherd, 1905):
E.S. Shephard, *J. Phys. Chem.*, 9(1905)504.

(Smithells, 1983):
C.J. Smithells, Metals Reference Book, 6th ed., 1983.

(Southin and Chadwick, 1978):
R.T. Southin and G.A. Chadwick, *Acta Metallurgica*, 26(1978)223.

(Spittle, 1977):
J.A. Spittle, *Met. Sci.*, 12(1977)578.

(Suk et al., 1992):
M-J. Suk, G-H. Choi, and I-H. Moon, *J. Cryst. Growth*, 123(1992)5.

(Sundquist and Mondolfo, 1961):
B.E. Sundquist and L.F. Mondolfo, *Trans. AIME*, 221(1961)157.

(Sundquist et al., 1963):
B.E. Sundquist, R. Bruscato, and L.F. Mondolfo, *J. Inst. Met.*, 91(1962-63)204.

(Sutliff, 1988):
J.A. Sutliff: "A TEM Investigation of a Hyper-eutectic Lead-Tin Alloy", Proceedings of the 46th Annual Meeting of the Electron Microscopy Society of America, G.W. Bailey, Ed., San Francisco Press, 1988, p. 562-563.

(Tammann and Botschwar, 1934):
G. Tammann and A.A. Botschwar, *Z. Anorg. Chem.*, 220(1934)334.

(Tiller, 1958):
W.A. Tiller, in Liquid Metals and Solidification, ASM, Ohio, p. 276.

(Thompson and Spaepen, 1983):
C.V. Thompson and F. Spaepen, *Acta metall.*, 31/12(1983)2021.

(Tuček et al., 1986):
V. Tuček, S. Holeček, L. Kubíček, and C. Barta, *Cryst. Res. Technol.*, 21/10(1986)1355.

(Turnbull, 1950a):
D. Turnbull, *J. Chem. Phys.*, 21(1950)1022.

(Turnbull, 1950b):
D. Turnbull, *J. Chem. Phys.*, 18/2(1950)198.

(Turnbull and Cech, 1950):
D. Turnbull and R.E. Cech, *J. Appl. Phys.*, 21(1950)804.

(Turnbill and Fisher, 1949):
D Turnbull and J.C. Fisher, *J. Chem. Phys.*, 17/1(1949)71.

(Úředníček and Kirkaldy, 1973):
M. Úředníček and J.S. Kirkaldy, *Z. Metallkde.*, 4(1973)899.

(Weinberg et al., 1990):
F. Weinberg, M. Mager, and L. Frederick, *Can. Met. Quart.*, 29/2(1990)163.

(Yamaguchi and Hisamatsu, 1979):
H. Yamaguchi and Y. Hisamatsu, *Trans. ISIJ*, 19(1979)649.

(Yilmaz and Elliott, 1984):
F. Yilmaz and R. Elliott, *Met. Sci.*, 18(1984)362.

(Zener, 1946):
C. Zener, *Trans. AIME*, 167(1946)550.

VITA

Scott Thomas Bluni was born to Thomas D. and Carol A. Bluni on December 16, 1966, in Rockville Centre, New York. He graduated from St. Anthony's High School in June, 1985, with hopes of applying his interests in mathematics and science to an engineering education. Scott attended Lafayette College from 1985 to 1989, graduating from that institution with honors in Metallurgical Engineering. Following undergraduate school, Scott attended Lehigh University where he served as a research assistant for Professor A.R. Marder and also as a teaching assistant for four laboratory classes during five separate semesters in the Department of Materials Science & Engineering. After receiving a Master of Science degree in 1992, Scott continued to work towards a Ph.D. at Lehigh. During his studies at Lehigh, Scott has prepared six manuscripts for publication and served as speaker at seven regional and international conferences. Scott is married to his high school sweetheart Maria and has two sons, Scott and Mark.